JNC TN9400 2001-008

Frequency response function method with constraint efficiency factors for Hot/Cold spot problems

(Research Report)

January 2000

Japan Nuclear Cycle Development Institute
O-arai Engineering Center

KO

JNC TN9400 20001-008
January 2 0 0 0

Frequency response function method with constraint efficiency factors for Hot/Cold spot problems

(Research Report)

Naoto Kasahara*

Abstract

Temperature fluctuation from incomplete fluid mixing induces typically bending plus peak stress across wall thickness. For this stress mode, author has developed the frequency response function to establish design-by-analysis methodology for this phenomenon. On the other hand, it is pointed out that hot and cold spots appear near T-junctions in piping systems. Those induce other stress modes from three-dimensional temperature distributions. This report describes the extension of the frequency response method to hot and cold spot problems by introducing constraint efficiency factors. Its applicability was validated by application to a hot spot near the T-junction of PHENIX secondary piping system.

* Structure and Material Research Group, System Engineering Division, OEC, JNC

JNC TN9400 2001-008
２０００年１月

ホット/コールドスポット評価のための有効拘束係数を用いた周波数応答関数法

（研究報告書）

笠原 直人*)

要　旨

流体温度ゆらぎが構造物に引き起こす応力は、通常板厚内の曲げ応力とピーク応力である。この応力モードに対する解析的評価法として著者は周波数応答関数を提案した。これに対し、高温と低温の配管の合流部近傍に生じるホット/コールドスポットは、配管内に3次元的な温度分布と応力分布を生じさせる可能性がある。

本研究では、3次元問題を評価可能とするため、有効拘束係数を導入することによって周波数応答関数の拡張を行った。

また、拡張した周波数応答関数をフェニックスの二次系配管合流部近傍に生じたホットスポット問題に適用し、評価精度を検証した。

尚、本内容は1999年9月から2000年8月までの期間にCEAカダラッシュ研究所にて実施した業務の一部である。

*) 大洗工学センター システム技術開発部 構造材料技術開発グループ

Contents

NOMENCLATURE

ΔT_f : Amplitude of sinusoidal temperature fluctuation of fluid

$\Delta\sigma|_{x=0}$: Amplitude of sinusoidal stress fluctuation on the structural surface

$\Delta\sigma^*$: Stress range under perfect heat transfer and full constraint conditions

σ_c : Stress at the center of hot spot

σ_i : Stress at the boundary inside the hot spot

σ_o : Stress at the boundary outside the hot spot

$T_f(j\omega)$: Expression of $T_f(t)$ in frequency domain

$\sigma(j\omega)$: Expression of stress in frequency domain

$G(B_i, jf^*)$: Frequency response function of structural surface to fluid temperature fluctuation

$G(B_i, jf^*, A_m, A_b)$: Frequency response function with constraint efficiency factors

$H(B_i, jf^*)$: Frequency response function of effective heat transfer

$S(jf^*)$: Frequency response function of effective thermal stress on the surface

$S(jf^*, A_m, A_b)$: Frequency response function of effective thermal stress with constraint efficiency factors

$Bi = \dfrac{hL}{\lambda}$: Biot number

A_m : Constraint efficiency factor of membrane stress

A_b : Constraint efficiency factor of bending stress

$f^* = \dfrac{fL^2}{a}$: Non-dimensional frequency

f: Frequency of sinusoidal fluctuation

ω: Rotational frequency of sinusoidal fluctuation

h: Heat transfer coefficient

L: Wall thickness of structure

a: Thermal diffusivity of structural material

λ : Heat conductivity of structural material

E : $Young's$ modulus of structural material

α : Linear expansion coefficient of structural material

ν : $Poisson's$ ratio of structural material

K: Stress index determined by mechanical boundary conditions and material properties

$K = 1/(1-\nu)$ in the case of biaxial plane stress condition

1 INTRODUCTION

At an incomplete mixing area of high and low temperature fluids near the structural surface, temperature fluctuations of fluid give thermal fatigue damages on the wall structures. This coupled thermohydraulic and thermomechanical phenomenon is called thermal striping. Typical thermal stress induced by thermal striping is bending plus peak stresses by temperature gradient in structural walls. Paying attention to such frequency characteristics that low frequency components of fluctuation may not cause large thermal stresses since thermal homogenization in materials, author have developed the Frequency response function method with Yves LEJEAIL of CEA [1]-[4].

On the other hand, it is pointed out the existence of another stress mode induced by hot and cold spots that appear near T-junctions in piping systems (Fig.1.1). For example, a hot spot is supposed to appear at the T-junction of PHENIX secondary piping system [5] and the CIBAUX PWR plant. Hot and cold spots are able to induce membrane stresses from three-dimensional temperature distributions. Since this stress hardly attenuated even though their frequencies are low, we should take care of this mode. This report describes the extension of the frequency response method to hot and cold spot problems by considering complex constraint conditions of membrane plus bending stresses.

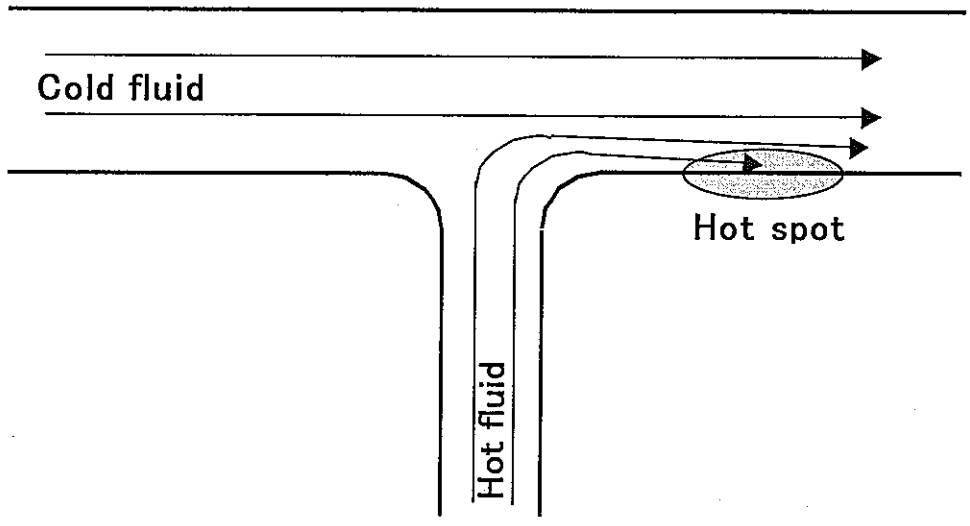

Fig.1.1 Hot spot near T-junctions in piping systems

2. PROPOSAL OF HOT/COLD SPOT EVALUATION METHOD

2.1. FORMULATION OF HOT/COLD SPOT PROBLEMS

Hot/Cold spot problems can be categorized as follows. Actual problems are considered as these combinations.

(1) Temperature changing spot

Location and seize of a spot are constant and its temperature changes as Fig.2.1.

(2) Moving spot

Temperature and seize of a spot are constant and its location moves as Fig.2.2.

(3) Size changing spot

Temperature and location of a spot are constant and its size changes as Fig.2.3.

In all of above cases, temperature at the same location changes. If structures are full constrained, induced stresses are proportional to temperature. Actual structures generate lower stresses because of finite constraint conditions from their own stiffness. A hot spot also causes inverse stresses before and after it.

In the case of the temperature changing spot, membrane plus bending components of temperature are transferred to thermal stress according to constraint conditions.

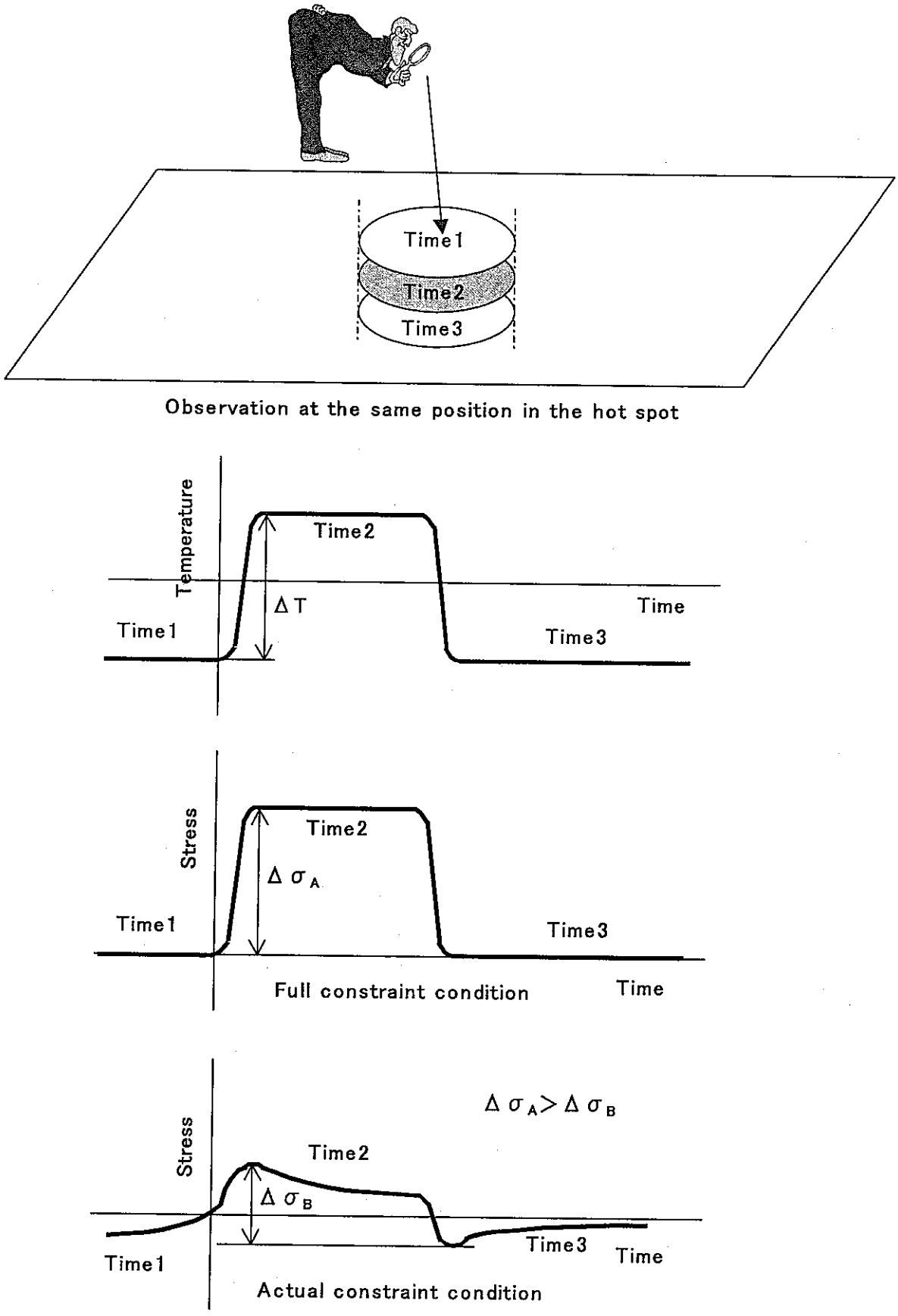

Fig. 2.1 Induced stress by a temperature changing hot spot

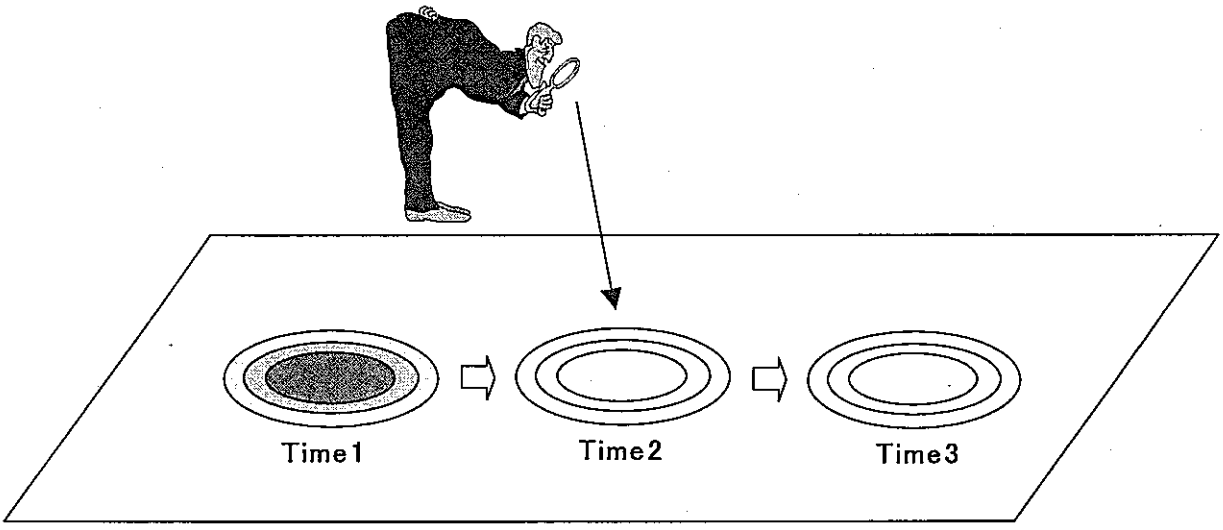

Observation at the same position

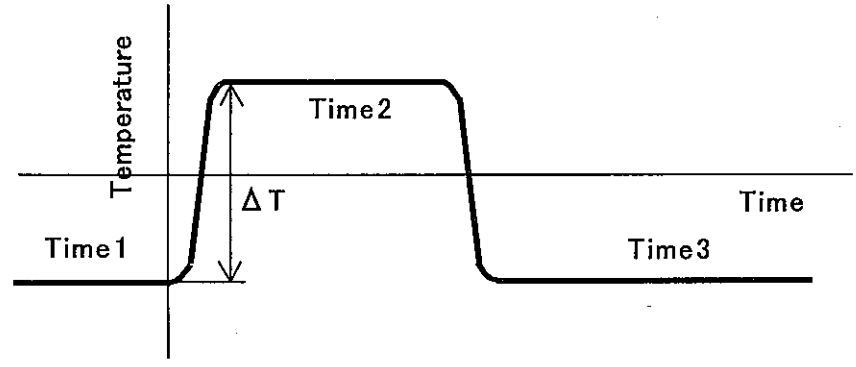

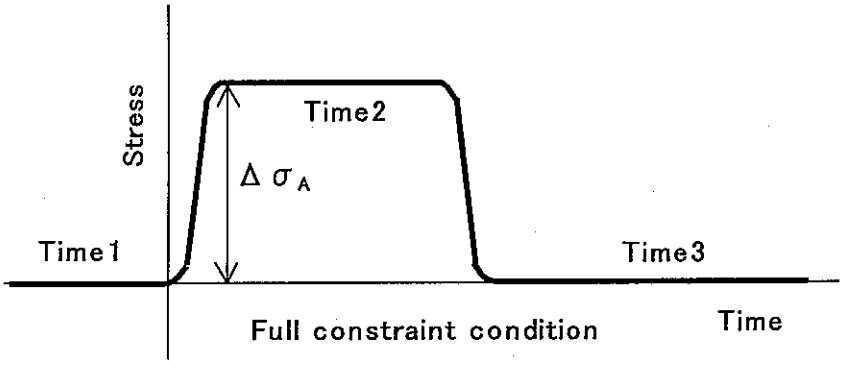

Full constraint condition

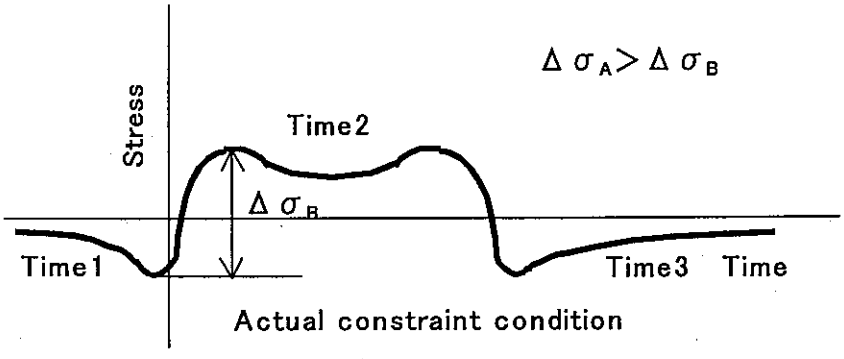

Actual constraint condition

Fig. 2.2 Induced stress by a moving hot spot

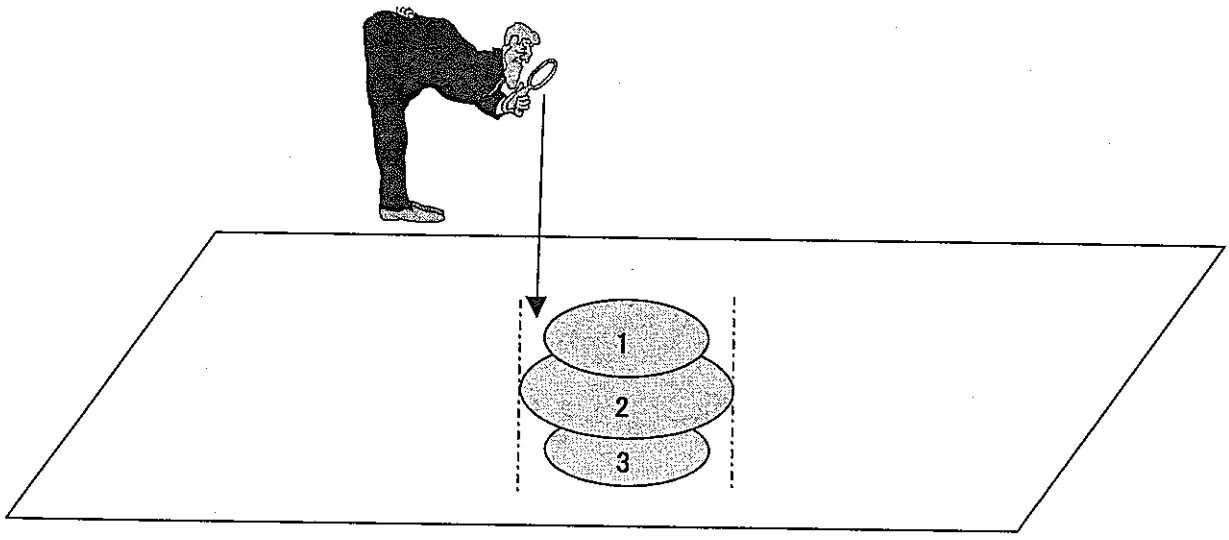

Observation at the edge of the hot spot

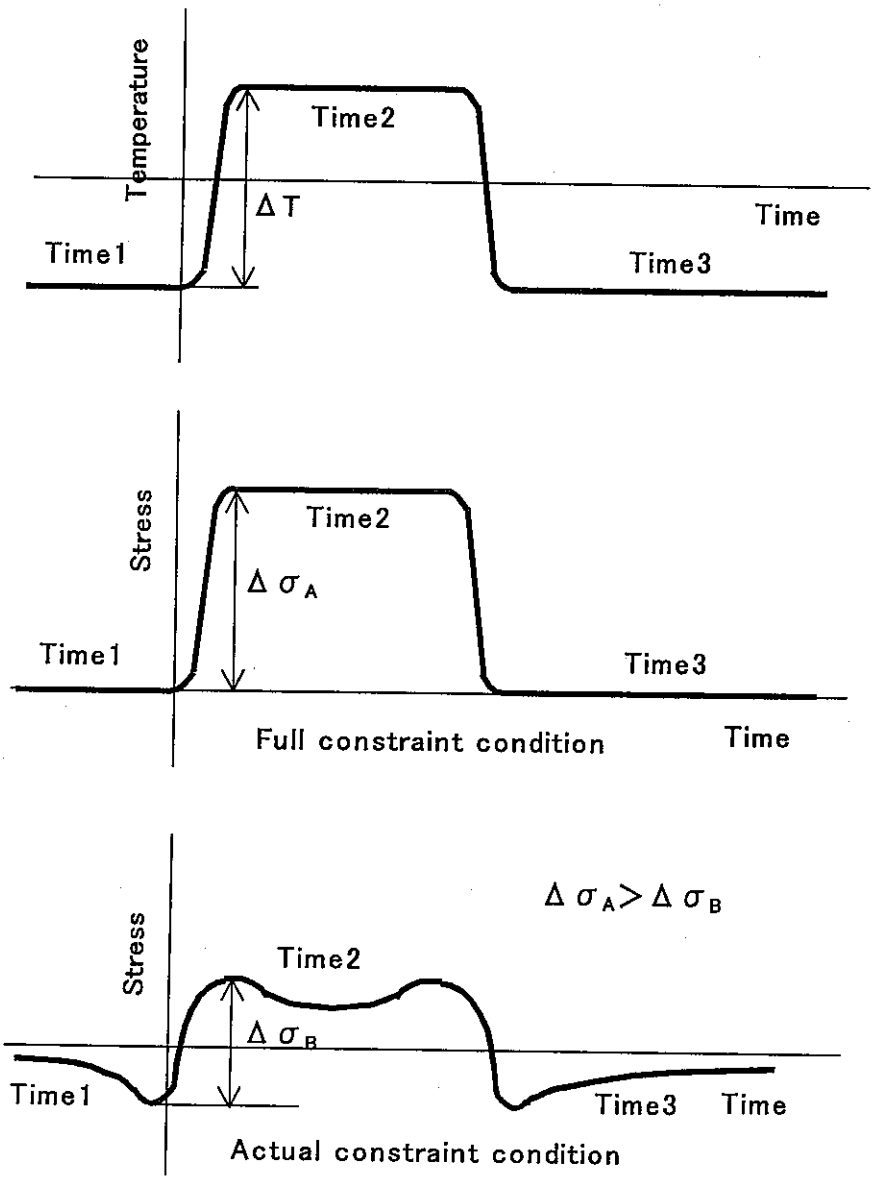

Fig. 2.3 Induced stress by a size changing hot spot

Temperature distributions across wall thickness can be categorized into membrane, bending and peak components. Among them, thermal expansions from peak components are full constrained by wall sections. Deformations by membrane and bending components are constrained by structural stiffness determined from their geometrical configurations. Here, ratios among membrane, bending and peak components of temperature are variable according to frequencies of temperature fluctuations. It means that different frequencies induce the different thermal stresses in the same structures.

From above consideration, Hot/Cold spot problems are formulated paying attention to constraint conditions of structures with relation to frequencies.

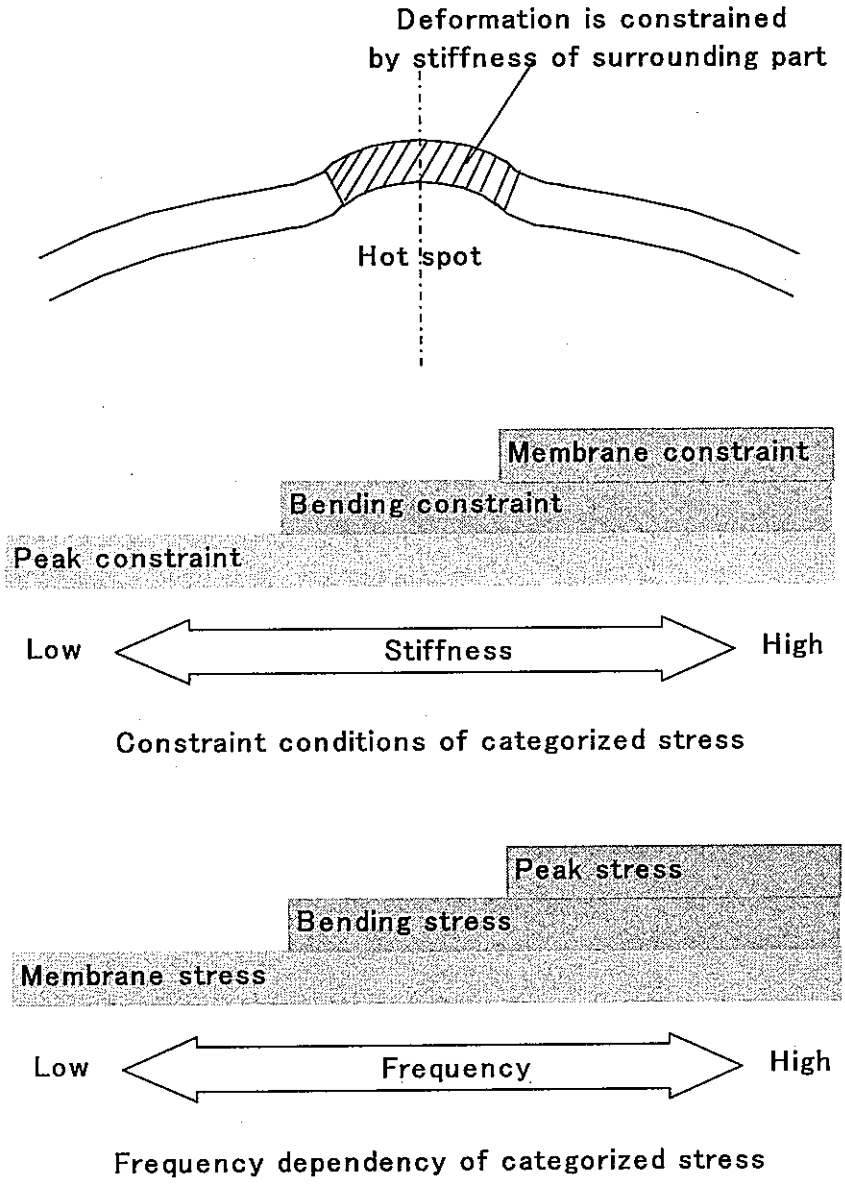

Fig.2.4 Frequency dependent thermal stresses and constraint conditions

2.2 FREQUENCY RESPONSE FUNCTION WITH CONSTANT EFFICIENCY FACTORS

General structures with hot/cold spots have mixed constraint conditions of membrane, bending and peak stresses. Mixing ratios among these stress components depend on structures and frequencies. In this chapter, the frequency response functions for arbitrary constraint conditions. The previous study provides Frequency response functions for (a) constraint free, (b) bending constraint and (c) membrane plus bending constraint conditions (Fig.2.5). These functions are provided by both formula of $G(B_i, jf^*)$ and diagrams as follows.

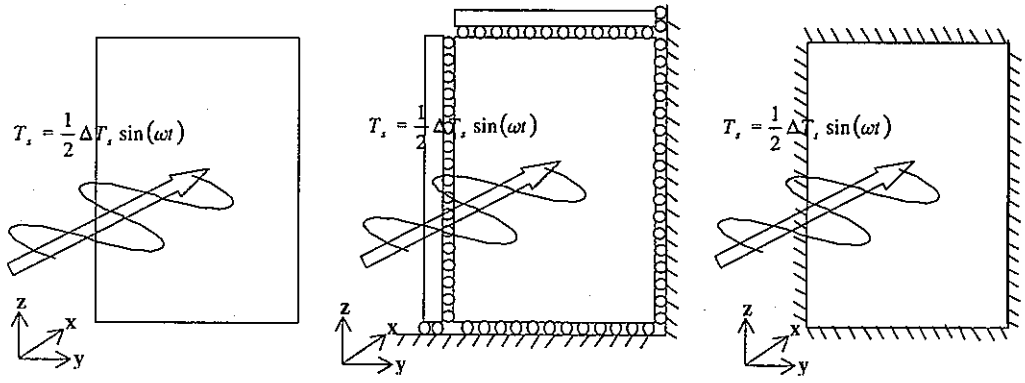

(a) Constraint free (b) Bending constraint (c) Membrane plus bending constraint

Fig.2.5 Variations of constraint conditions

$$G(B_i, jf^*) = H(B_i, jf^*)S(jf^*), \tag{2.1}$$

where $Bi = \dfrac{hL}{\lambda}$ and $f^* = \dfrac{fL^2}{a}$.

$$|H(Bi, j\omega)| = \frac{\dfrac{h}{\lambda}}{\sqrt{\left(\dfrac{h}{\lambda}+\sqrt{\dfrac{\omega}{2a}}\right)^2+\left(\sqrt{\dfrac{\omega}{2a}}\right)^2}} = \frac{L\dfrac{h}{\lambda}}{\sqrt{\left(L\dfrac{h}{\lambda}+\sqrt{L^2\dfrac{\omega}{2a}}\right)^2+\left(\sqrt{L^2\dfrac{\omega}{2a}}\right)^2}} = \frac{B_i}{\sqrt{\left(B_i+\sqrt{\pi f^*}\right)^2+\pi f^*}} \tag{2.2}$$

$$\angle H(Bi, j\omega) = -\tan^{-1}\frac{\sqrt{\dfrac{\omega}{2a}}}{\dfrac{h}{\lambda}+\sqrt{\dfrac{\omega}{2a}}} = -\tan^{-1}\frac{\sqrt{L^2\dfrac{\omega}{2a}}}{L\dfrac{h}{\lambda}+\sqrt{L^2\dfrac{\omega}{2a}}} = -\tan^{-1}\frac{\sqrt{\pi f^*}}{B_i+\sqrt{\pi f^*}} \tag{2.3}$$

(a) Constraint free

$$S(jf^*) = -(B + jC) + (B_m + jC_m) + (B_b + jC_b) \tag{2.4}$$

(b) Bending constraint

$$S(jf^*) = -(B + jC) + (B_m + jC_m) \tag{2.5}$$

(c) Membrane plus bending constraint

$$S(jf^*) = -(B + jC) \tag{2.6}$$

Where,

$$B = \frac{PR + QS}{R^2 + S^2}, \quad C = \frac{QR - PS}{R^2 + S^2}$$

$$P = R = \cos\sqrt{\pi f^*}\cosh\sqrt{\pi f^*}, \quad Q = S = \sin\sqrt{\pi f^*}\sinh\sqrt{\pi f^*}$$

$$B_m = \frac{1}{2\sqrt{\pi f^*}}\left[\frac{\sin\sqrt{\pi f^*}\cos\sqrt{\pi f^*} + \sinh\sqrt{\pi f^*}\cosh\sqrt{\pi f^*}}{\cos^2\sqrt{\pi f^*}\cosh^2\sqrt{\pi f^*} + \sin^2\sqrt{\pi f^*}\sinh^2\sqrt{\pi f^*}}\right]$$

$$C_m = \frac{1}{2\sqrt{\pi f^*}}\left[\frac{\sin\sqrt{\pi f^*}\cos\sqrt{\pi f^*} - \sinh\sqrt{\pi f^*}\cosh\sqrt{\pi f^*}}{\cos^2\sqrt{\pi f^*}\cosh^2\sqrt{\pi f^*} + \sin^2\sqrt{\pi f^*}\sinh^2\sqrt{\pi f^*}}\right]$$

$$B_b = \frac{3}{2\sqrt{\pi f^*}}\left[\frac{\sinh\sqrt{\pi f^*}\cosh\sqrt{\pi f^*} + \sin\sqrt{\pi f^*}\cos\sqrt{\pi f^*} - \dfrac{2\sinh\sqrt{\pi f^*}\sin\sqrt{\pi f^*}}{\sqrt{\pi f^*}}}{\cos^2\sqrt{\pi f^*}\cosh^2\sqrt{\pi f^*} + \sin^2\sqrt{\pi f^*}\sinh^2\sqrt{\pi f^*}}\right]$$

$$C_b = \frac{3}{2\sqrt{\pi f^*}}\left[\frac{\begin{array}{l}-\sinh\sqrt{\pi f^*}\cosh\sqrt{\pi f^*} + \sin\sqrt{\pi f^*}\cos\sqrt{\pi f^*} \\ + \dfrac{2}{\sqrt{\pi f^*}}\left(\cos^2\sqrt{\pi f^*}\cosh^2\sqrt{\pi f^*} + \sin^2\sqrt{\pi f^*}\sinh^2\sqrt{\pi f^*} - \cosh\sqrt{\pi f^*}\cos\sqrt{\pi f^*}\right)\end{array}}{\cos^2\sqrt{\pi f^*}\cosh^2\sqrt{\pi f^*} + \sin^2\sqrt{\pi f^*}\sinh^2\sqrt{\pi f^*}}\right]$$

$$\left|S(jf^*)\right| = \sqrt{\mathrm{Re}^2 + \mathrm{Im}^2} \tag{2.7}$$

$$\angle S(jf^*) = -\tan^{-1}\frac{\mathrm{Im}}{\mathrm{Re}} \tag{2.8}$$

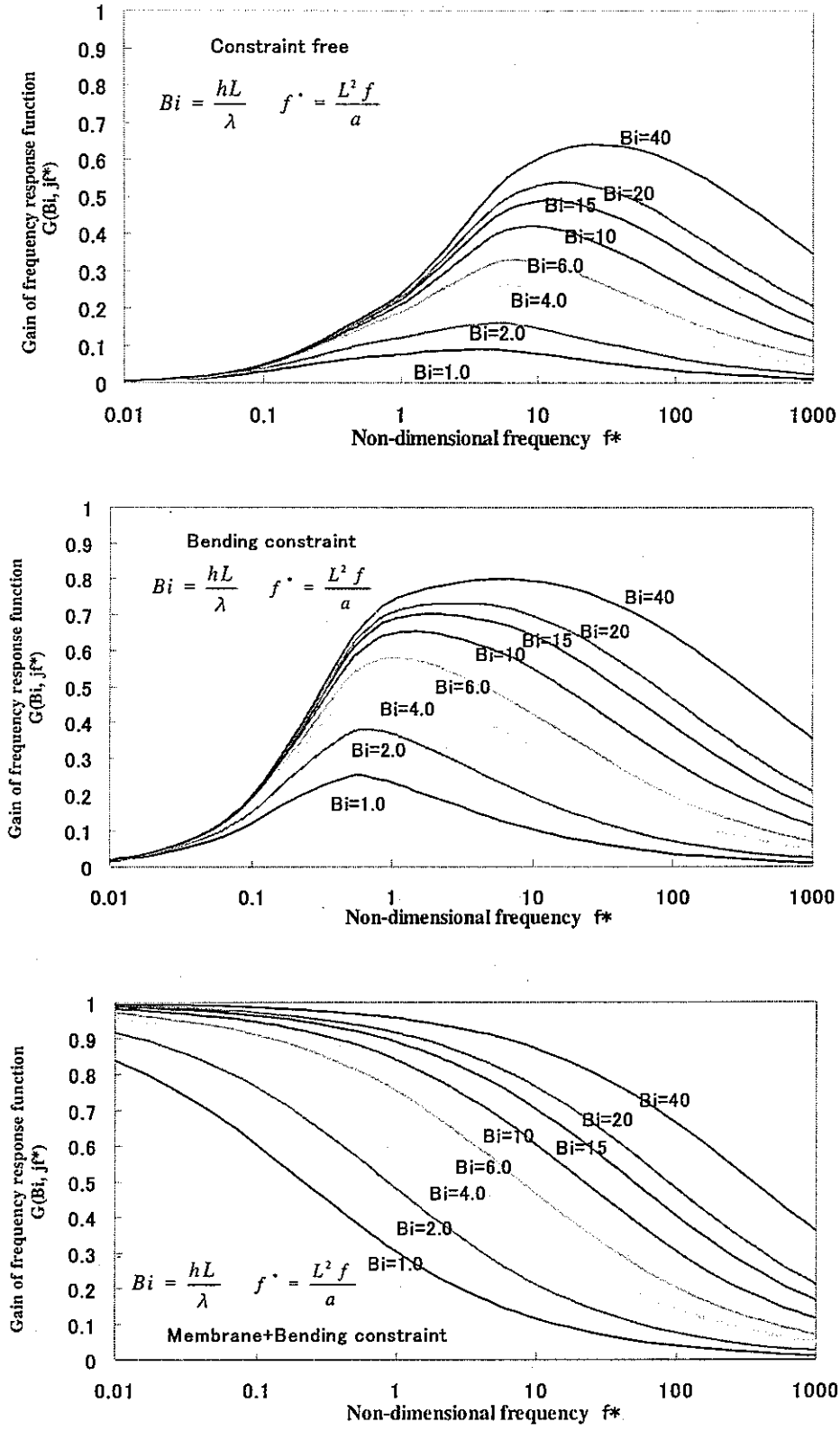

Fig.2.6 Frequency response function of categorized stress

Under elastic theory, arbitrary constraint conditions can be expressed by a linear summation of (a) constraint free, (b) bending constraint and (c) membrane plus bending constraint conditions. Therefore, If we can express, frequency characteristics of mixed problems can be described by a linear summation of Eqs.(2.4)～(2.6) with introduction of constraint efficiency factors A_m for membrane stress and A_b for bending stress.

$$S(jf^*, A_m, A_b) = -(B + jC) + (1 - A_m)(B_m + jC_m) + (1 - A_b)(B_b + jC_b) \tag{2.9}$$

Definition of the constraint efficiency factors A_m is a ratio of total stress (membrane plus bending plus peak stress) caused by membrane temperature component to stress by the same temperature under full constraint condition. Definition of the constraint efficiency factors A_b is the same for bending temperature component. Here, a constraint efficiency factor A_p for peak stress is one because of its full constraint condition. More preciously, these factors can be defined separately for membrane, bending and peak stresses. Eq.(2.9) gives frequency response diagrams for mixed constraint conditions as in the next figure.

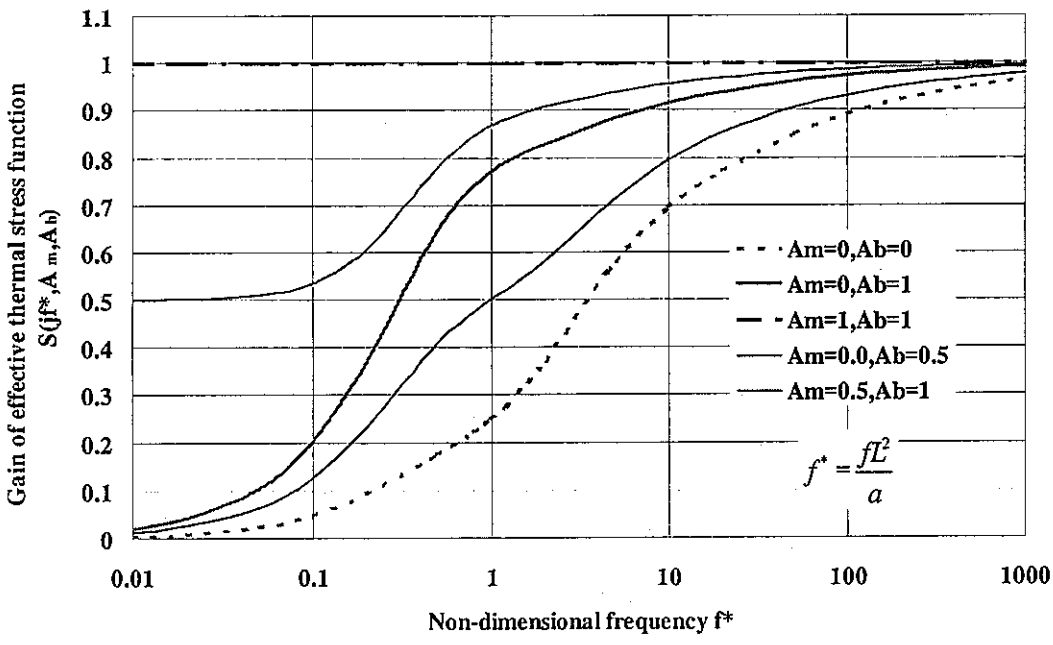

Fig. 2.7 Gain of effective thermal stress function with Am and Ab factors

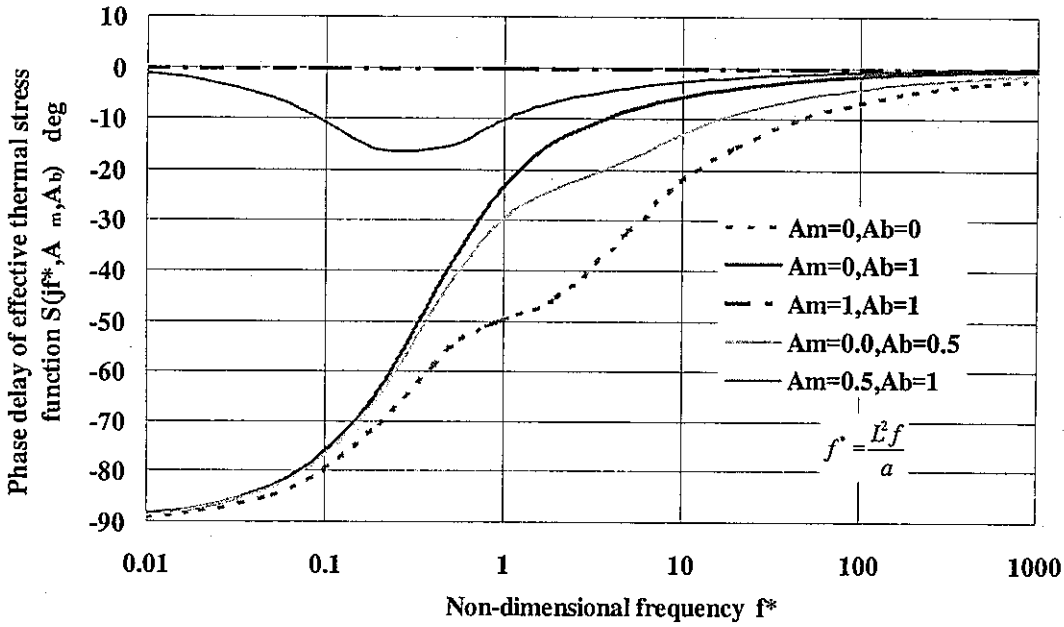

Fig. 2.8 Phase delay of effective thermal stress function with Am and Ab factors

By using Eg.(2.9), Eq.(2.1) can be extended to the frequency response function with constraint efficiency factors as

$$G(B_i, jf^*, A_m, A_b) = H(B_i, jf^*)S(jf^*, A_m, A_b). \tag{2.10}$$

In the case that Biot number is 6.02, frequency response diagrams can be obtained from Eq.(2.10) as in the next figures.

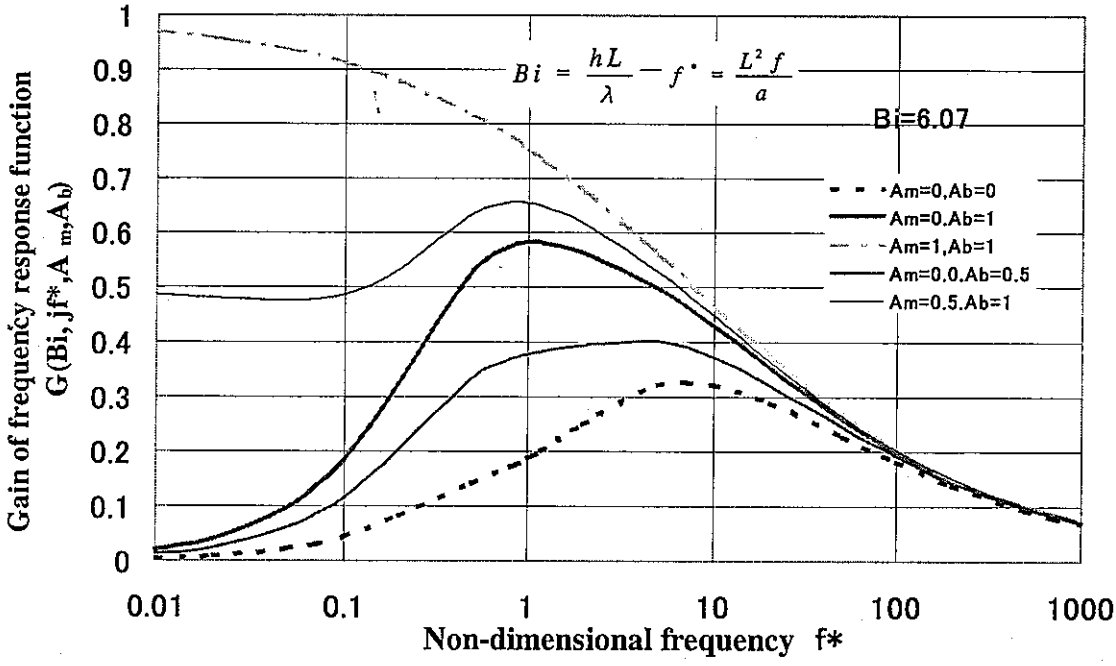

Fig. 2.9 Gain of frequency response function with Am and Ab parameters

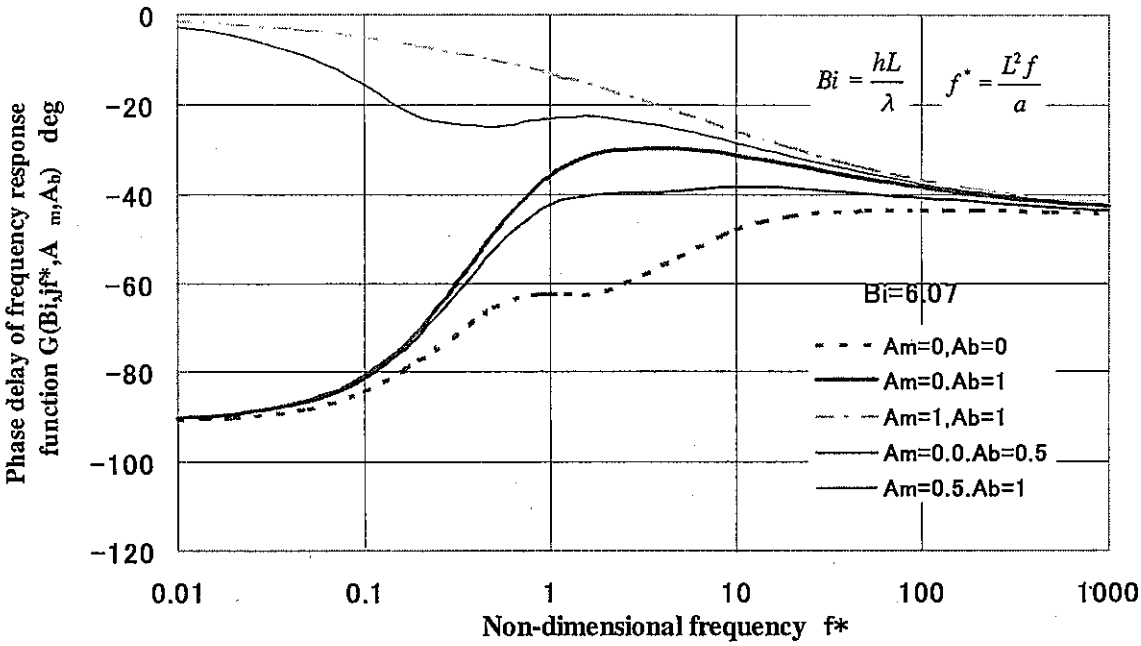

Fig. 2.10 Phase delay of frequency response function with Am and Ab parameters

By using above frequency response function with constraint efficiency factors, we can get stress ranges on the surface.

$$\Delta\sigma\big|_{x=0} = \Delta\sigma^* \left| G\left(B_i, jf^*, A_m, A_b\right) \right| . \tag{2.11}$$

where ideal stress range under perfect heat transfer and full constraint conditions is

$$\Delta\sigma^* = KE\alpha\Delta T_f . \tag{2.12}$$

3. APPLICATION TO ACTUAL PLANTS

3.1. HOT SPOT PROBLEM IN PHENIX SECONDARY PIPING SYSTEM

A small pipe is attached to a main pipe of the PHENIX secondary circuit containing cold sodium at 340℃, and discharges hot sodium at 430℃ into the main pipe. The two convergent flows with different temperatures (ΔT=90℃) are therefore mixed at the tee junction area. At the circumferential welded joint that locates at 160mm down stream from the tee junction, through wall cracks have been observed during the course of a campaign of inspection after operation of 90,000 hours [5]. One of main causes is supposed as fluctuation of a hot spot caused from injection of hot sodium (Fig.3.1). To study this problem, a 494mm radius and 7mm-thickness sphere shell with 200mm radius hot spot was assumed (Fig.3.2).

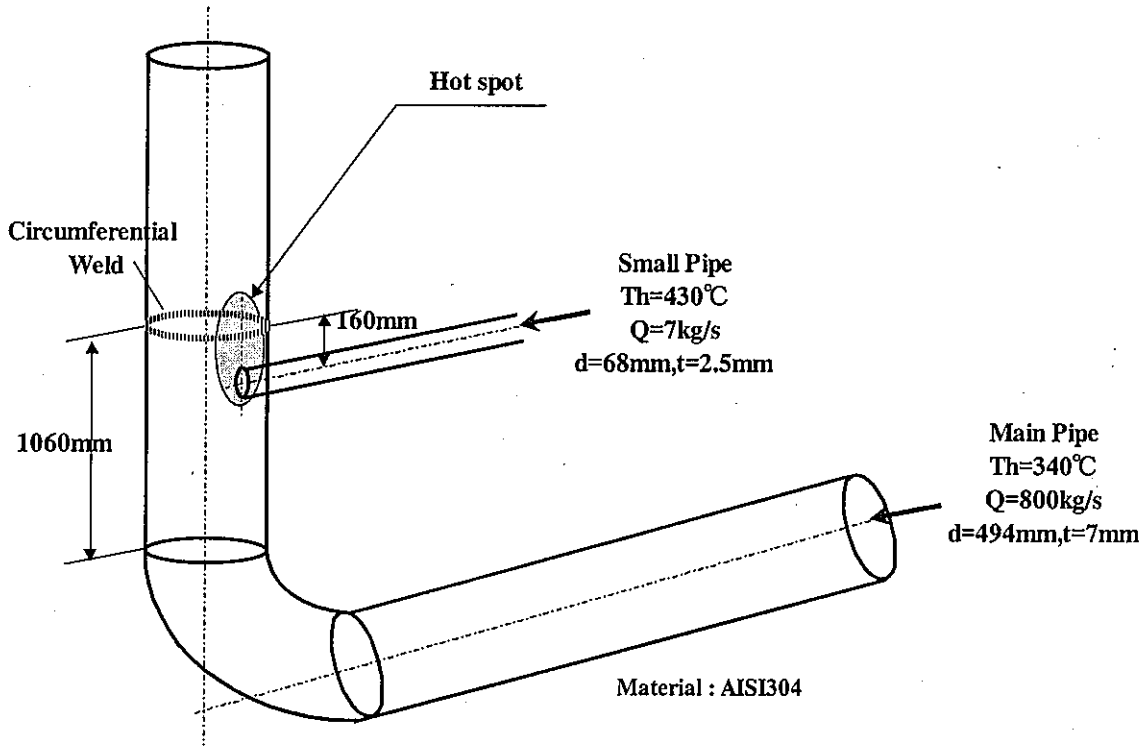

Fig.3.1 Geometrical characteristics of the Phenix Secondary Piping System

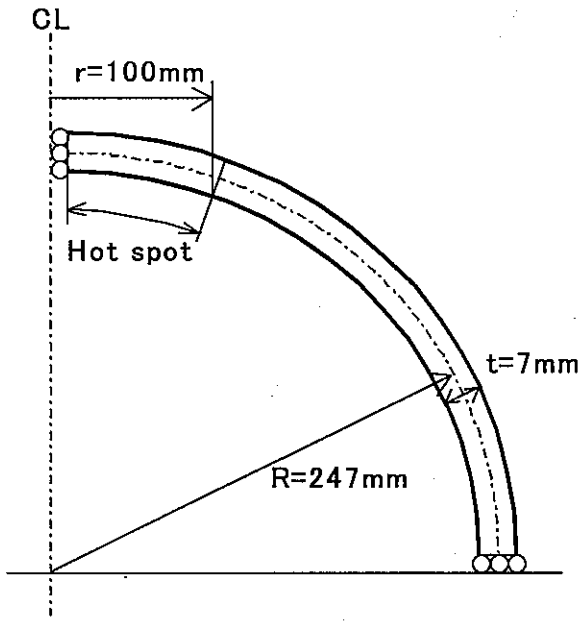

Fig. 3.2 F.E. analysis model of the Phenix Secondary Piping System

Loading conditions are 7 cases described in Table 3.1. Case P-M assumes a hot spot with 430 ℃ homogeneous temperature across the wall (Fig.3.3). Case P-ML considers linear temperature change within 6mm width at the boundary of the hot spot, to avoid singularity at the boundary (Fig.3.4). The purpose of these two cases is to evaluate a constraint efficiency of membrane stress. Case P-B gives a linear temperature gradient across the wall (Fig.3.5). Case P-BL considers linear temperature change at the boundary. Above two cases evaluate a constraint efficiency of bending stress. P-S series are more realistic loads and they take sinusoidal temperature fluctuation of fluid with 14500 kcal/m2h℃) heat transfer coefficient into account (Fig.3.6). These results are utilized for validation.

Table 3.1 Load conditions of the Phenix Secondary Piping System

Cases	Model	Loading	Remark
P-M	Phenix	Membrane stress	Fig.3.3
P-ML	Phenix	Membrane stress with liner change	Fig.3.4
P-B	Phenix	Bending stress	Fig.3.5
P-BL	Phenix	Bending stress with linear change	Fig.3.6
P-S0.01	Phenix	Sinusoidal temperature fluctuation (0.01Hz)	Fig.3.7
P-S0.084	Phenix	Sinusoidal temperature fluctuation (0.084Hz)	Fig.3.7
P-S1.0	Phenix	Sinusoidal temperature fluctuation (1.0Hz)	Fig.3.7

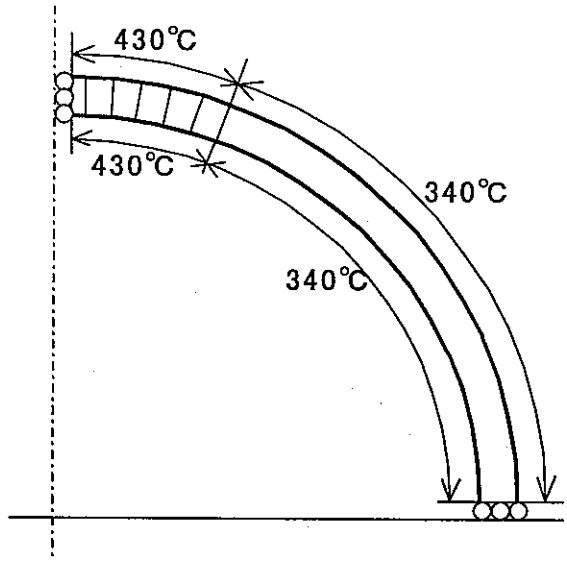

Fig. 3.3 Boundary condition of membrane stress (Case P-M)

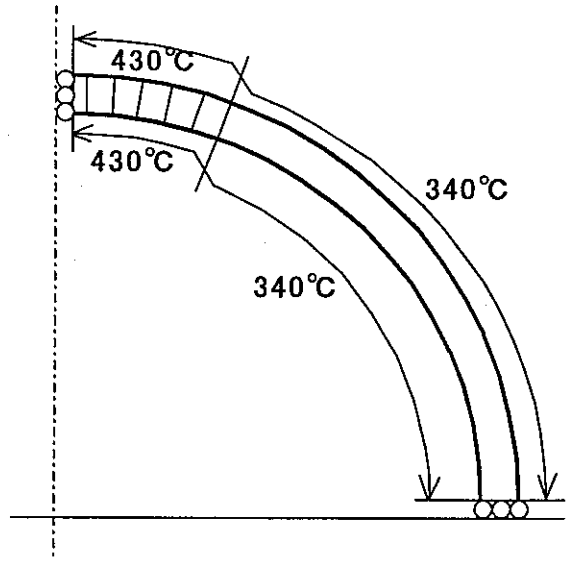

Fig. 3.4 Boundary condition of membrane stress (Case P-ML)

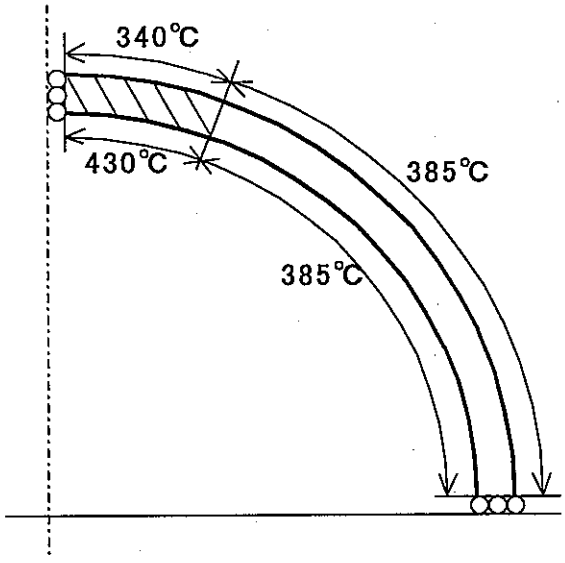

Fig. 3.5 Boundary condition of bending stress (Case P-B)

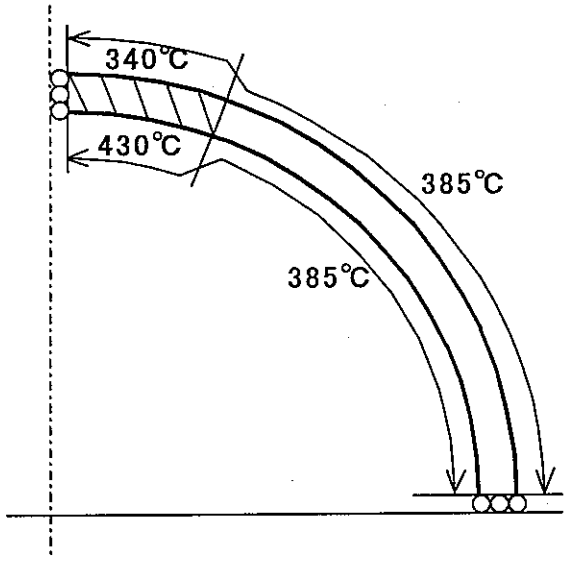

Fig. 3.6 Boundary condition of bending stress (Case P-BL)

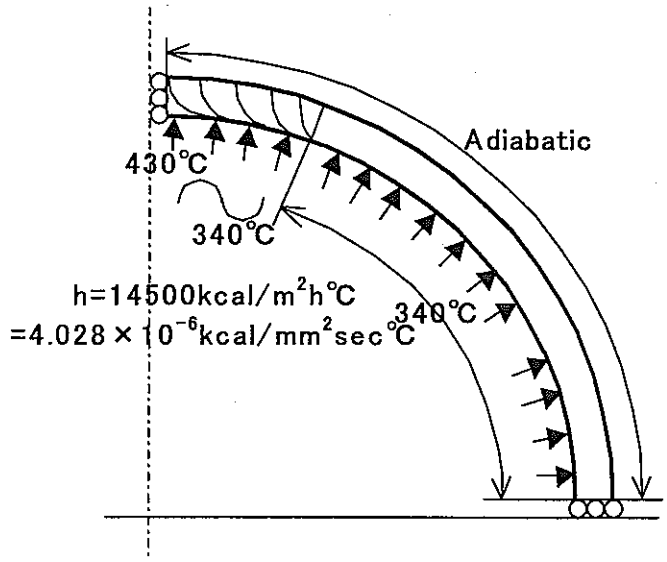

Fig. 3.7 Boundary condition of sinusoidal temperature fluctuation (Case P-S series)

3.2 FINITE ELEMENT ANALYSIS

To investigate mechanism of stress generation and to obtain reference data for validation, finite element analyses have been conducted with mesh models shown in Fig.3.8.

8-nodes quadrilateral axisymmetric elements HQAX8/QAX8 and 3-nodes axisymmetric heat transfer element FCAX3 of the FINAS code [6] were utilized for this calculation. Since temperature dependency of material has few effects [2][3], material properties were assumed as constant values at 385℃. Thermal elastic calculations were performed without consideration of kinematics non-linearity, because there were no influences by large deformations.

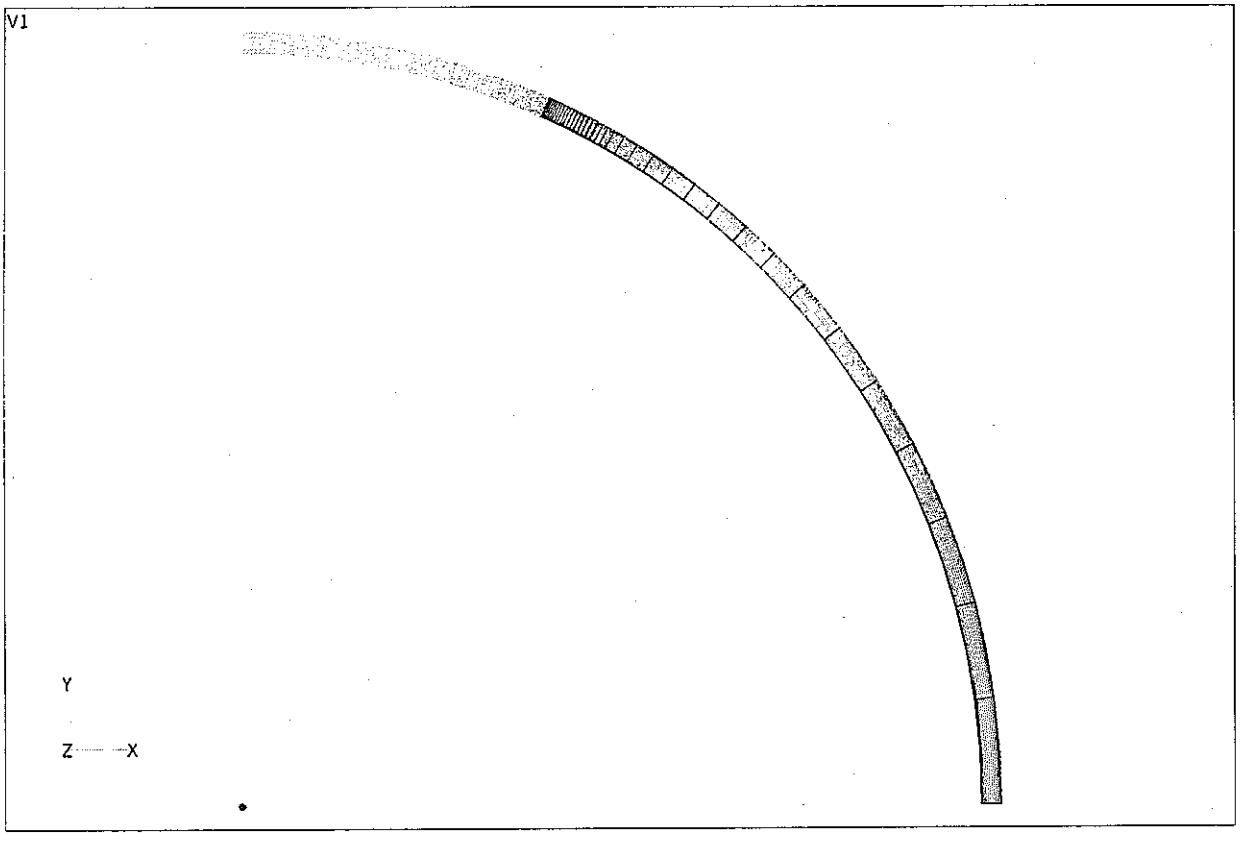

Fig. 3.8 F.E. mesh model of the Phenix Secondary Piping System

Calculated deformations and stress distributions are described here according to a coordinate system shown in Fig.3.9. Output times are ones when a θ stress component becomes the maximum and the minimum.

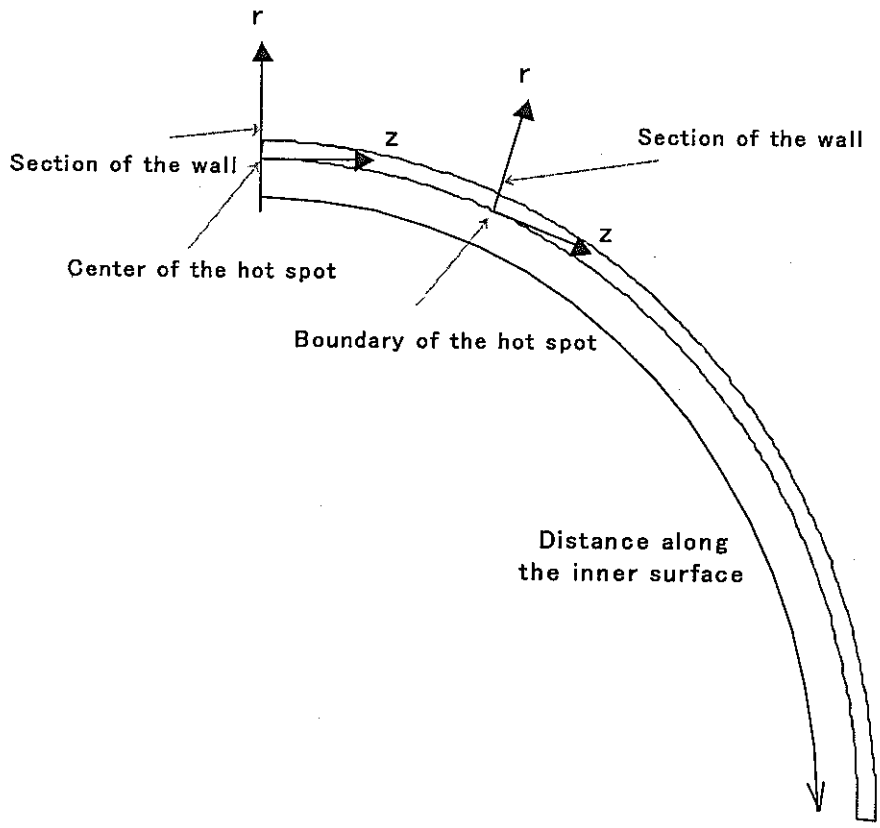

Fig. 3.9 Coordinate system for output

(1) Case P-M

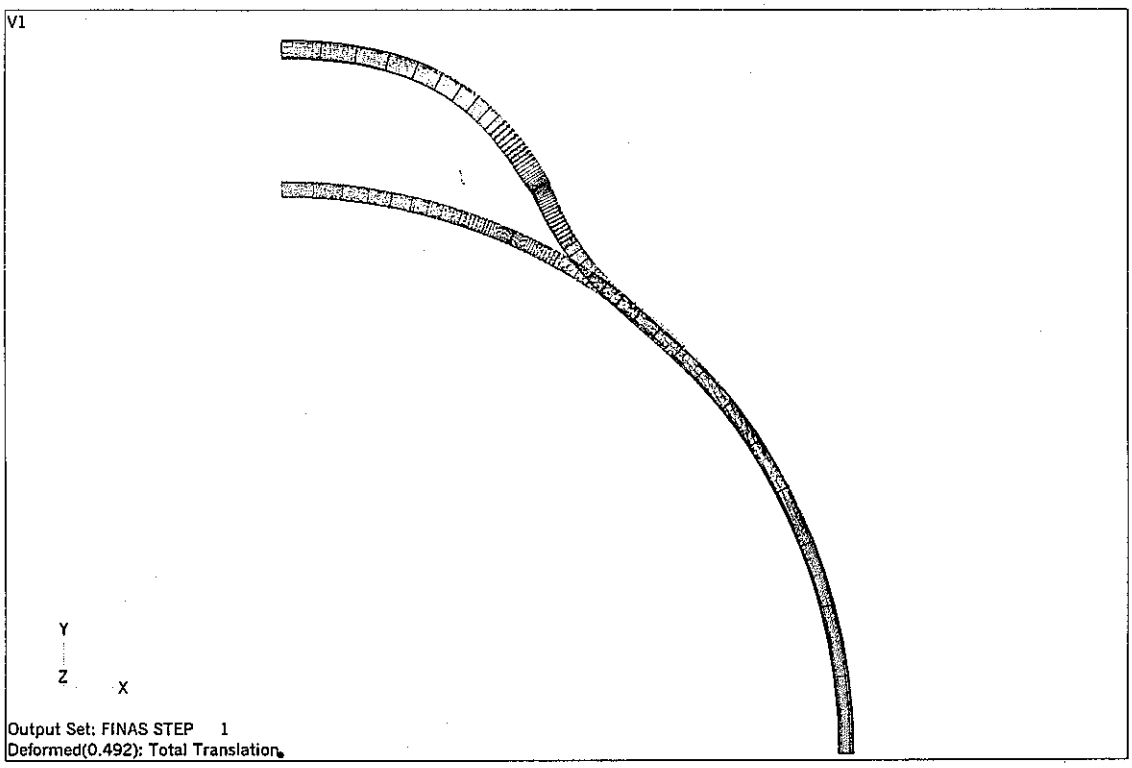

Fig. 3.10 (a) Deformed shape (P-M)

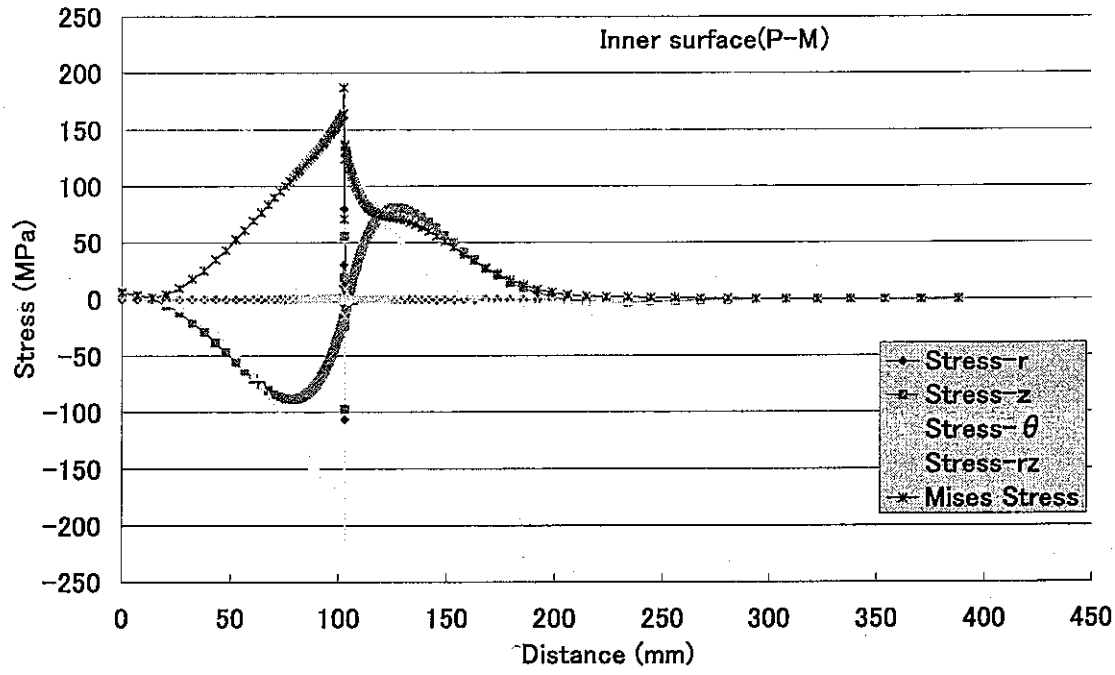

Fig. 3.10 (b) Stress distribution on the inner surface (P-M)

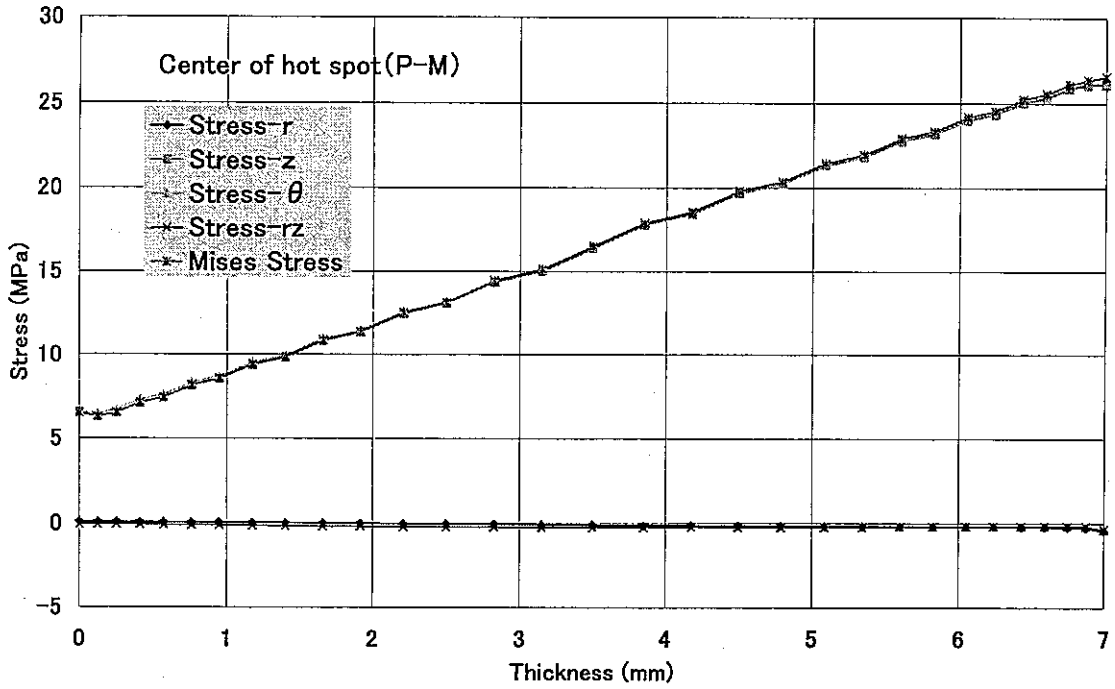

Fig. 3.10 (c) Stress distribution across wall thickness at the center of hot spot (P-M)

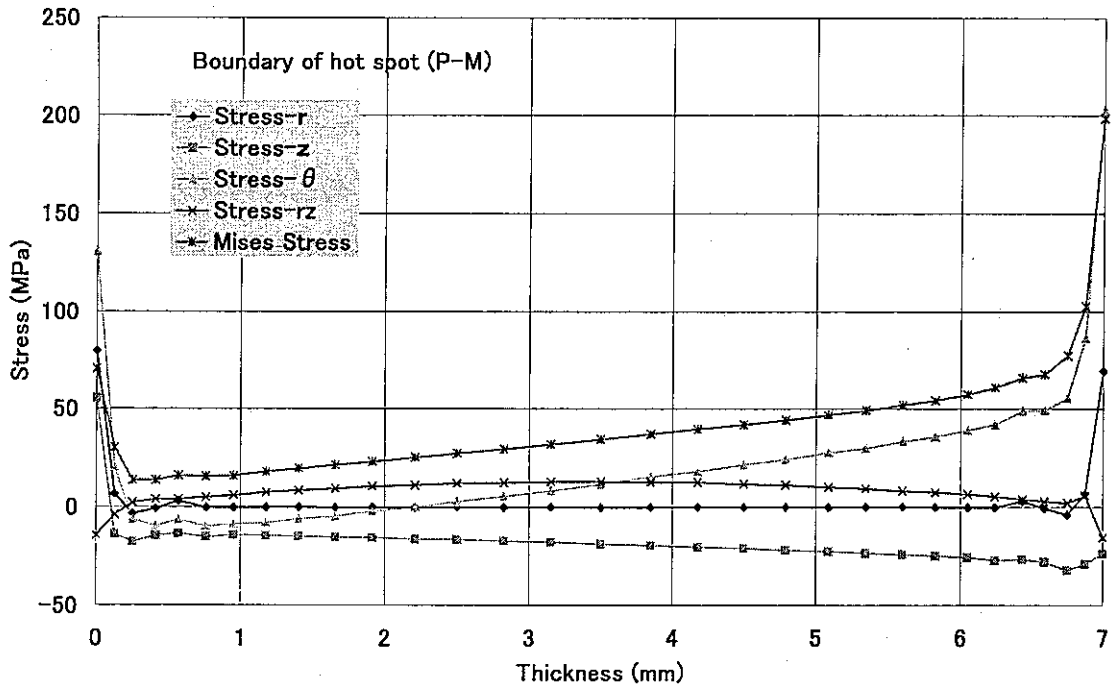

Fig. 3.10 (d) Stress distribution across wall thickness at the boundary of hot spot (P-M)

(2) Case P-ML

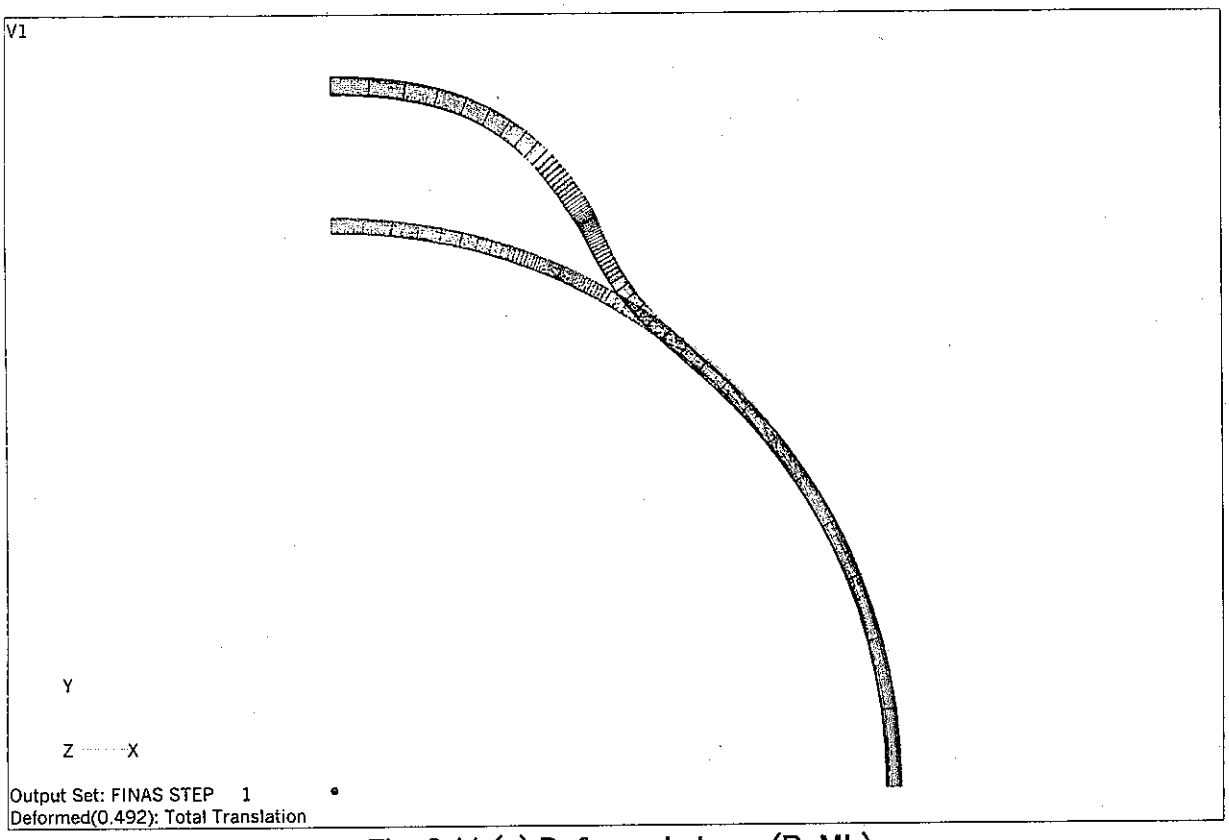

Fig. 3.11 (a) Deformed shape (P-ML)

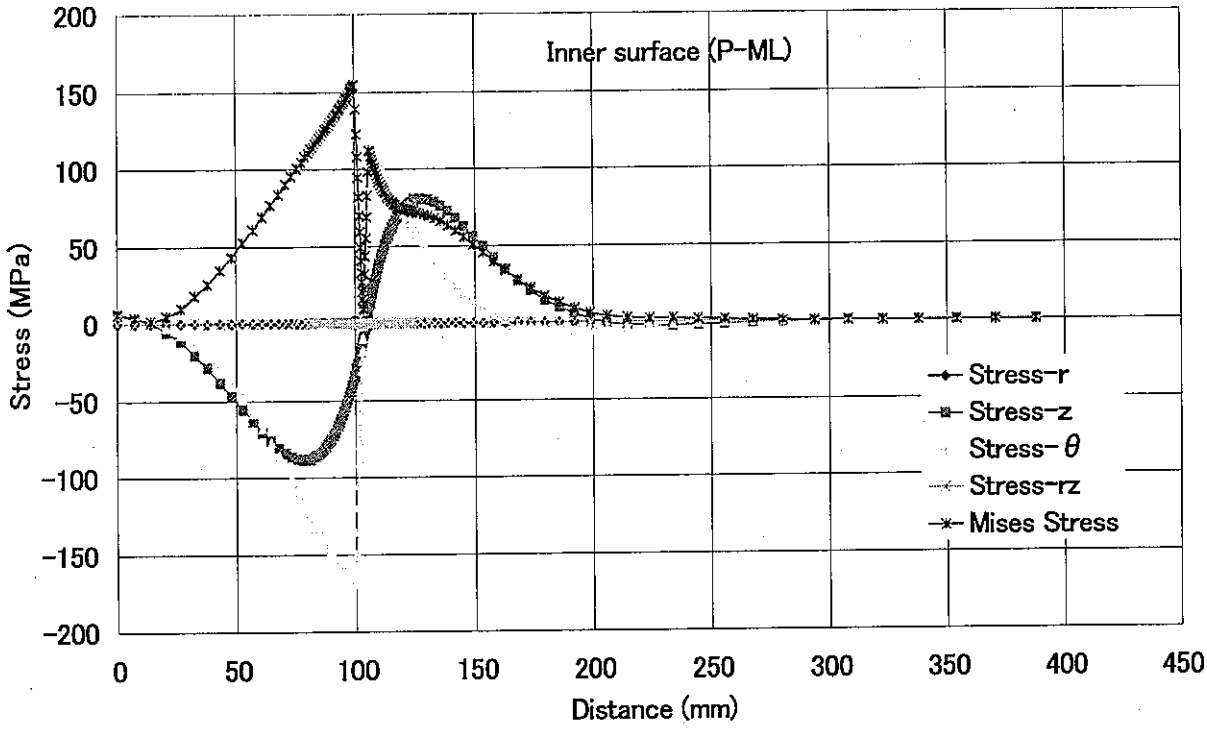

Fig. 3.11 (b) Stress distribution on the inner surface (P-ML)

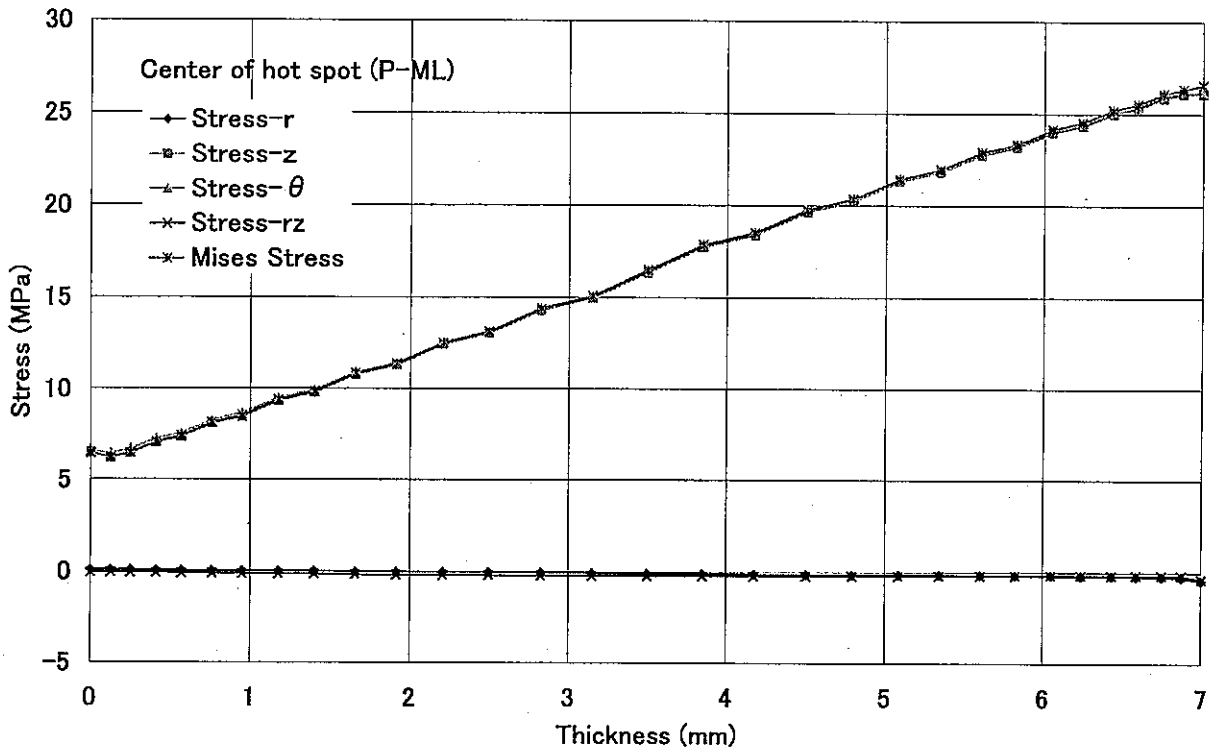

Fig. 3.11 (c) Stress distribution across wall thickness at the center of hot spot (P-ML)

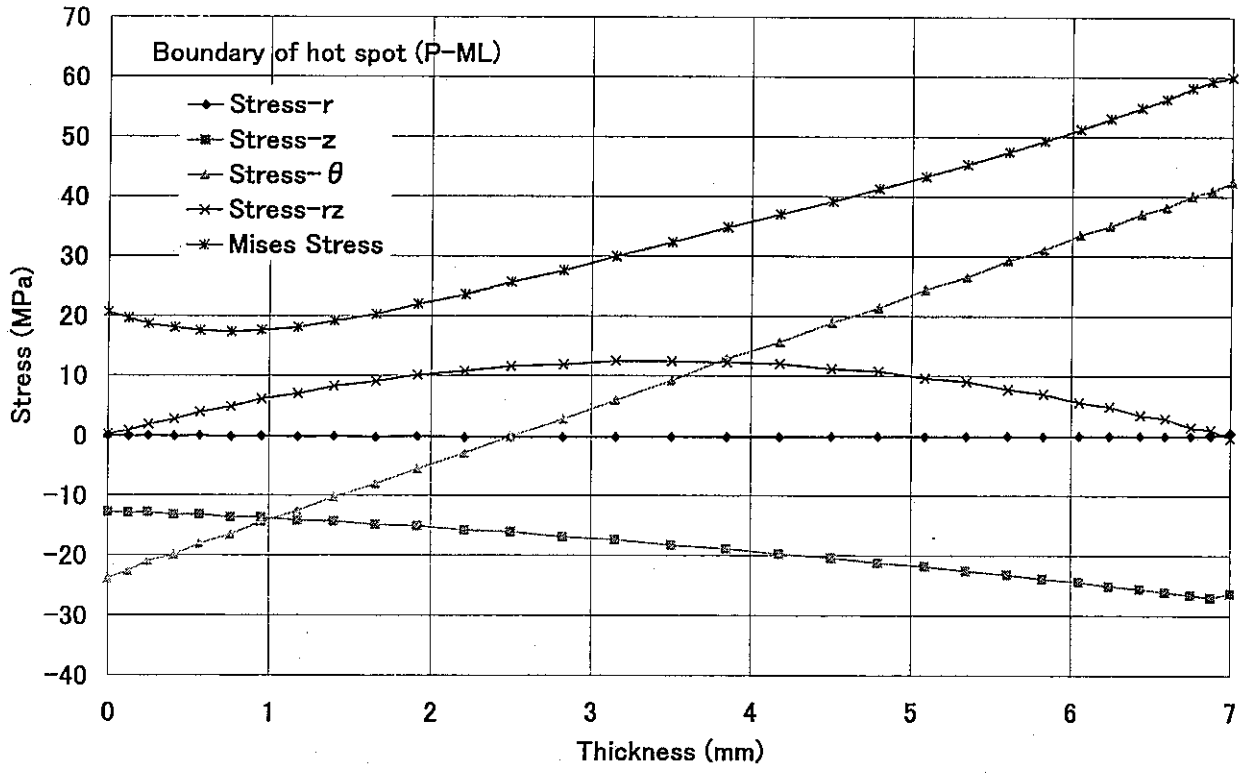

Fig. 3.11 (d) Stress distribution across wall thickness at the boundary of hot spot (P-ML)

(3) Case P-B

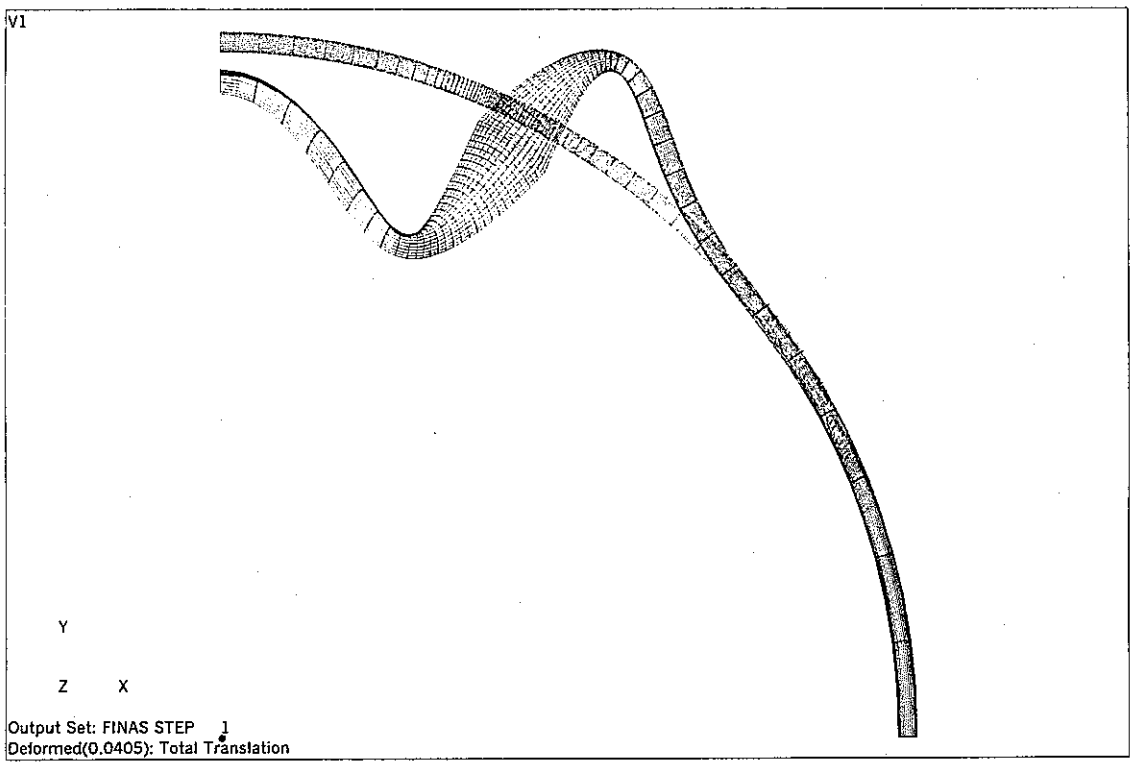

Fig. 3.12 (a) Deformed shape (P-B)

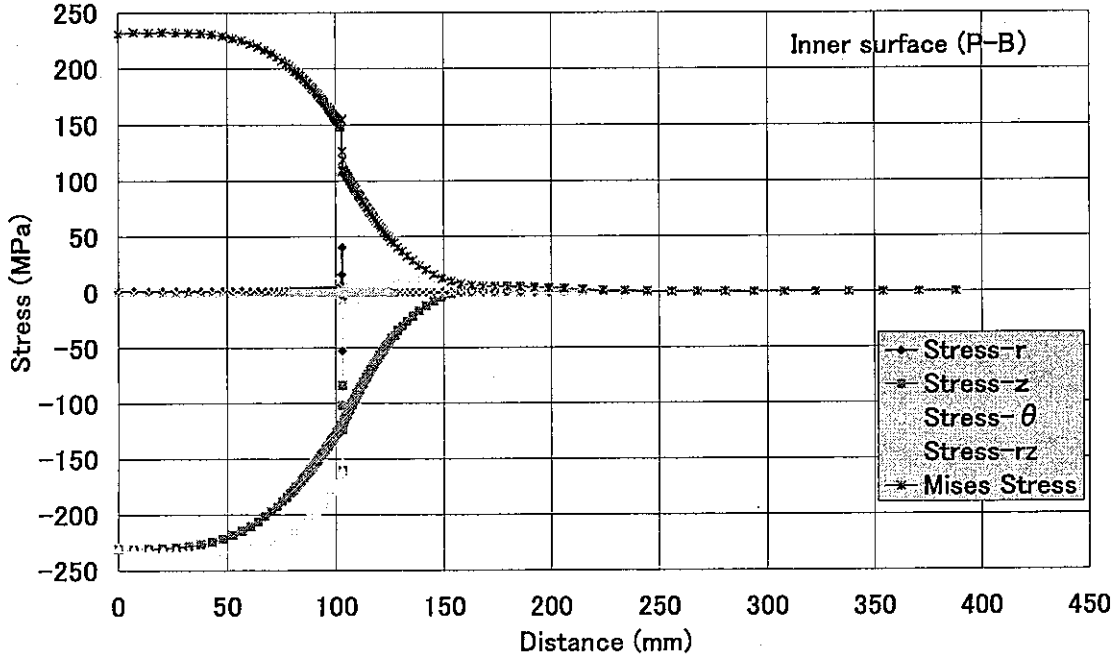

Fig. 3.12 (b) Stress distribution on the inner surface (P-B)

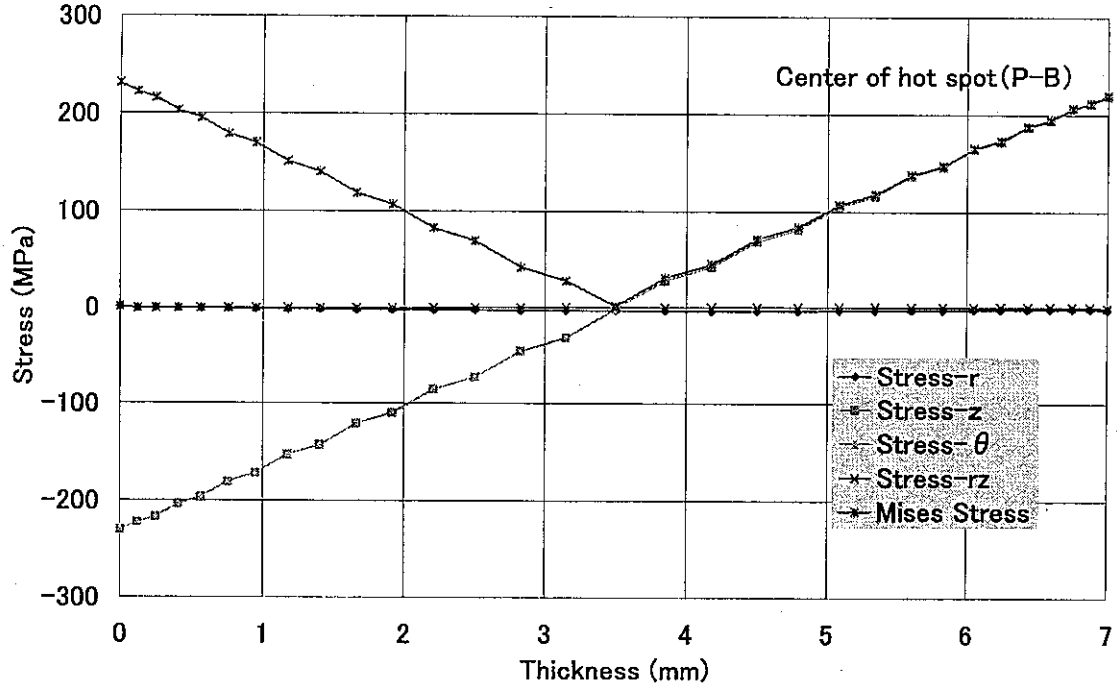

Fig. 3.12 (c) Stress distribution across wall thickness at the center of hot spot (P-B)

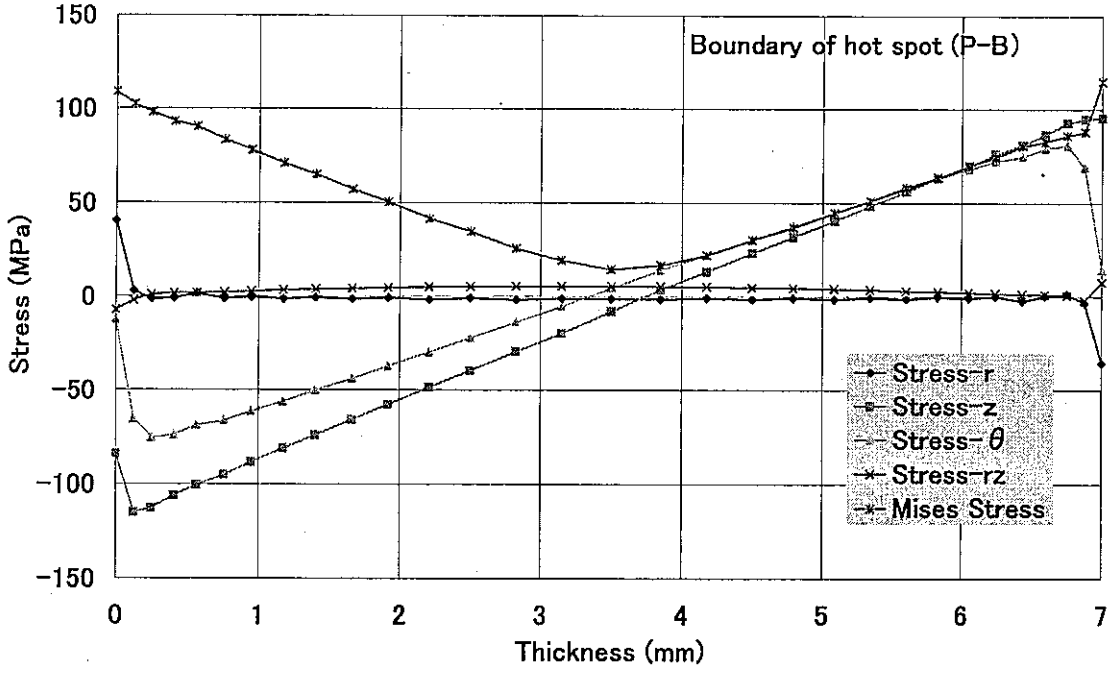

Fig. 3.12 (d) Stress distribution across wall thickness at the boundary of hot spot (P-B)

(4) Case P-BL

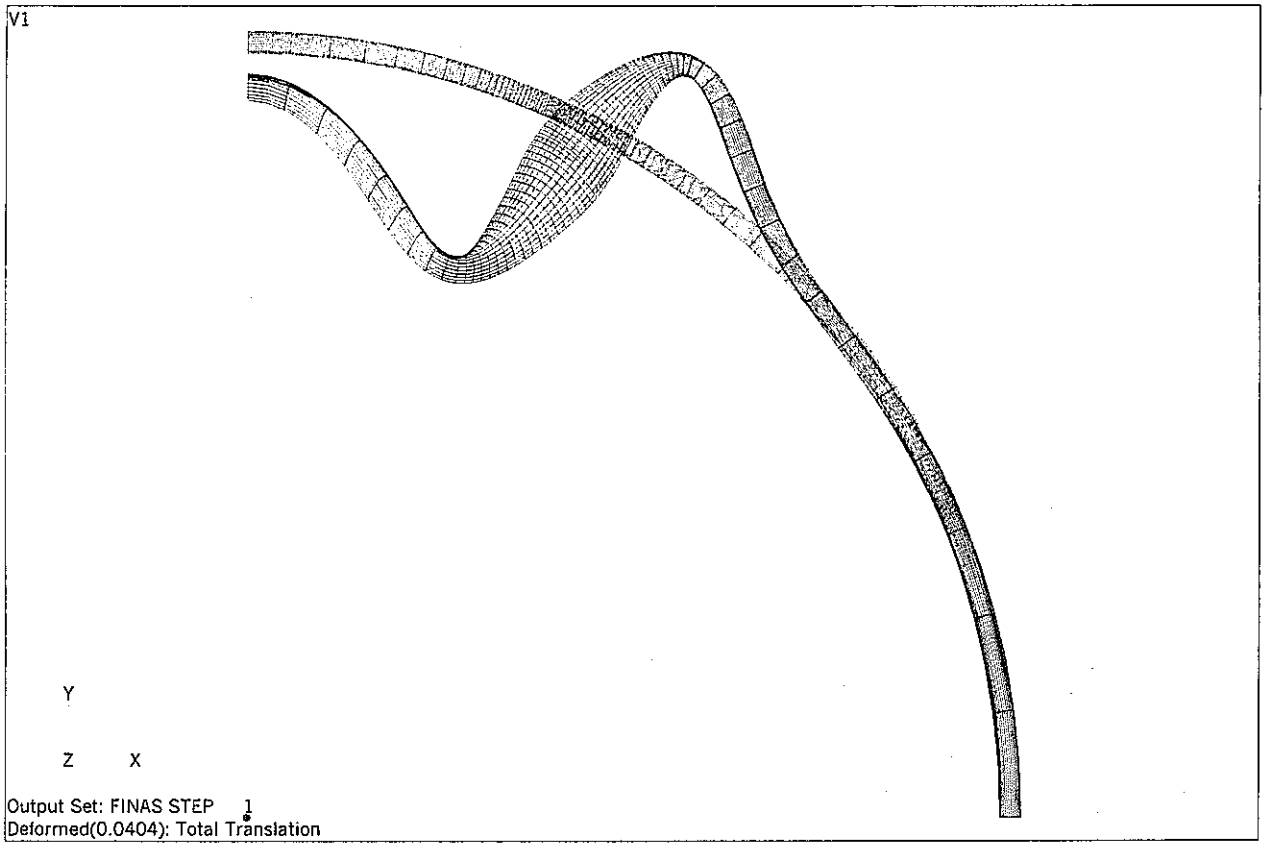

Fig. 3.13 (a) Deformed shape (P-BL)

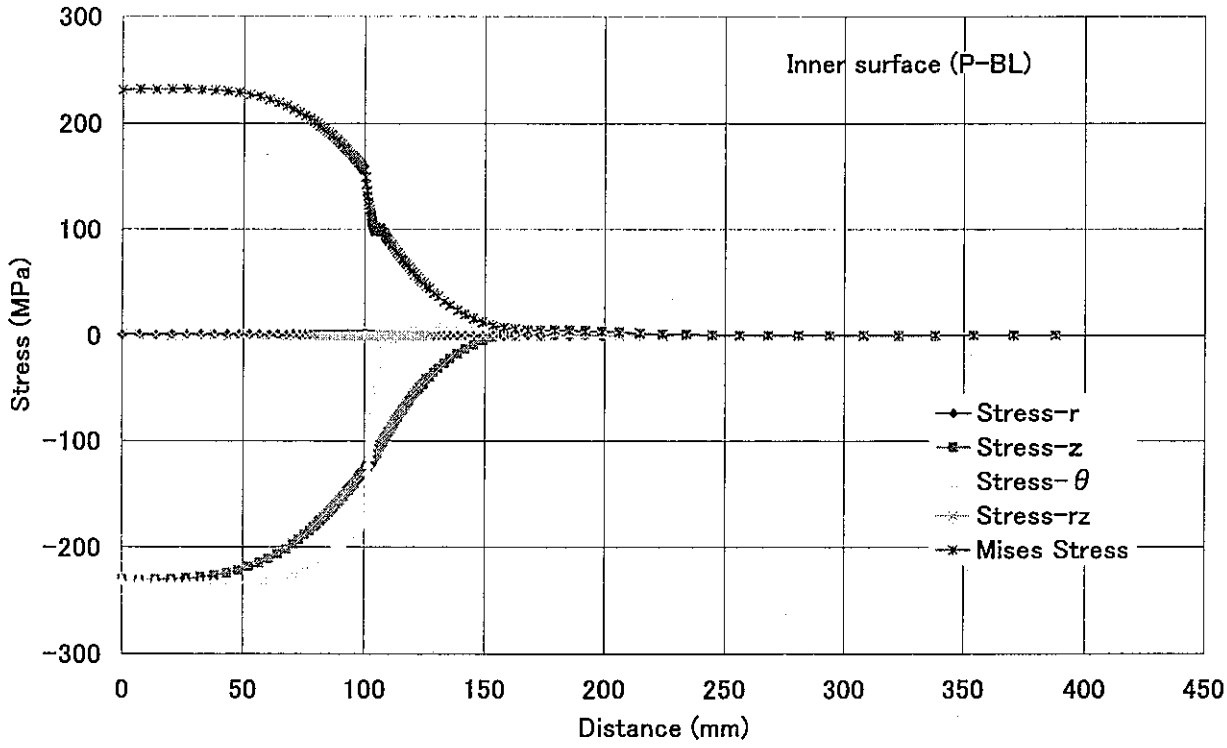

Fig. 3.13 (b) Stress distribution on the inner surface (P-BL)

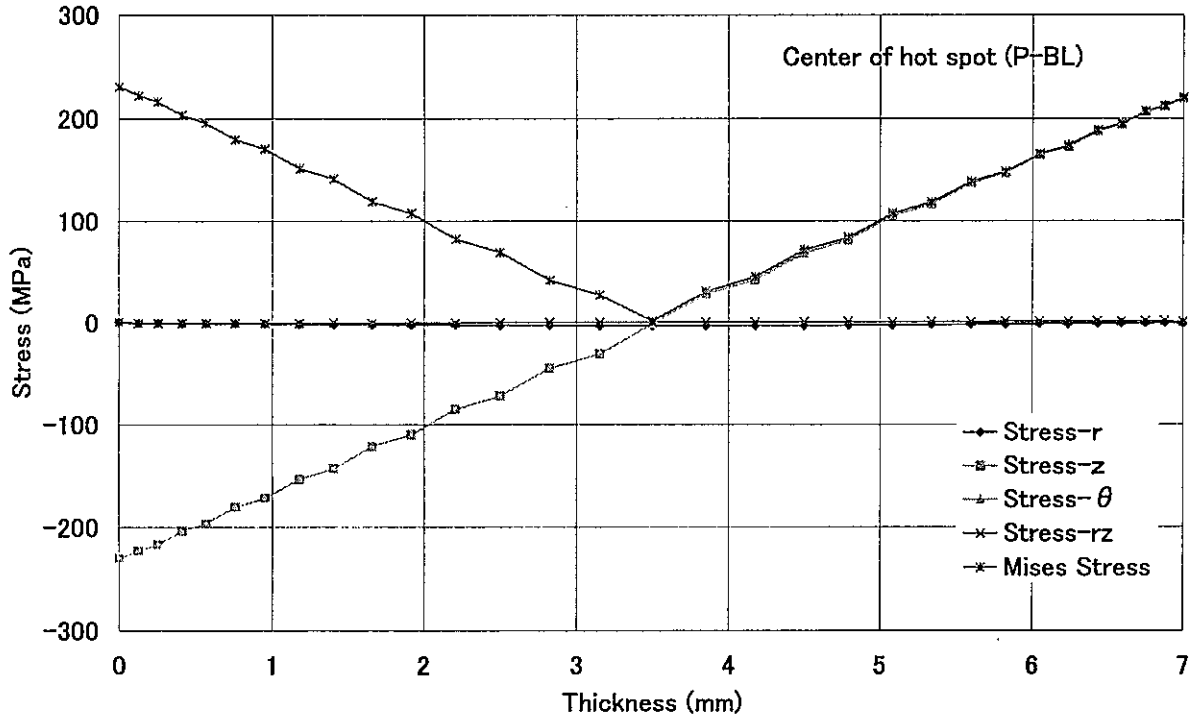

Fig. 3.13 (c) Stress distribution across wall thickness at the center of hot spot (P-BL)

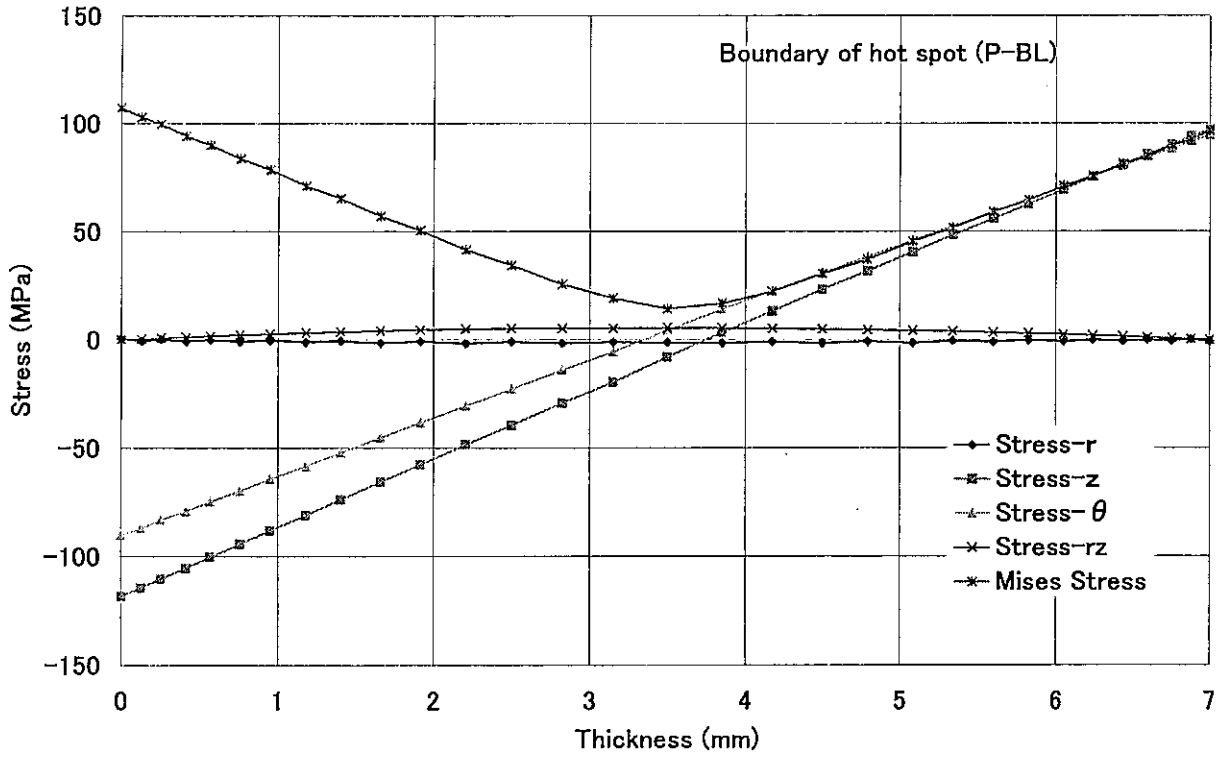

Fig. 3.13 (d) Stress distribution across wall thickness at the boundary of hot spot (P-BL)

From above F.E. calculated results, we can get constraint efficiency factors for membrane and bending stresses.

Factors for membrane stresses are

$$A_m = \frac{|\sigma_C|}{\Delta\sigma^*} \quad \text{(Center of spot),} \tag{3.1}$$

$$A_m = \frac{|\sigma_i|}{\Delta\sigma^*} \quad \text{(Boundary of spot) and} \tag{3.2}$$

$$A_m = \frac{\max(|\sigma_c - \sigma_o|, |\sigma_i - \sigma_o|)}{\Delta\sigma^*} \quad \text{(Moving spot).} \tag{3.3}$$

Factors for bending stresses are

$$A_b = \frac{|\sigma_C|}{\Delta\sigma^*/2} \quad \text{(Center of spot),} \tag{3.4}$$

$$A_b = \frac{|\sigma_i|}{\Delta\sigma^*/2} \quad \text{(Boundary of spot) and} \tag{3.5}$$

$$A_b = \frac{\max(|\sigma_c - \sigma_o|, |\sigma_i - \sigma_o|)}{\Delta\sigma^*/2} \quad \text{(Moving spot).} \tag{3.6}$$

The next table shows evaluated constraint efficiency factors.

Table 3.2 Constraint efficiency factors by F.E. caluculation

Case	F.E.Calculated Mises Stress (MPa)			$\Delta\sigma^*$(MPa)=	Ratio A_m		
	Center of hot spot σc	Bounday inside hot spot σi	Bounday outside hot spot σo	$E\alpha/(1-\nu)\cdot\Delta T_t$	$\lvert\sigma_c\rvert/\Delta\sigma^*$	$\lvert\sigma_i\rvert/\Delta\sigma^*$	$\max(\lvert\sigma_c-\sigma_o\rvert,\lvert\sigma_i-\sigma_o\rvert)/\Delta\sigma^*$
P-ML (Membrane)	6.42	-169	116.00	420.86	0.015	0.402	0.68
					Ratio A_b		
					$\lvert\sigma_c\rvert/(\Delta\sigma^*/2)$	$\lvert\sigma_i\rvert/(\Delta\sigma^*/2)$	$\max(\lvert\sigma_c-\sigma_o\rvert,\lvert\sigma_i-\sigma_o\rvert)/(\Delta\sigma^*/2)$
P-BL (Bending)	-230	-173	10.60	420.86	1.093	0.822	1.14

(5) Case P-S series

In the cases of P-S series, times when stresses become maximum and minimum are different among different positions. Therefore stress ranges defined by

$$\Delta\sigma_{eq} = \frac{1}{\sqrt{2}}\sqrt{(\Delta\sigma_r - \Delta\sigma_z)^2 + (\Delta\sigma_z - \Delta\sigma_\theta)^2 + (\Delta\sigma_\theta - \Delta\sigma_r)^2 + 6\Delta\tau_{rz}^{\ 2}}\ . \qquad (3.7)$$

are utilized.

The next figure shows distribution of stress ranges on the surface.

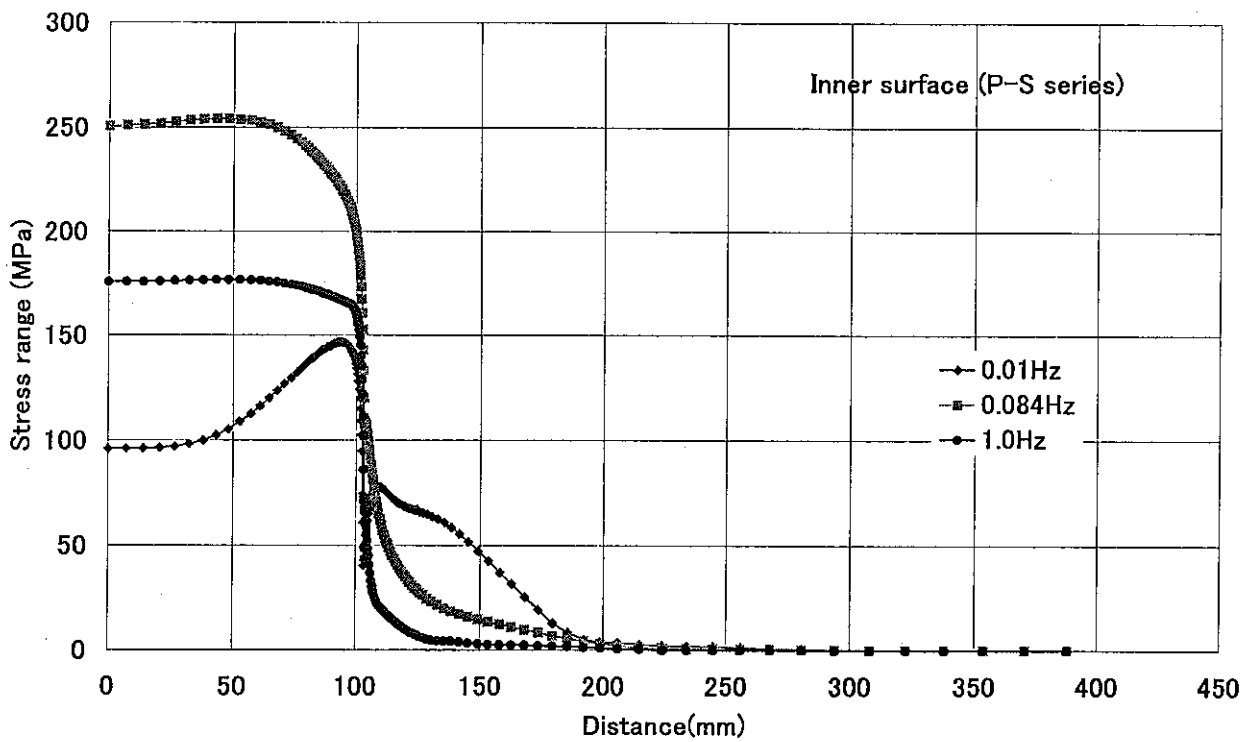

Fig. 3.14 Stress range distribution on the inner surface (P-S series)

From above figure, gains of P-S series defined by the ratio of surface stress $\Delta\sigma_{eq}$ to $\Delta\sigma^*$ were evaluated as in the next table and the frequency diagram.

Table 3.3 Gains of thermal stress of P-S series by F.E. calculation

Case	F.E.calculated stress range (MPa)		$\Delta\sigma^*=$	Gain	
	Center of hot spot $\Delta\sigma c$	Bounday inside hot spot $\Delta\sigma i$	$E\alpha/(1-\nu)\cdot\Delta Tf$ (MPa)	$\lvert\Delta\sigma c/\Delta\sigma^*\rvert$	$\lvert\Delta\sigma i/\Delta\sigma^*\rvert$
P-S0.01	97.00	160.00	420.86	0.230	0.380
P-S0.084	250.00	239.40	420.86	0.594	0.569
P-S1.0	178.70	175.30	420.86	0.425	0.417

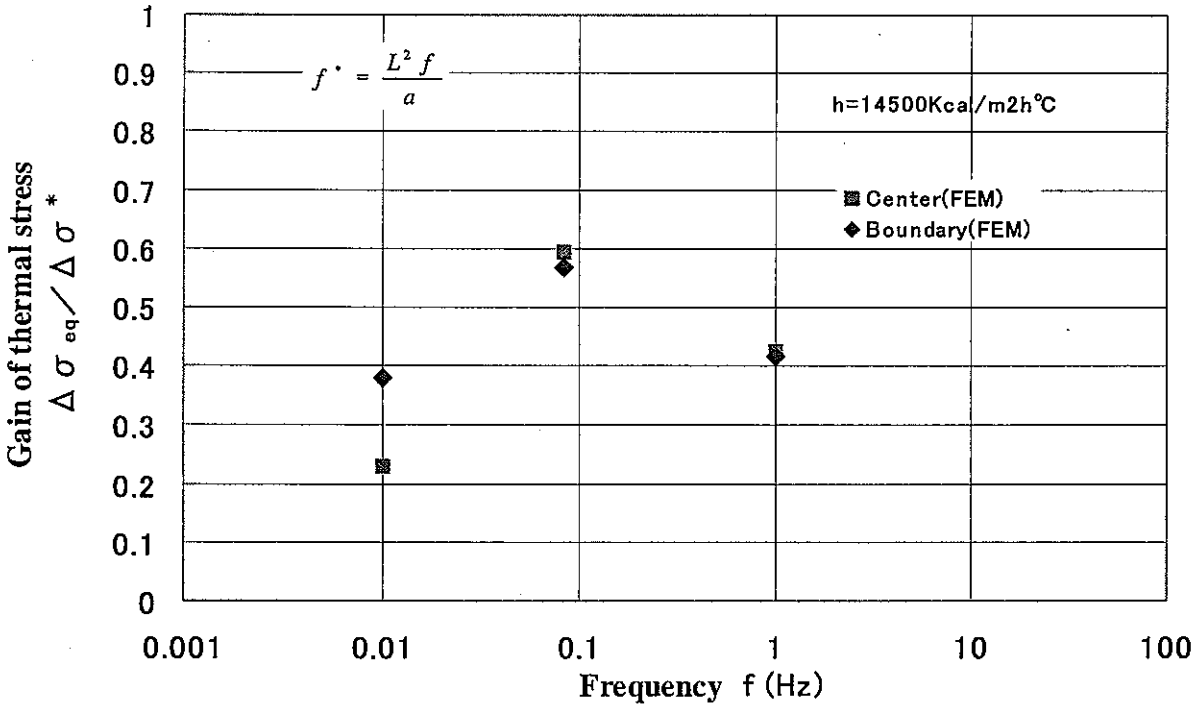

Fig. 3.15 F.E. calculated gains of thermal stress on the inner surface (P-S series)

3.3 EVALUATION WITH THE FREQUENCY RESPONSE FUNCTION

From Table 3.2, we can get the constraint efficiency factors as

A_m=0.015, A_b=1 (For center) (3.8)

A_m=0.40, A_b=0.82 (For boundary) (3.9)

When inputting above factors and Biot number Bi=6.02 that corresponds to 14500 kcal/m^{2}h℃ into Eq.(2.9), we can get stress response diagrams as in the next figure.

Predictions by these diagrams agree well with gains of Table 3.2 as in the next figure.

It means that the extended frequency response function with the constraint efficiency factors can predict thermal stresses induced by hot/cold spots.

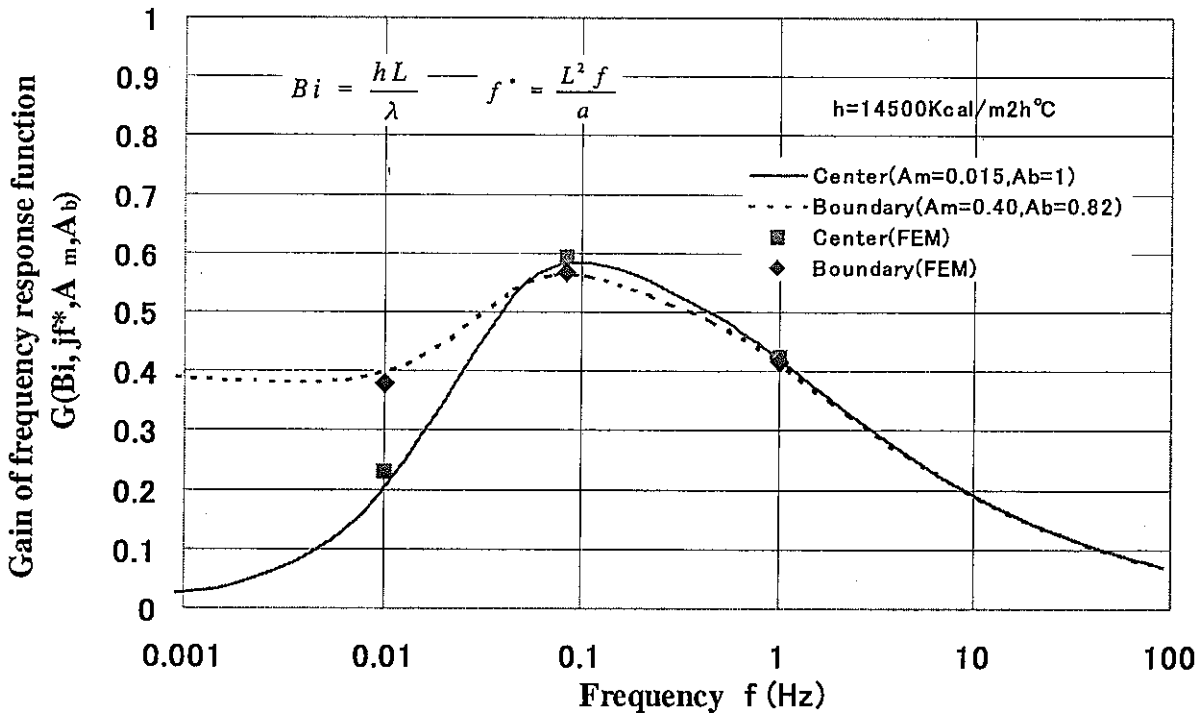

Fig. 3.16 Frequency response diagrams with F.E. calculated gains

4. APPLICATION TO TIFFSS-4

4.1. HOT/COLD SPOT PROBLEM IN TIFFSS-4 SODIUM EXPERIMENT

The specimen is a plate (50mm * 50mm * 10t mm) made of 316FR with a thermal insulator [2]. Its insulator is a ceramic plate made of Si_3N_4 with a 15mm diameter hole. The specimen is submitted to temperature fluctuations inside this hole and a surrounded portion keeps less temperature amplitudes. The configuration of specimen with a thermal insulator is shown as in Fig.4.1.

Hot and cold sodium is alternatively projected to the center of a specimen through a single nozzle by the TIFFSS facility (Fig.4.2). Distance between bottom of the nozzle and surface of the specimen is 5.5 mm. Flow rate at the exit nozzle is constant as 1.2 l/min (approximately 0.7m/s) in the nozzle). This value was adjusted to achieve the maximum temperature amplitude since flow rates are limited by capacity of a cooler and small flow rates are affected by heat capacity of the nozzle. Temperature amplitude at the nozzle keeps the constant value such as 240℃(470℃ - 230℃). Frequencies of temperature fluctuation are 0.04Hz, 0.1Hz and 0.2Hz. Heat transfer coefficient is 13300 kcal/m^{2}h℃ that corresponds to Biot number 8.19 [3].

Distributions of temperature range on the upper surface of the specimen were measured by thermocouples attached on the surface. Fig.4.3 and Table 4.1 show locations of thermocouples. Measured data were described in Table 4.2 and Fig.4.4. These results mean that temperature range changes gradually around the edge of the hole. This temperature gradient may influence on constraint effects. In this study, frequency response of TIFFSS-4 is examined with considering gradual temperature change.

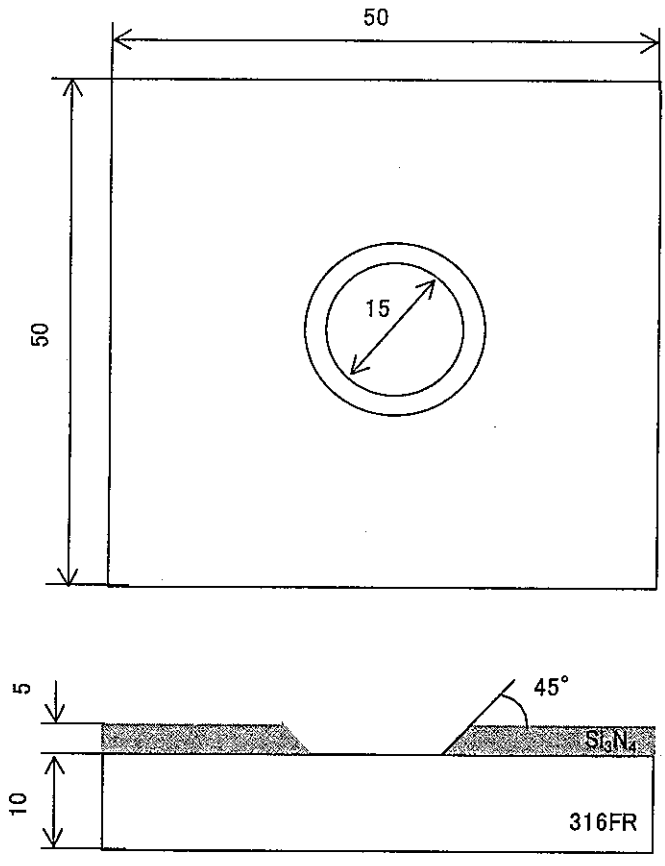

Fig.4.1 Configuration of a plate specimen with thermal insulator for TIFFSS-4 fatigue test

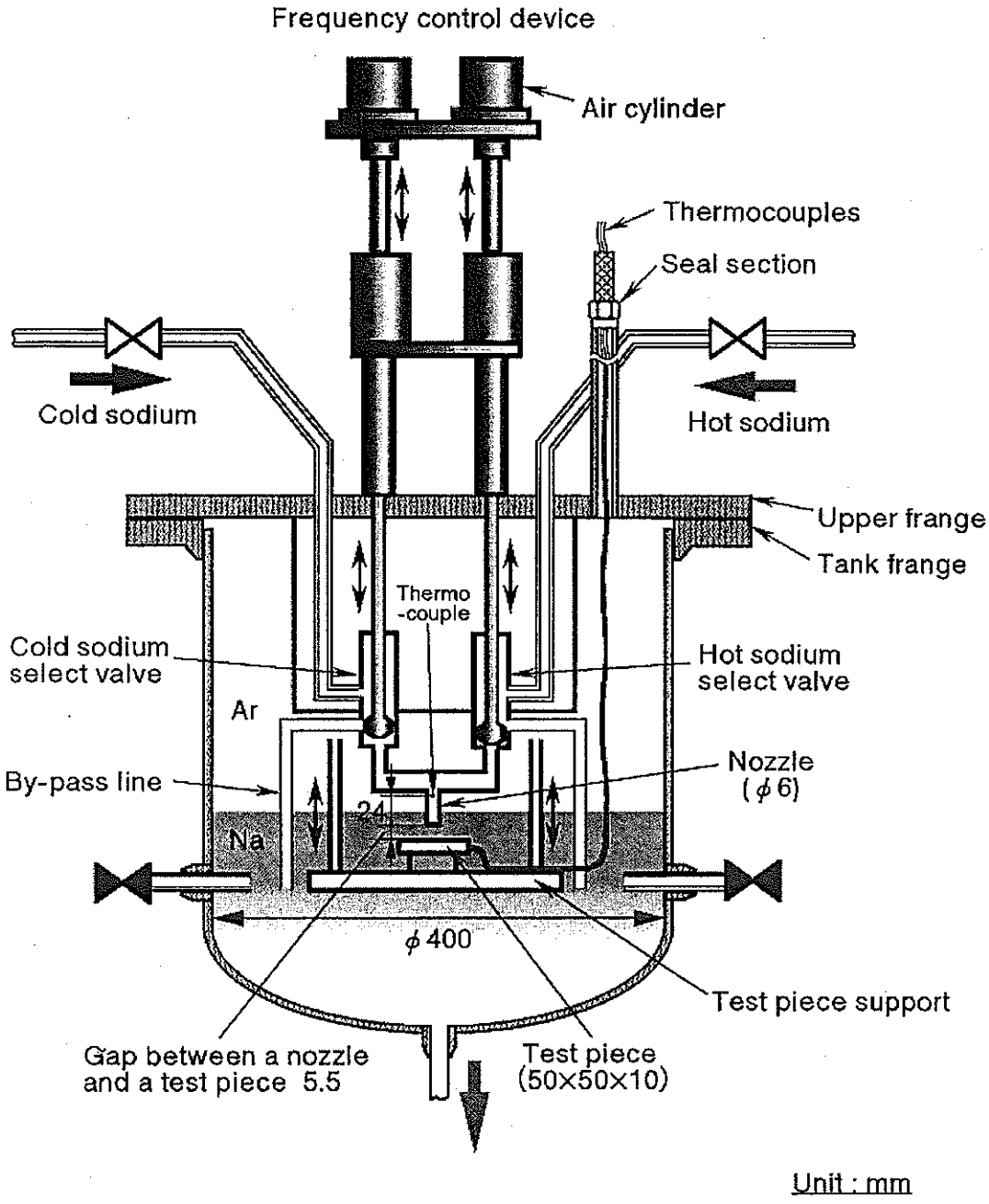

Fig.4.2 Details of TIFFSS test section

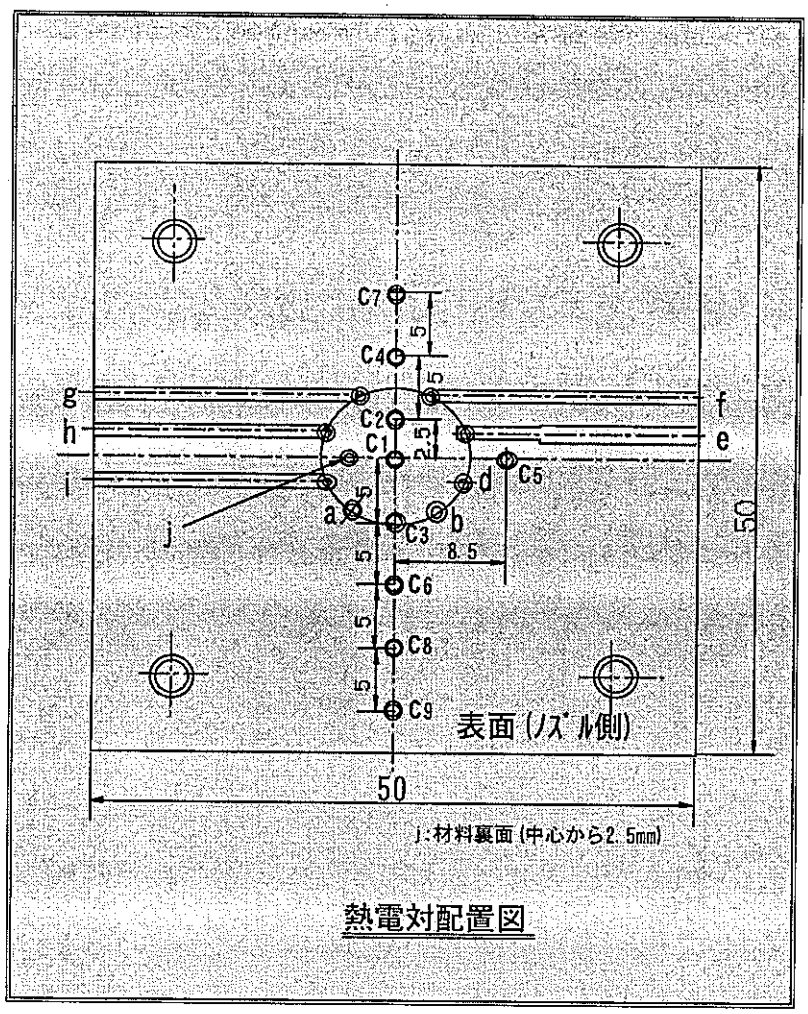

Fig.4.3 Location of thermocouples in the constraint plate specimen

Table 4.1 Thermocouples on the surface of the specimen

TC No.	Horizontal distance from the center of the specimen
c1	0mm (Center)
c2	2.5mm
c3	5mm
c4	7.5mm
c5	8.5mm
c6	10mm
c7	12.5mm
c8	15mm
c9	20mm

Table 4.2 Measured temperature range on the surface of the specimen

TC-No	Distance	0.04Hz	0.1Hz	0.2Hz
c1	0	202.275	184.125	162.975
c2	2.5	200.825	182.425	160.4
c3	5	201.125	182	160.75
c4	7.5	180.65	153.55	124.225
c5	8.5	161.1	125.9	66.9
c6	10	144.075	76.225	31.175
c7	12.5	115.25	53.675	15.2
c8	15	99.775	49	6.475
c9	20	85.725	32.7	14.3
Nozzle		239.03	239.9	240.2

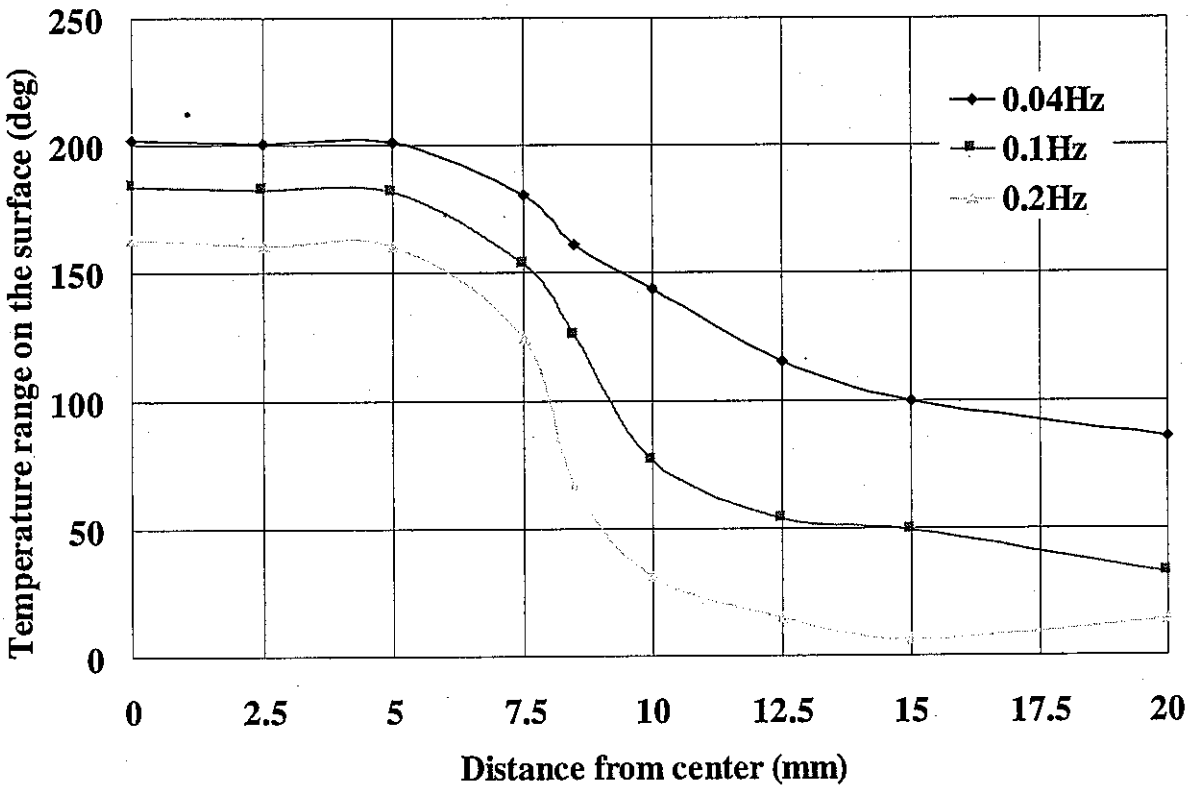

Fig.4.4 Thermocouples on the surface of the specimen

To study TIFFSS-4 problem, a 10mm-thickness and 10000mm radius partial sphere shell was assumed considering out of plane bending as in Fig.4.5.

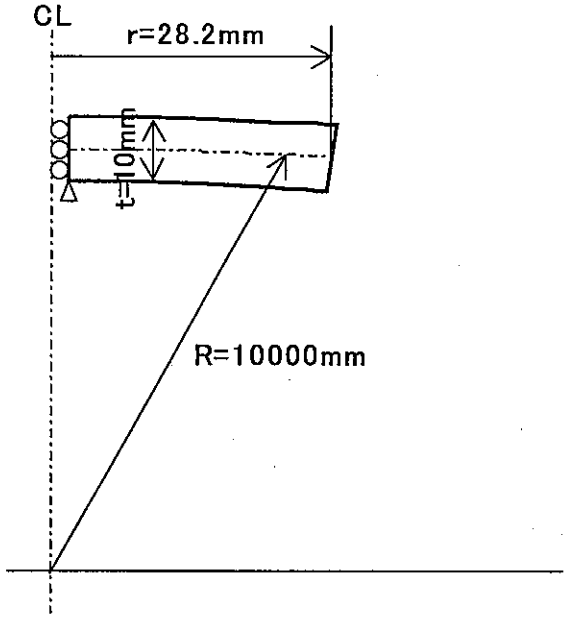

Fig.4.5 F.E. analysis model of TIFFSS-4

Loading conditions are 6 cases described in Table 4.3. Case T-ML series assume a hot spot with 470 ℃ homogeneous temperature across the wall and consider linear temperature change within 5,10,15mm width at the boundary of the hot spot as in Fig.4.6. The purpose of these cases is to evaluate a constraint efficiency of membrane stress. Case T-BL series give a linear temperature gradient across the wall with linear temperature change at the boundary as in Fig.4.7. These cases evaluate a constraint efficiency of bending stress.

Table 4.3 Load conditions of TIFFSS-4

Cases	Model	Loading	Remark
T-ML1	TIFFSS-4	Membrane stress with 5mm width linear change	Fig.4.6
T-ML2	TIFFSS-4	Membrane stress with 10mm width linear change	Fig.4.6
T-ML3	TIFFSS-4	Membrane stress with 15mm width linear change	Fig.4.6
T-BL1	TIFFSS-4	Bending stress with 5mm width linear change	Fig.4.7
T-BL2	TIFFSS-4	Bending stress with 10mm width linear change	Fig.4.7
T-BL3	TIFFSS-4	Bending stress with 15mm width linear change	Fig.4.7

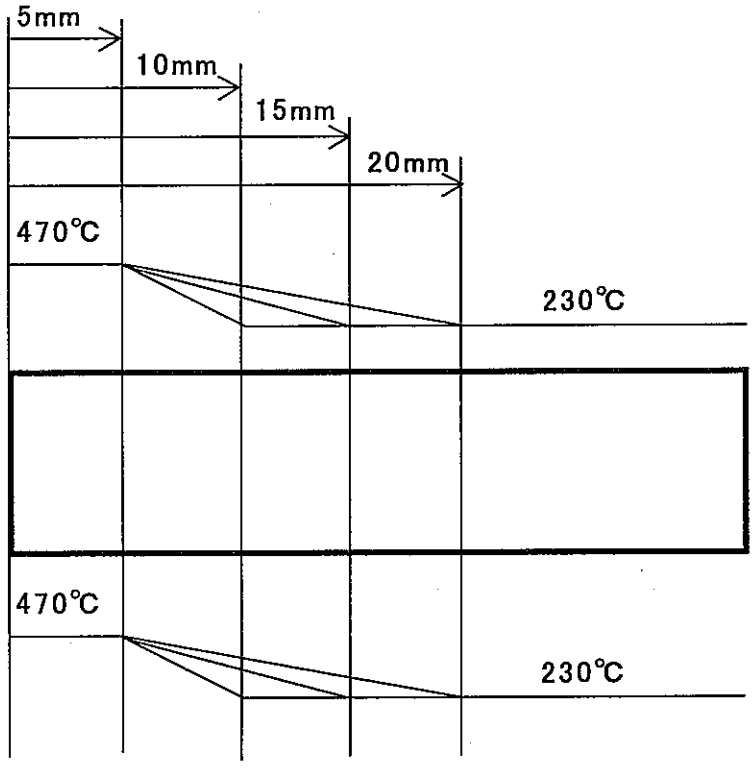

Fig. 4.6 Boundary condition of membrane stress (Case T-ML series)

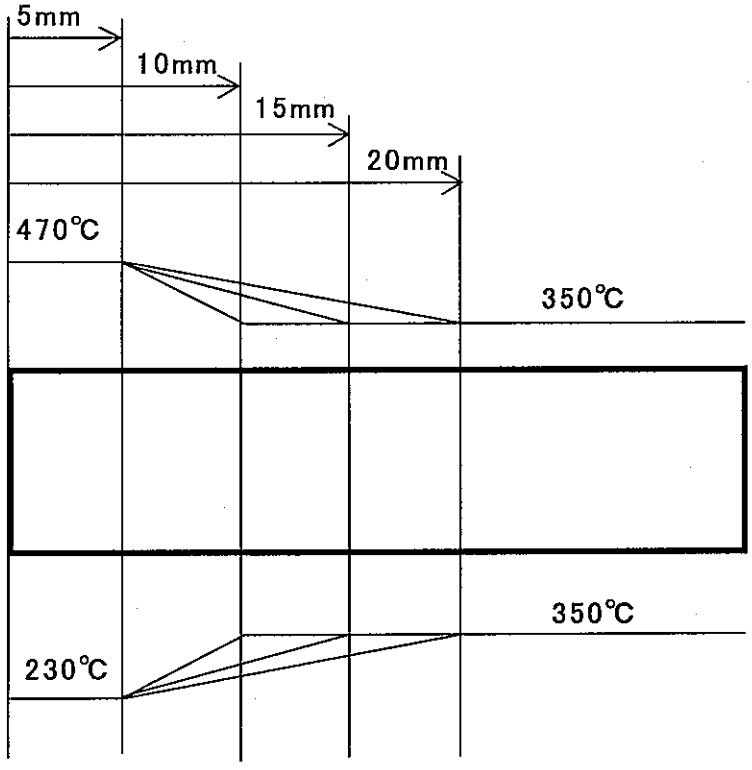

Fig. 4.7 Boundary condition of bending stress (Case T-BL series)

4.2 FINITE ELEMENT ANALYSIS

To investigate mechanism of stress generation and to obtain constraint efficiency factors, finite element analyses have been conducted with mesh models shown in Fig.4.8.

8-nodes quadrilateral axisymmetric elements HQAX8/QAX8 of the FINAS code [6] were utilized for this calculation. Since temperature dependency of material has few effects [2][3], material properties were assumed as constant values at 350℃. Thermal elastic calculations were performed.

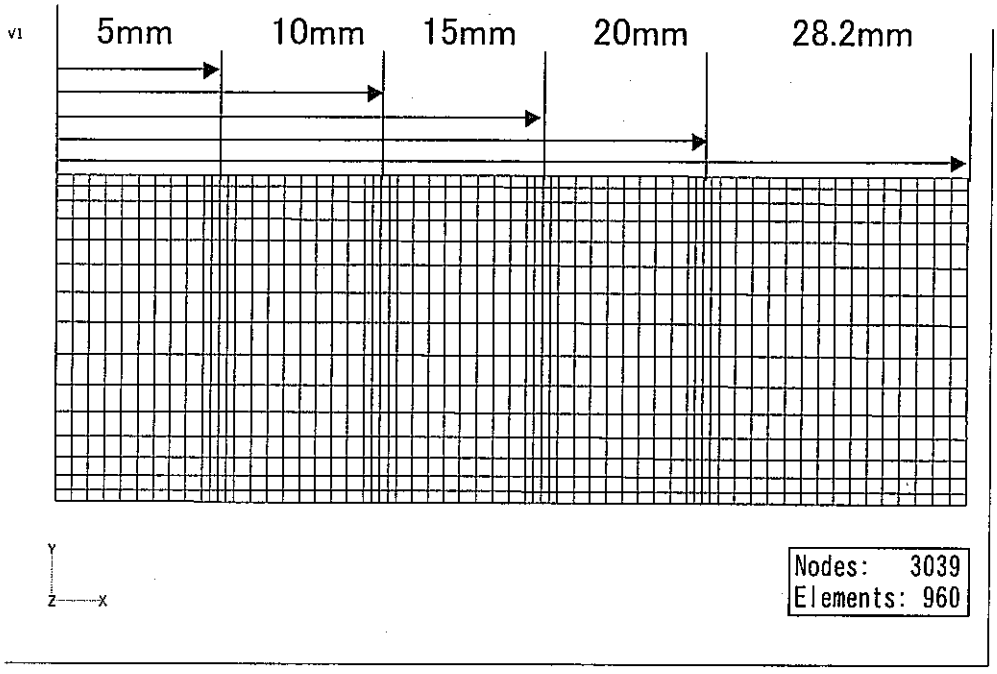

Fig. 4.8 F.E. mesh model of the TIFFSS-4 specimen

Calculated deformations and stress distributions on the surface are described here according to a coordinate system shown in Fig.4.9.

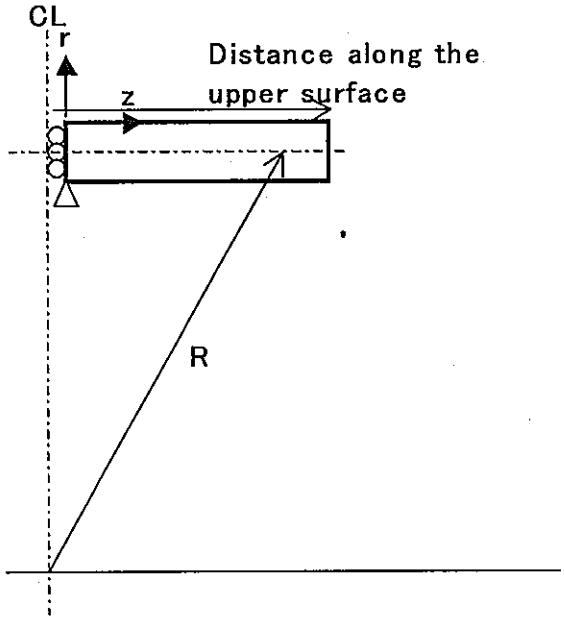

Fig. 4.9 Coordinate system for output

(1) Case T-ML series

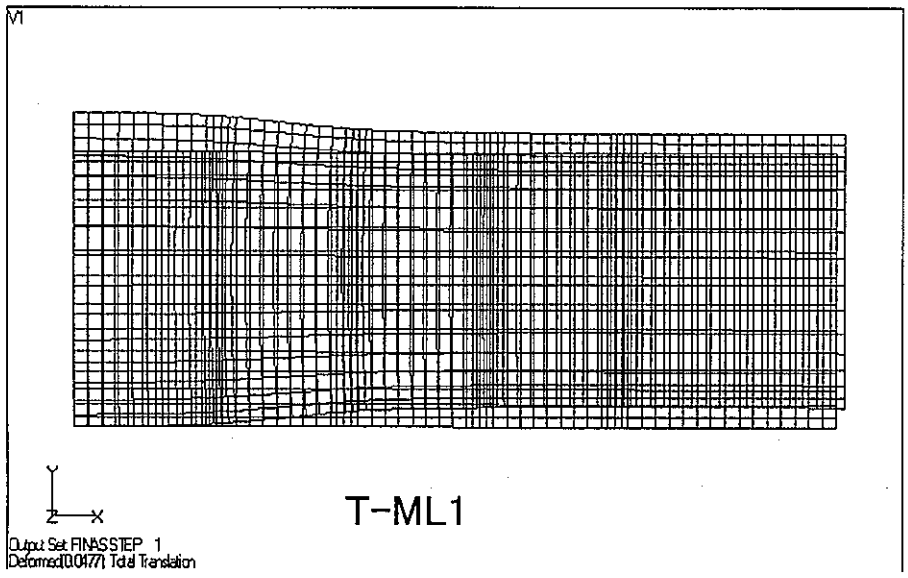

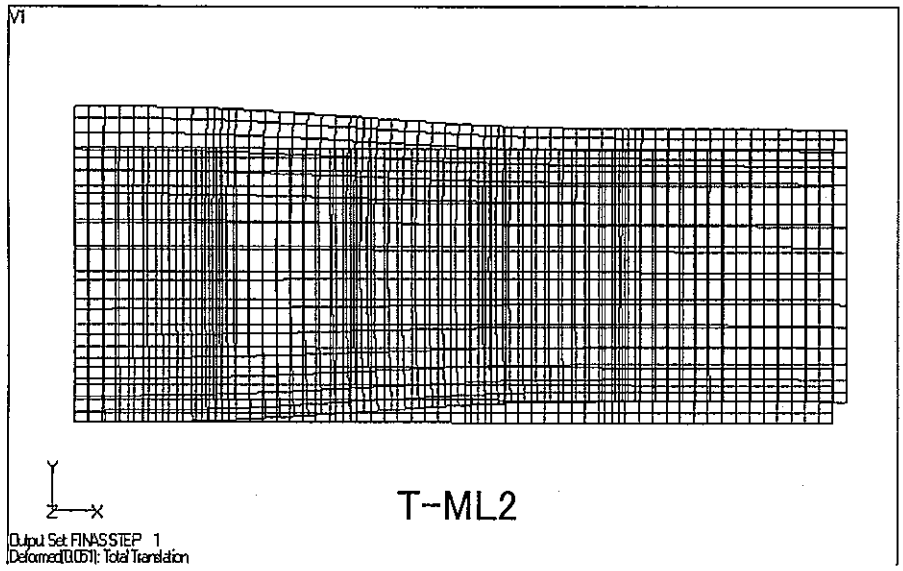

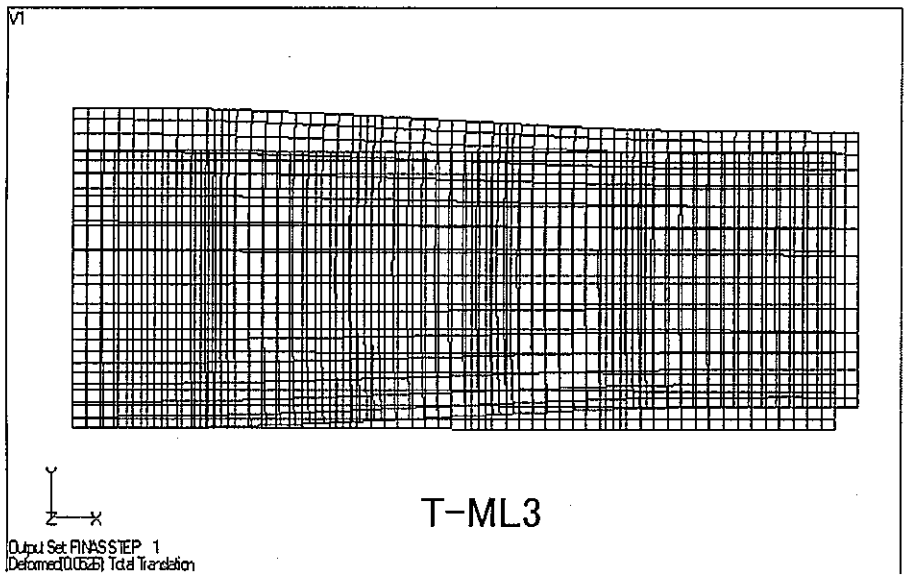

Fig. 4.10 Deformed shape (T-ML)

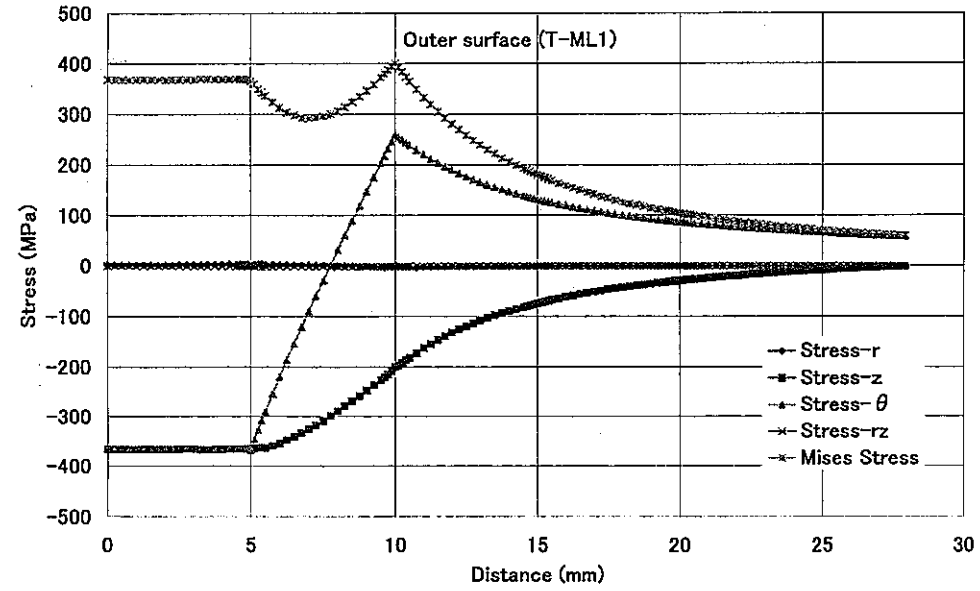

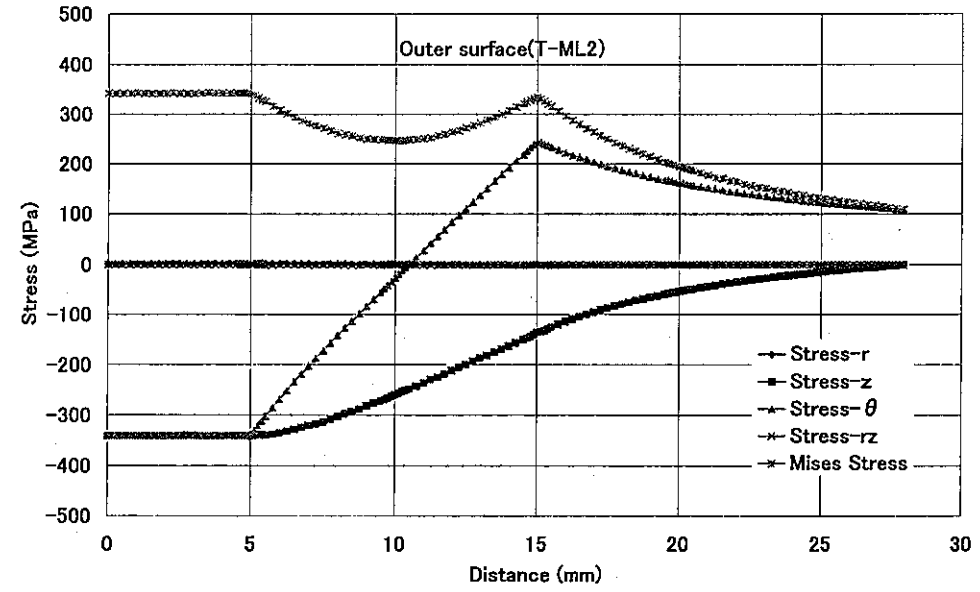

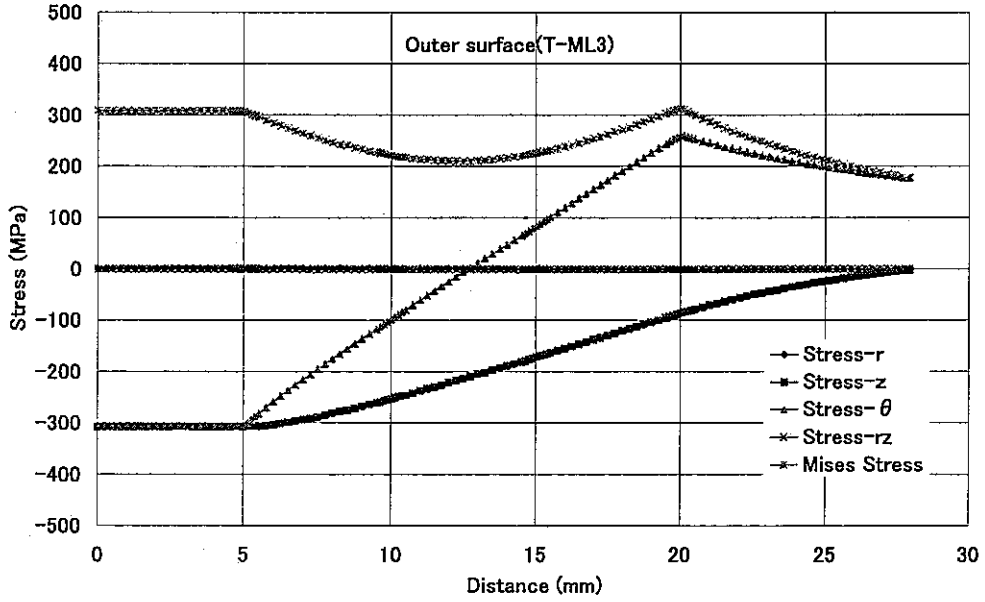

Fig. 4.11 Stress distribution on the upper surface (T-ML)

(2) Case T-BL series

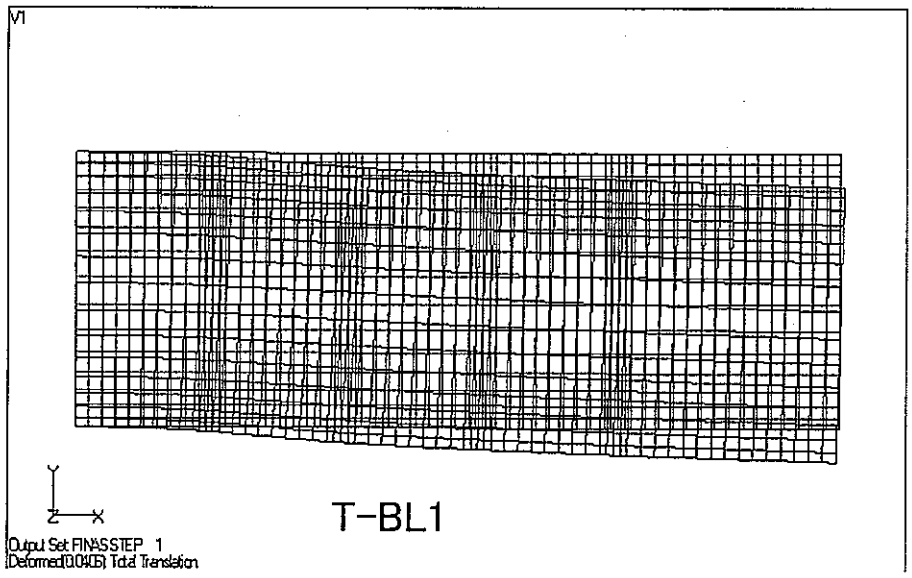

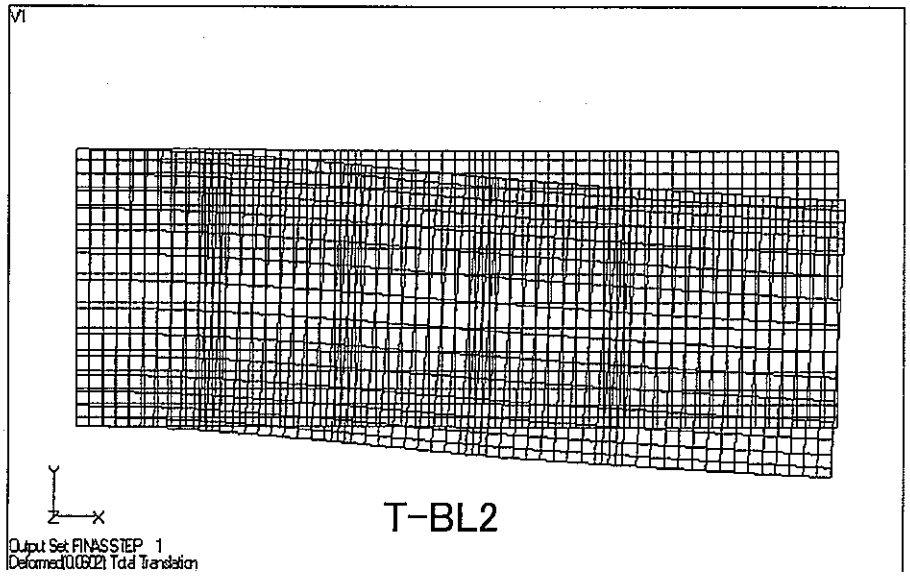

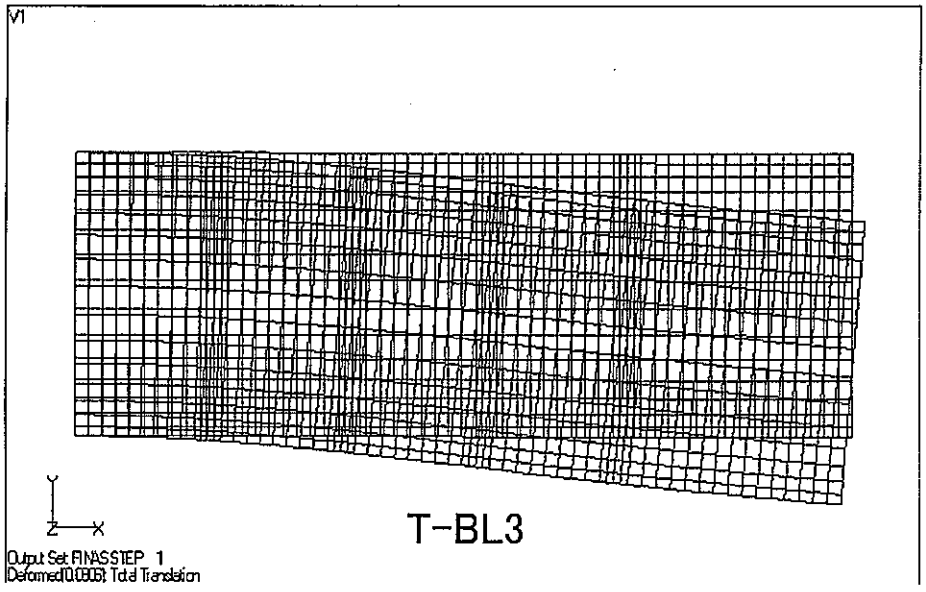

Fig. 4.12 Deformed shape (T-BL)

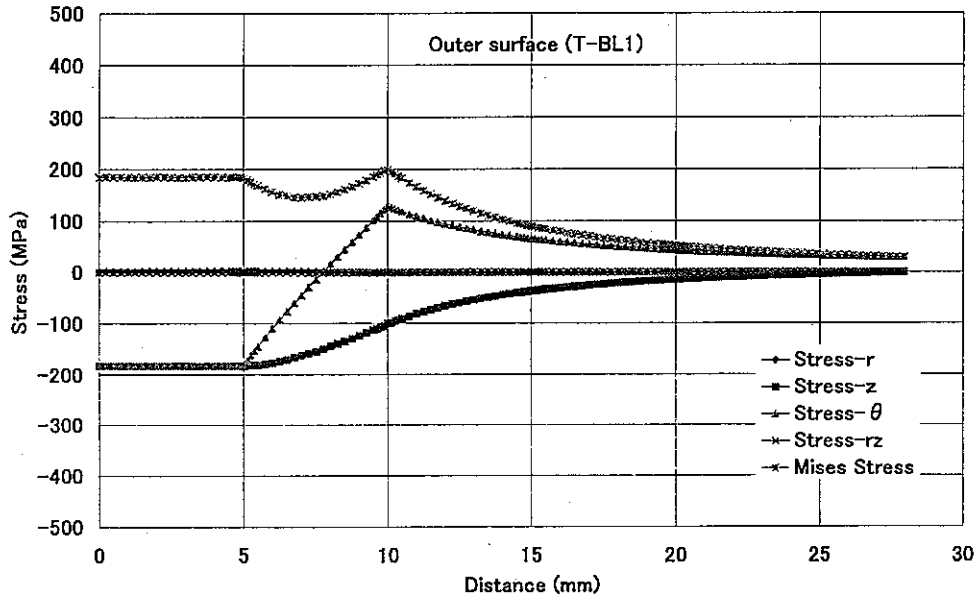

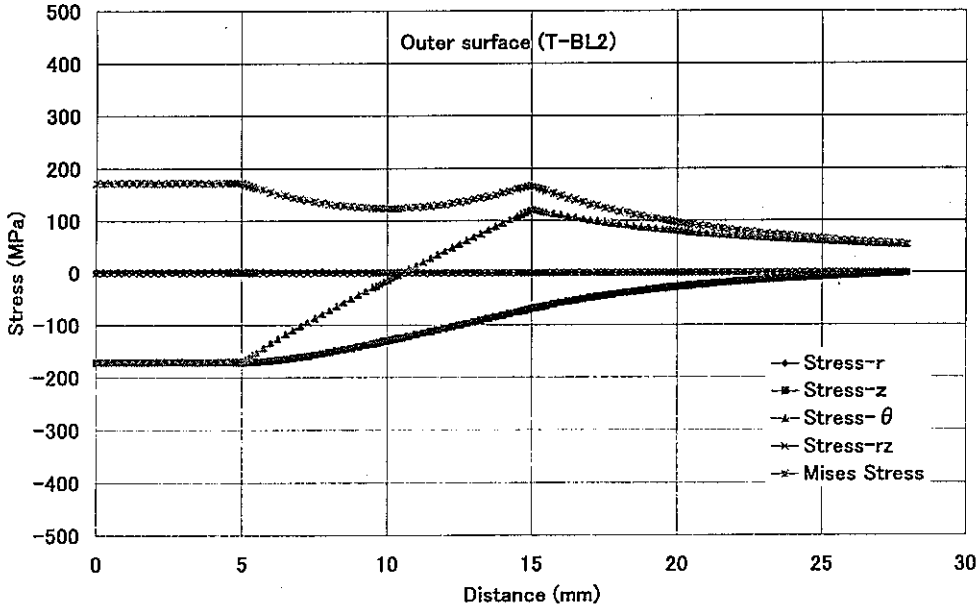

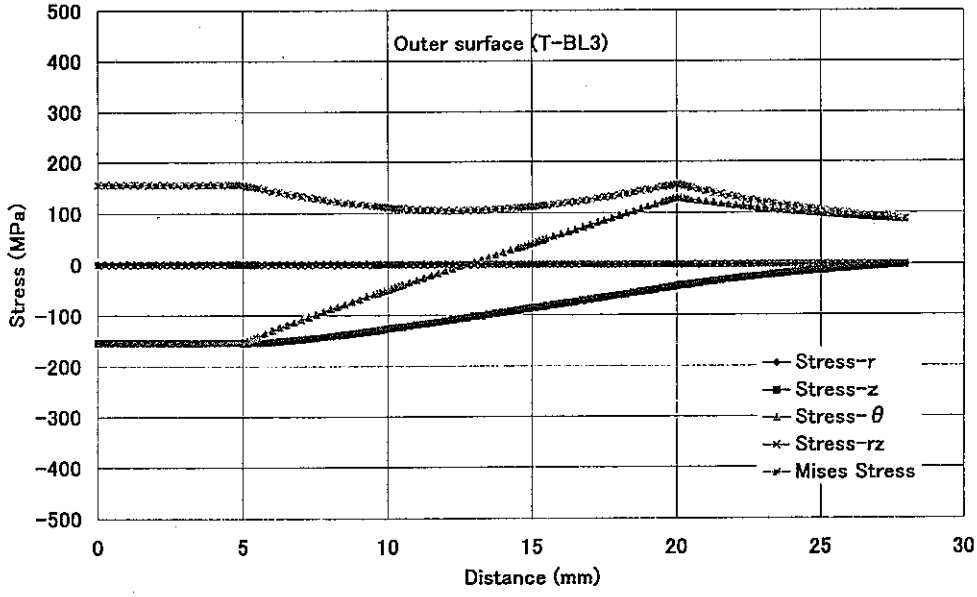

Fig. 4.13 Stress distribution on the upper surface (T-BL)

From above F.E. calculated results, we can get constraint efficiency factors for membrane and bending stresses.

Factors for membrane stresses are

$$A_m = \frac{|\sigma_C|}{\Delta\sigma^*} \quad \text{(Center of spot),} \tag{4.1}$$

$$A_m = \frac{|\sigma_i|}{\Delta\sigma^*} \quad \text{(Boundary of spot) and} \tag{4.2}$$

$$A_m = \frac{\max(|\sigma_c - \sigma_o|, |\sigma_i - \sigma_o|)}{\Delta\sigma^*} \quad \text{(Moving spot).} \tag{4.3}$$

Factors for bending stresses are

$$A_b = \frac{|\sigma_C|}{\Delta\sigma^*/2} \quad \text{(Center of spot),} \tag{4.4}$$

$$A_b = \frac{|\sigma_i|}{\Delta\sigma^*/2} \quad \text{(Boundary of spot) and} \tag{4.5}$$

$$A_b = \frac{\max(|\sigma_c - \sigma_o|, |\sigma_i - \sigma_o|)}{\Delta\sigma^*/2} \quad \text{(Moving spot).} \tag{4.6}$$

The next table shows evaluated constraint efficiency factors.

Table 4.4 Constraint efficiency factors by F.E. calculation

Case	F.E.Calculated Mises Stress (MPa)			$\Delta\sigma^*$(MPa)=	Ratio A_m		
	Center of hot spot σc	Bounday inside hot spot σi	Bounday outside hot spot σo	$E\alpha/(1-\nu)\cdot\Delta T_f$	$\lvert\sigma_c\rvert/\Delta\sigma^*$	$\lvert\sigma_i\rvert/\Delta\sigma^*$	$\max(\lvert\sigma_c-\sigma_o\rvert,\lvert\sigma_i-\sigma_o\rvert)/\Delta\sigma^*$
T-ML1	-366.1	-364.8	254.70	1120.4	0.327	0.326	0.55
T-ML2	-350.0	-340.2	242.50	1120.4	0.312	0.304	0.53
T-ML3	-307.5	-307.0	259.40	1120.4	0.274	0.274	0.51

Case	F.E.Calculated Mises Stress (MPa)			$\Delta\sigma^*$(MPa)=	Ratio A_b		
	Center of hot spot σc	Bounday inside hot spot σi	Bounday outside hot spot σo	$E\alpha/(1-\nu)\cdot\Delta T_f$	$\lvert\sigma_c\rvert/(\Delta\sigma^*/2)$	$\lvert\sigma_i\rvert/(\Delta\sigma^*/2)$	$\max(\lvert\sigma_c-\sigma_o\rvert,\lvert\sigma_i-\sigma_o\rvert)/(\Delta\sigma^*/2)$
T-BL1	-183.0	-182.4	127.00	1120.4	0.327	0.326	0.55
T-BL2	-170.4	-170.1	120.90	1120.4	0.304	0.304	0.52
T-BL3	-153.7	-150.2	129.20	1120.4	0.274	0.268	0.50

4.3 EVALUATION WITH THE FREQUENCY RESPONSE FUNCTION

When inputting factors of Table 4.4 and Biot number Bi=8.19 that corresponds to 13300kcal/m^{2}h℃ into Eq.(2.9), we can get stress response diagrams as in the next figure.

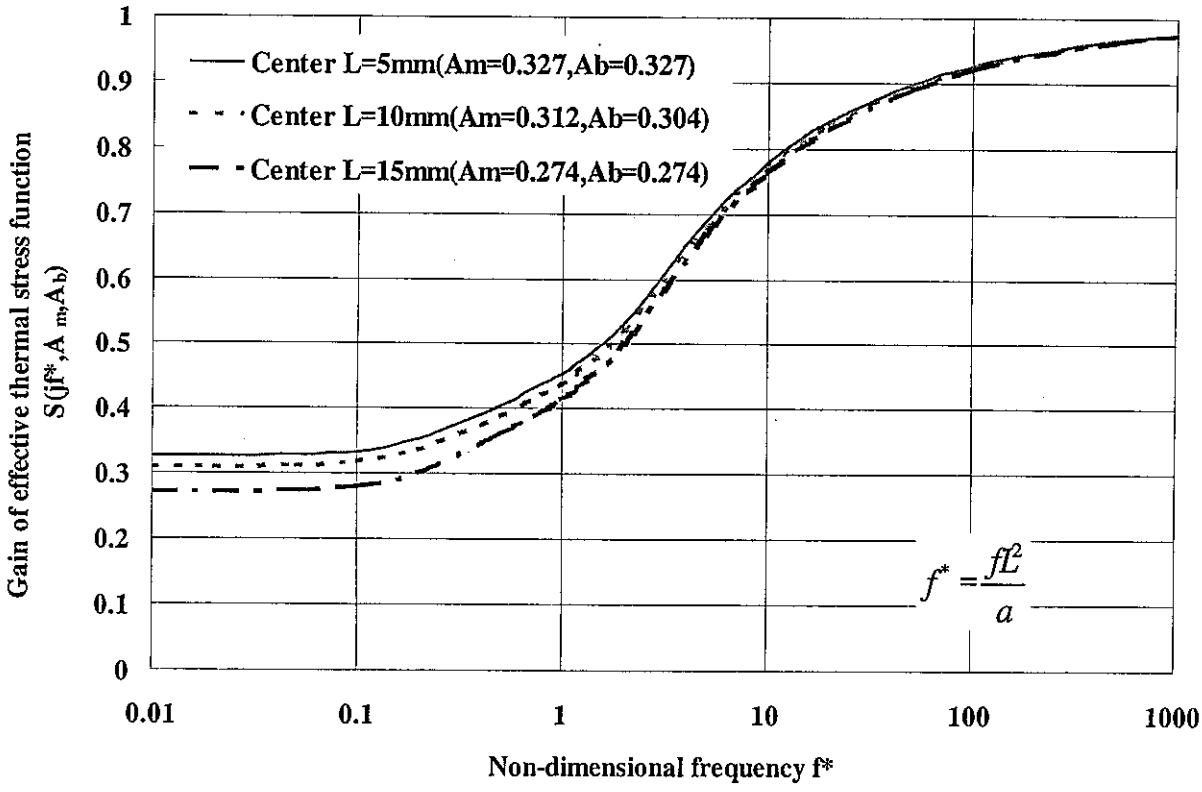

Fig. 4.14 Effective thermal stress diagrams with F.E. calculated gains

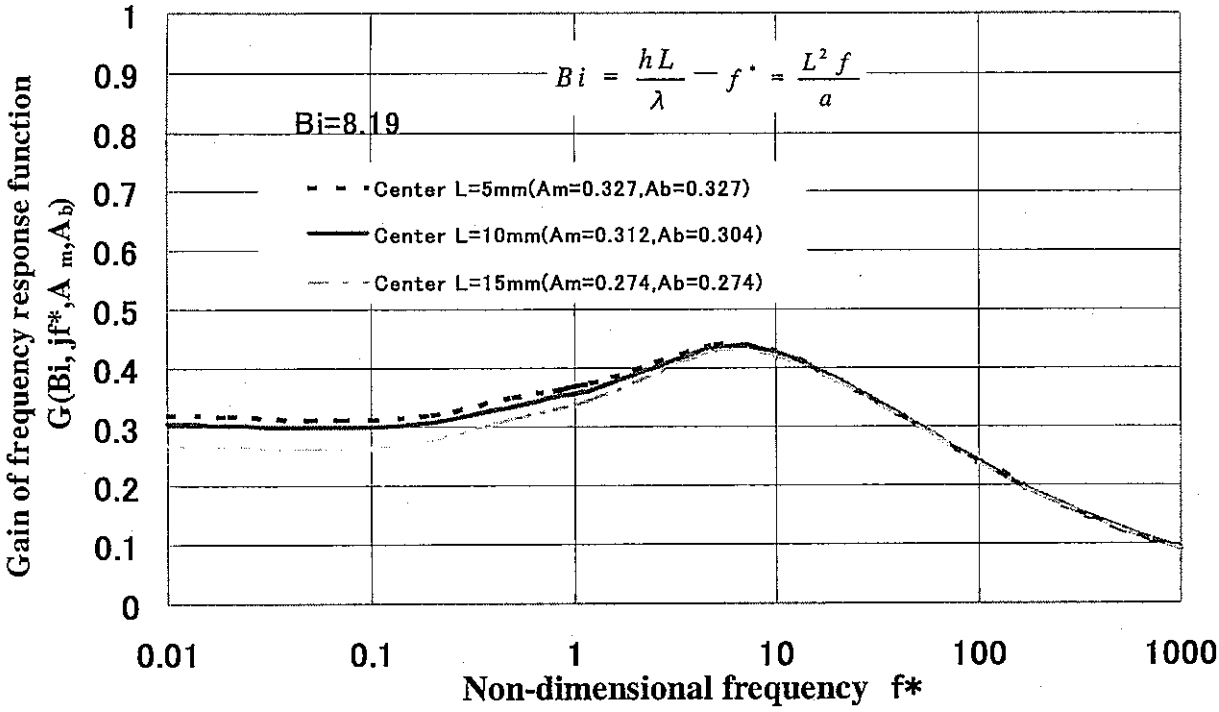

Fig. 4.15 Frequency response diagrams with F.E. calculated gains

5. DIAGRAMS OF CONSTRAINT EFFICIENCY FACTORS

5.1 PARAMETERS OF CONSTRAINT EFFICIENCY FACTORS

In the case of straight pipes, geometrical parameters to determine constraint conditions are R/t of Fig.5.1. Furthermore, constraints of spots depend on their sizes that can be characterized by $\theta/2$ of Fig.5.1. So that, constraint efficiency factors A_m and A_b have been investigated under various values of R/t and $\theta/2$ as in Table 5.1. In the symmetric analysis model shown in Fig.5.1, interactions between two spots are ignored, validation of which will be required.

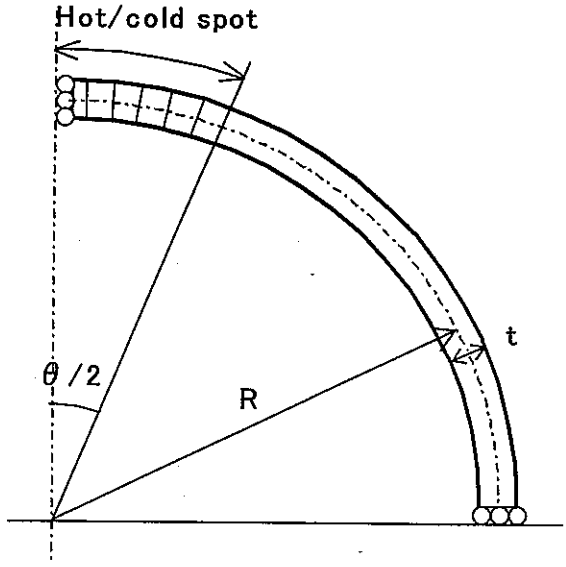

Fig. 5.1 Geometrical parameters to determine constraint conditions

Table 5.1(a) Geometrical parameters and load conditions (a)

Case	R(mm)	t(mm)	$\theta/2$ (deg)	R/t	Load	Remark
ML-t1	250.5	50.1	24.2	5	Fig.5.2	
ML-t2	250.5	21	24.2	11.9	Fig.5.2	PWR
ML-t3	250.5	7	24.2	35.8	Fig.5.2	Phenix
ML-t4	250.5	2.505	24.2	100	Fig.5.2	
ML-t5	250.5	0.2505	24.2	1000	Fig.5.2	TIFFSS4

Table 5.1(b) Geometrical parameters and load conditions (b)

Case	R(mm)	t(mm)	$\theta/2$ (deg)	R/t	Load	Remark
ML-θ1	250.5	7	2.5	35.8	Fig.5.2	
ML-θ2	250.5	7	5	35.8	Fig.5.2	
ML-θ3	250.5	7	10	35.8	Fig.5.2	
ML-θ4	250.5	7	24.2	35.8	Fig.5.2	Phenix
ML-θ5	250.5	7	45	35.8	Fig.5.2	

Table 5.1(c) Geometrical parameters and load conditions (c)

Case	R(mm)	t(mm)	θ /2 (deg)	R/t	Load	Remark
BL-t1	250.5	50.1	24.2	5	Fig.5.3	
BL-t2	250.5	21	24.2	11.9	Fig.5.3	PWR
BL-t3	250.5	7	24.2	35.8	Fig.5.3	Phenix
BL-t4	250.5	2.505	24.2	100	Fig.5.3	
BL-t5	250.5	0.2505	24.2	1000	Fig.5.3	TIFFSS4

Table 5.1(d) Geometrical parameters and load conditions (d)

Case	R(mm)	t(mm)	θ /2 (deg)	R/t	Load	Remark
BL-θ1	250.5	7	2.5	35.8	Fig.5.3	
BL-θ2	250.5	7	5	35.8	Fig.5.3	
BL-θ3	250.5	7	10	35.8	Fig.5.3	
BL-θ4	250.5	7	24.2	35.8	Fig.5.3	Phenix
BL-θ5	250.5	7	45	35.8	Fig.5.3	

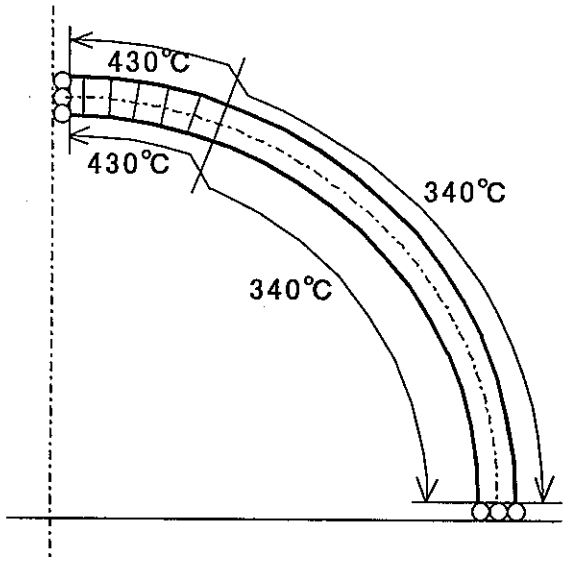

Fig. 5.2 Boundary condition of membrane stress (Case ML series)

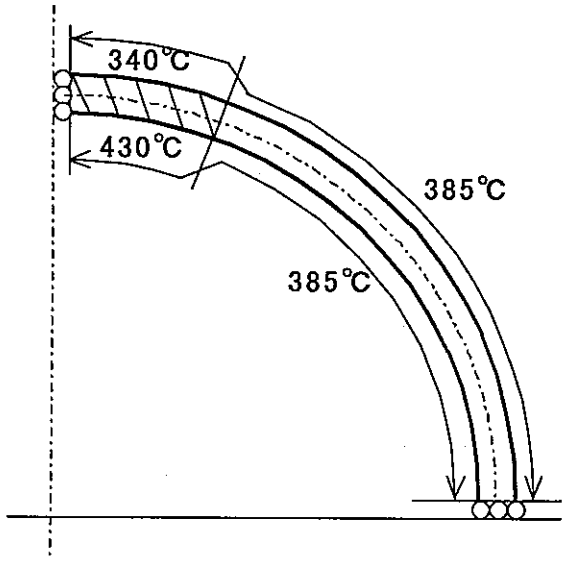

Fig. 5.3 Boundary condition of bending stress (Case BL series)

5.2. SHELL ANALYSIS RESULTS

To make diagrams of constraint efficiency diagrams, shell analyses have been conducted with mesh models shown in Fig.5.4.

Conical shell element CONIC2 of the FINAS code [6] was utilized for this calculation. Since temperature dependency of material has few effects [2][3], material properties were assumed as constant values at 385℃. In order to avoid numerical singularity at the hot spot boundary, temperature changes smoothly at the boundary within short distances.

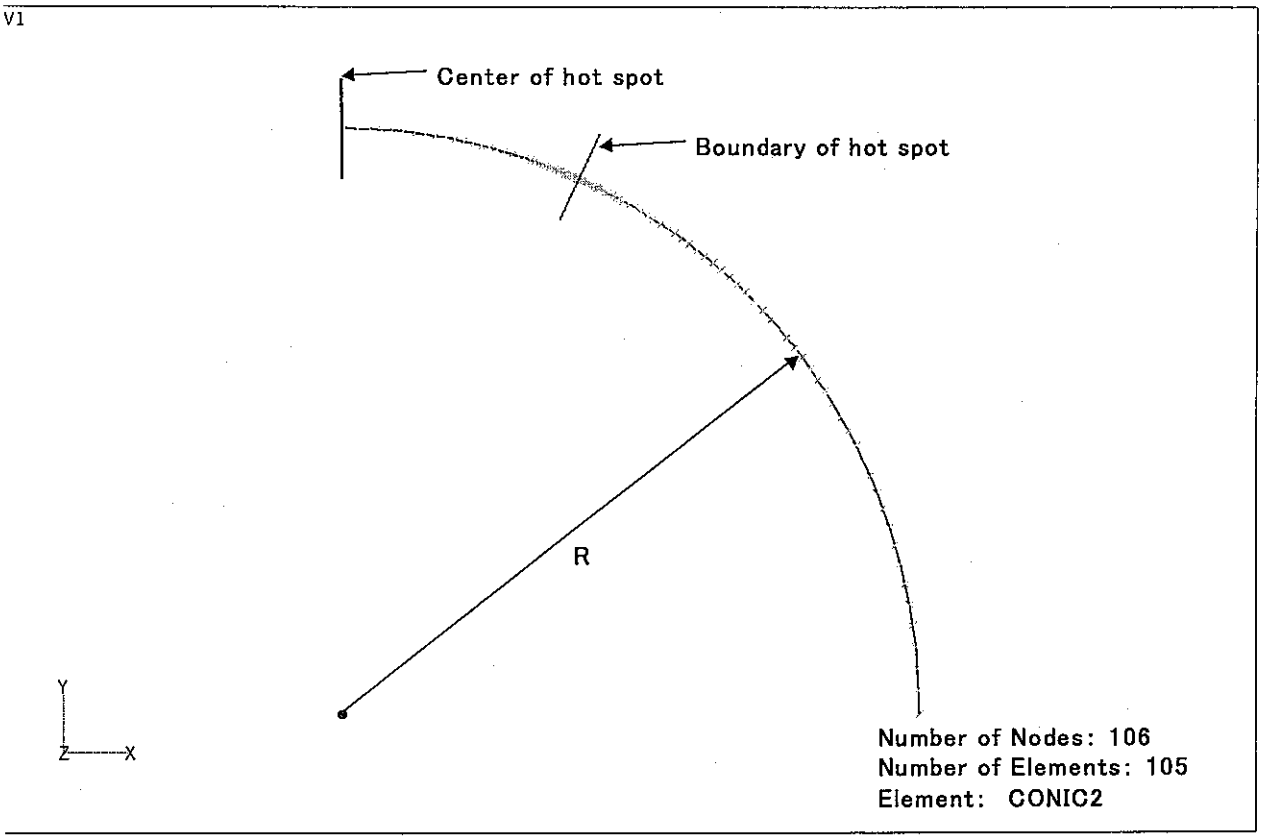

Fig. 5.4 Shell analysis model

(1) Case ML-t series

Calculated deformations of case ML-t series (Fig.5.5) show that structures with large R/t deform well due to their large flexibility. Stress distributions (Fig.5.6) indicate that flexible structures induce small stresses.

Furthermore, shell analysis was validated to provide the same results as solid analysis since stress distribution of ML-t3 is quite similar to one of P-ML (Fig.3.11(b)).

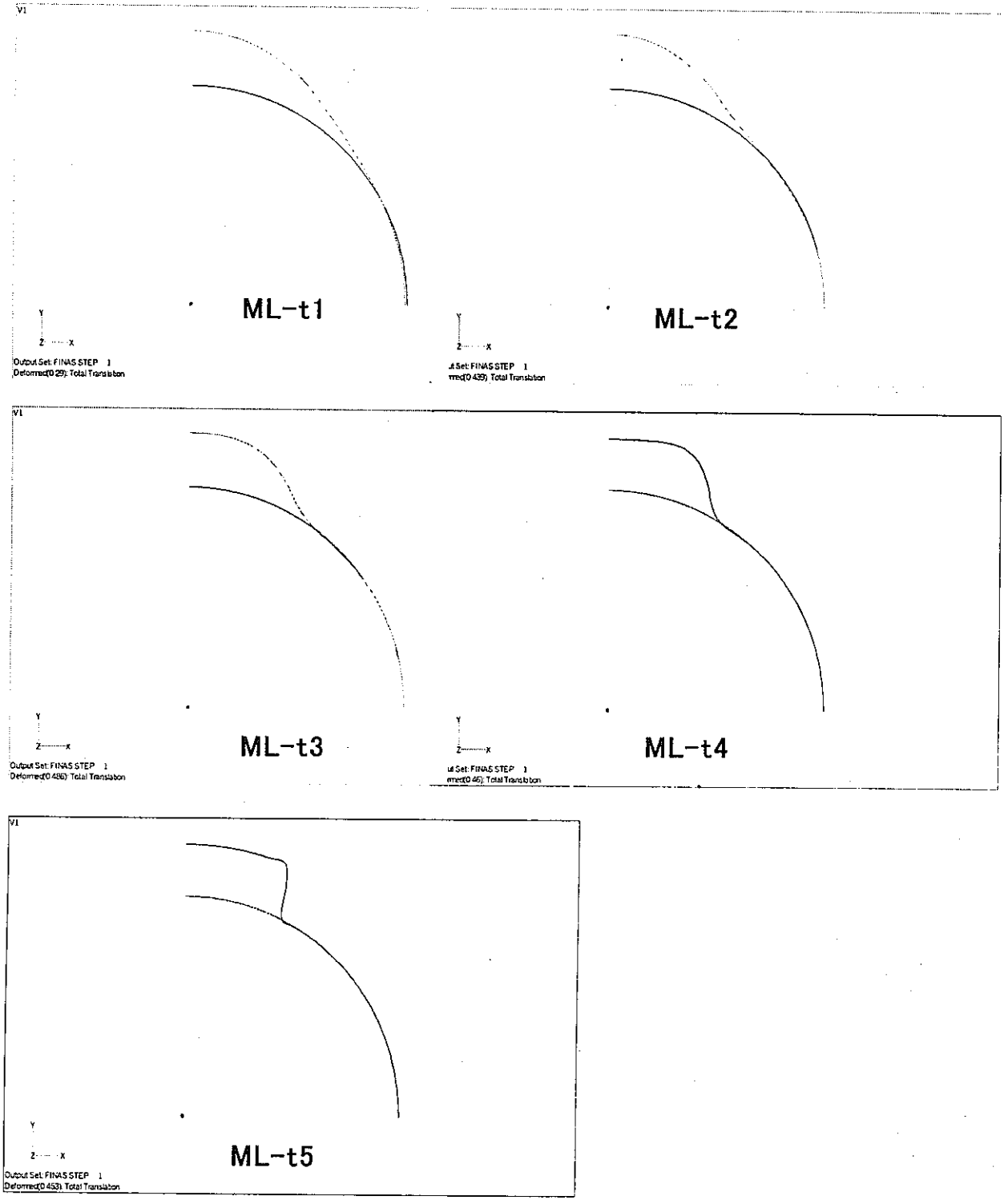

Fig. 5.5 Calculated deformations (ML-t series)

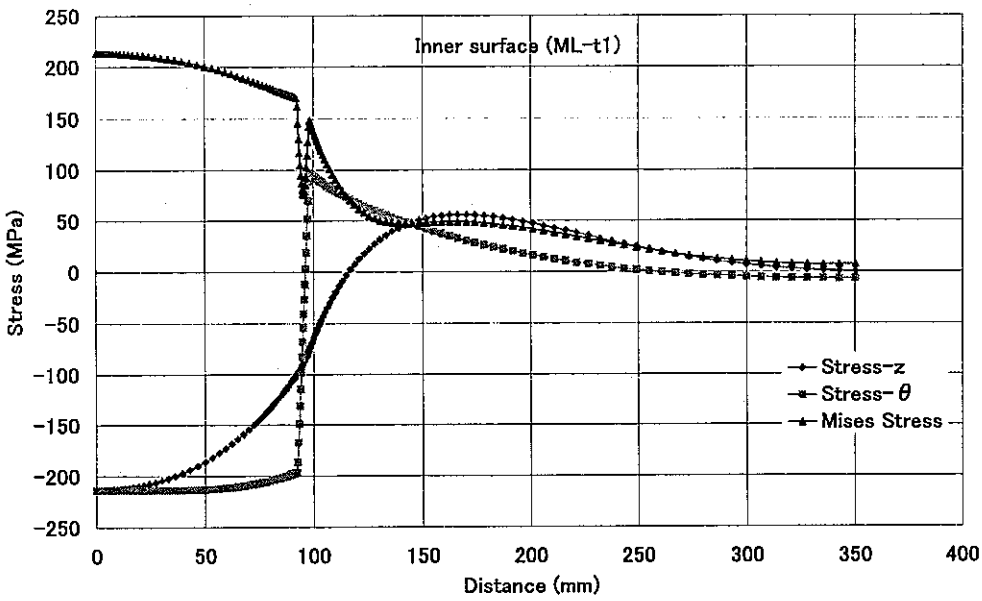
Inner surface (ML-t1)
Stress (MPa)
Distance (mm)
Stress-z
Stress-θ
Mises Stress

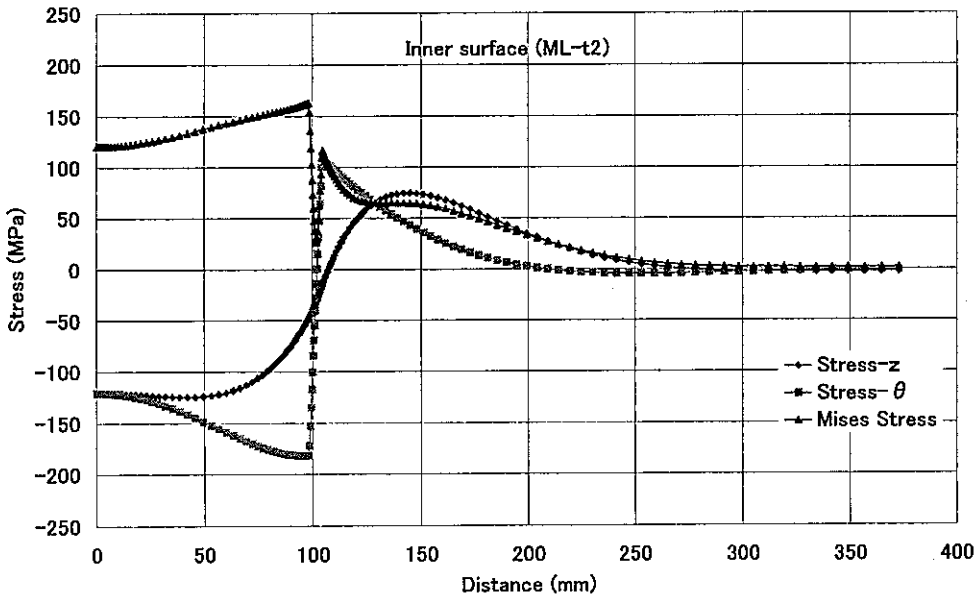
Inner surface (ML-t2)
Stress (MPa)
Distance (mm)
Stress-z
Stress-θ
Mises Stress

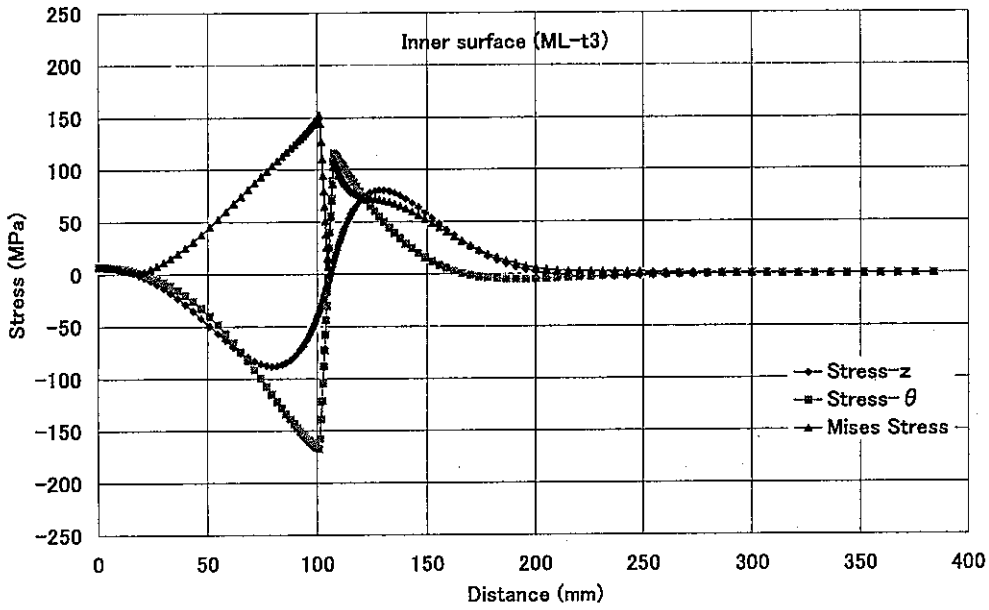
Inner surface (ML-t3)
Stress (MPa)
Distance (mm)
Stress-z
Stress-θ
Mises Stress

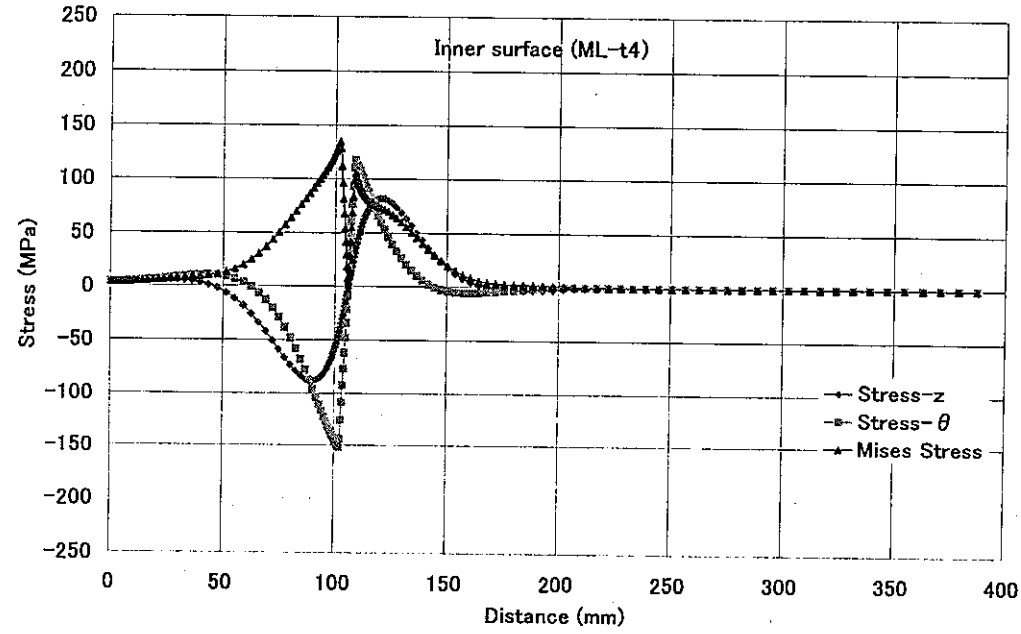

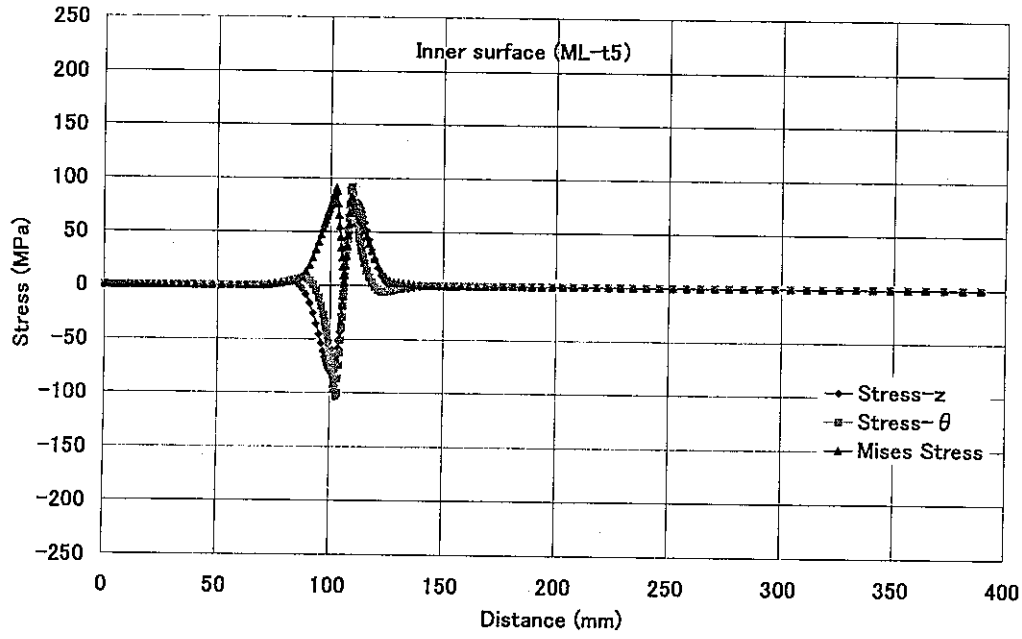

Fig. 5.6 Stress distribution on the inner surface (ML-t series)

(2) Case ML-θ series

The following results of case ML-θ series show that structures with large θ deform well and induce small stresses.

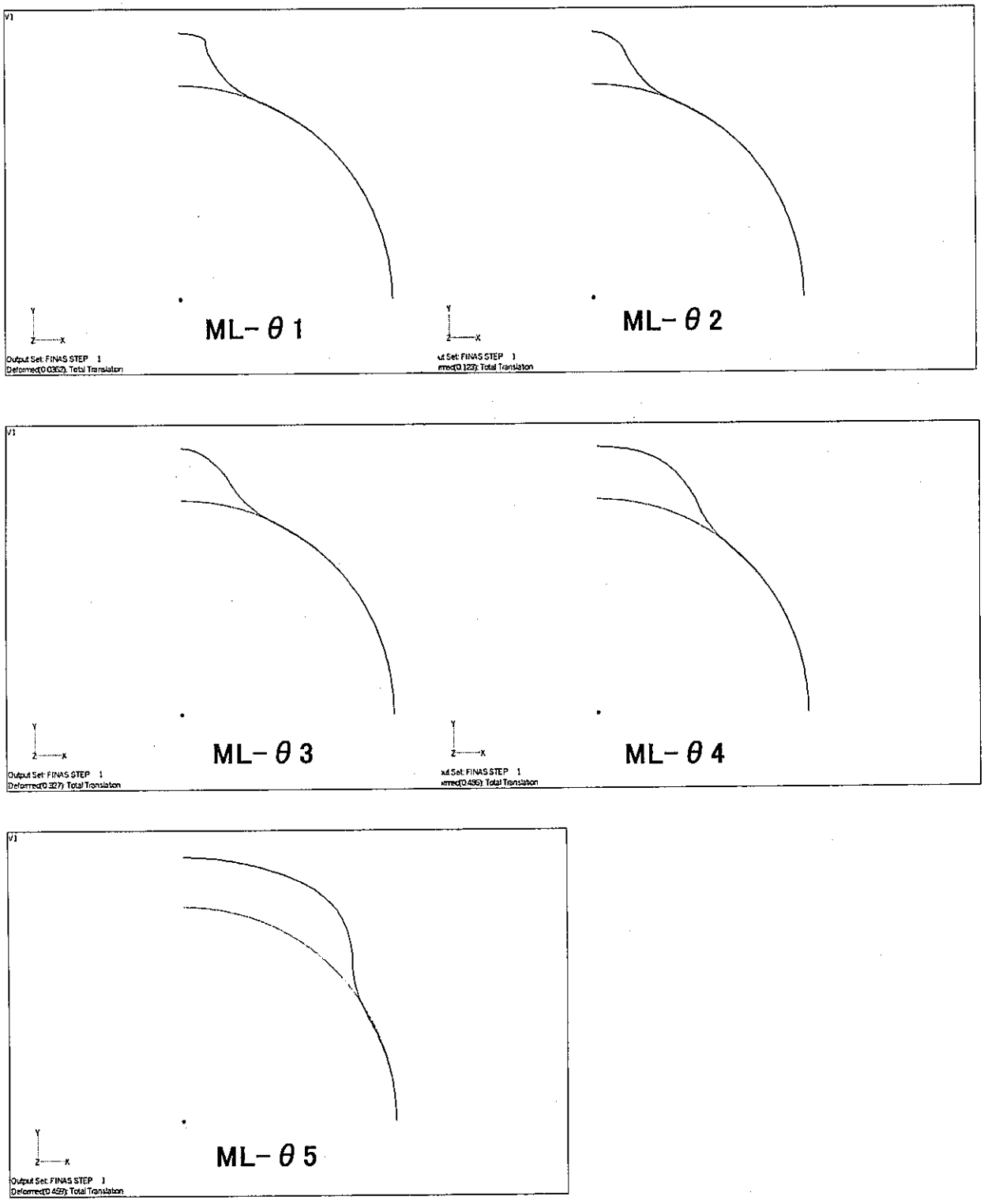

Fig. 5.7 Calculated deformation (ML-θ series)

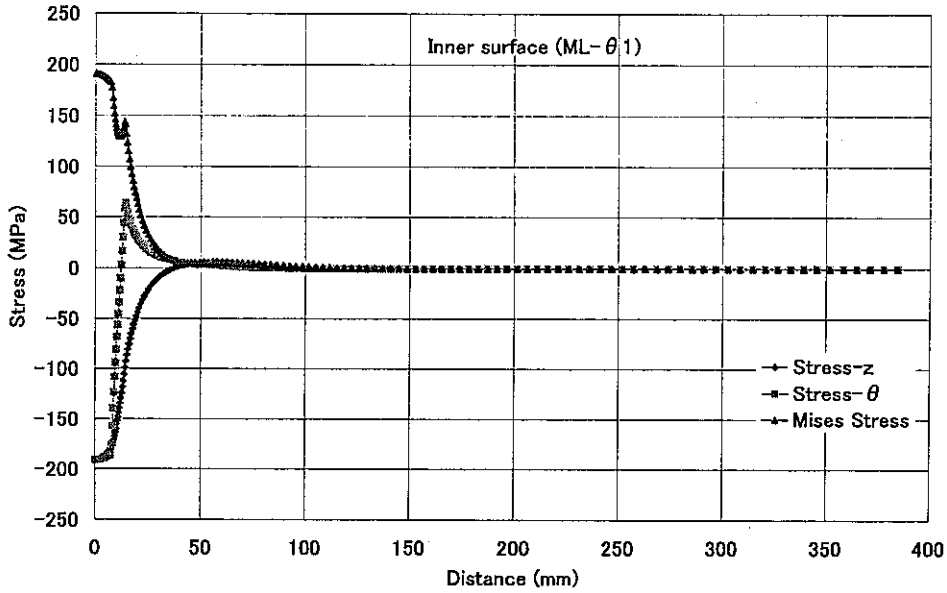
Inner surface (ML-θ1)
Stress (MPa)
Distance (mm)
Stress-z
Stress-θ
Mises Stress

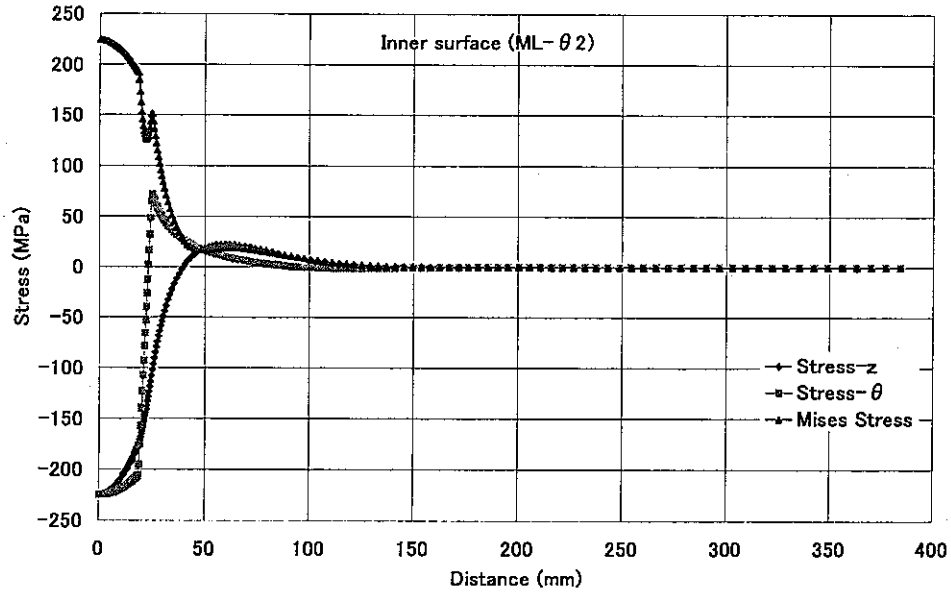
Inner surface (ML-θ2)
Stress (MPa)
Distance (mm)
Stress-z
Stress-θ
Mises Stress

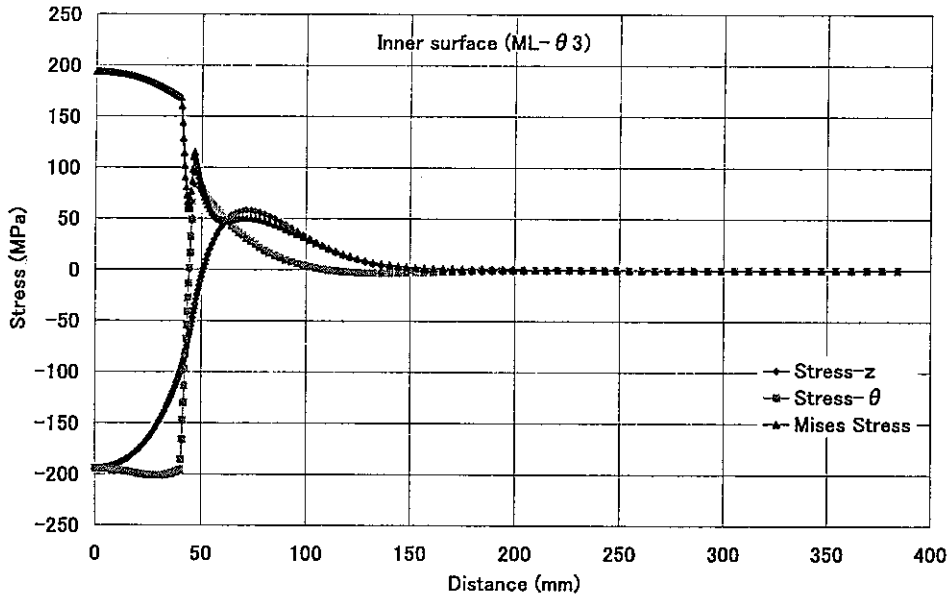
Inner surface (ML-θ3)
Stress (MPa)
Distance (mm)
Stress-z
Stress-θ
Mises Stress

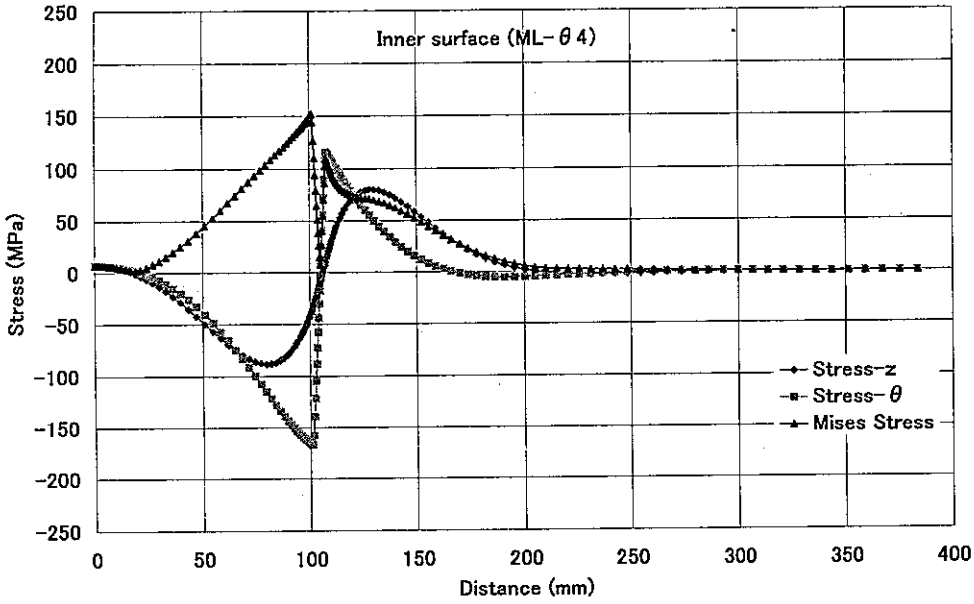

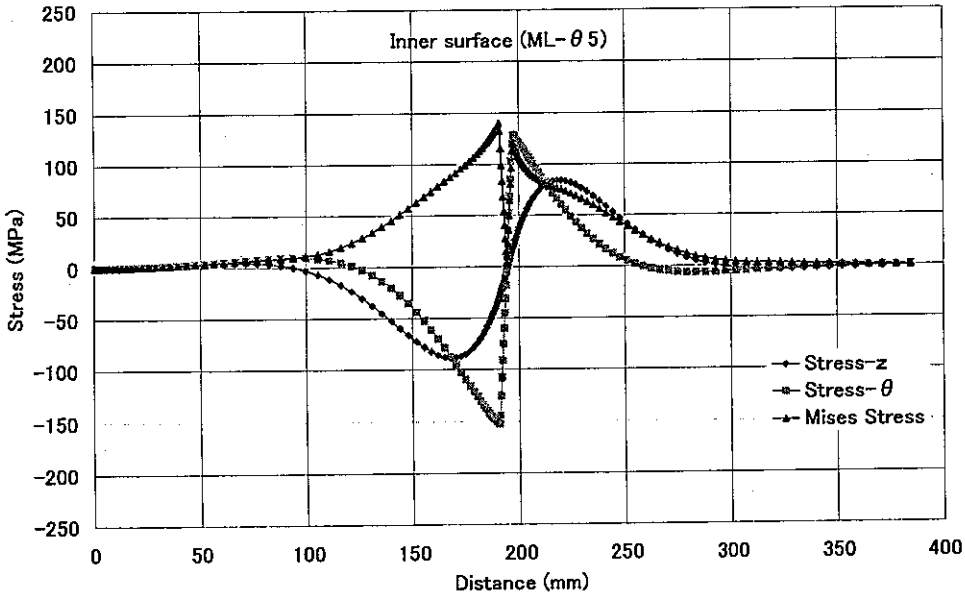

Fig. 5.8 Stress distribution on the inner surface (ML-θ series)

(3) Case BL-t series

The following results of case ML-t series show that structures with large R/t deform well since large flexibility and induced stresses are insensitive to R/t.

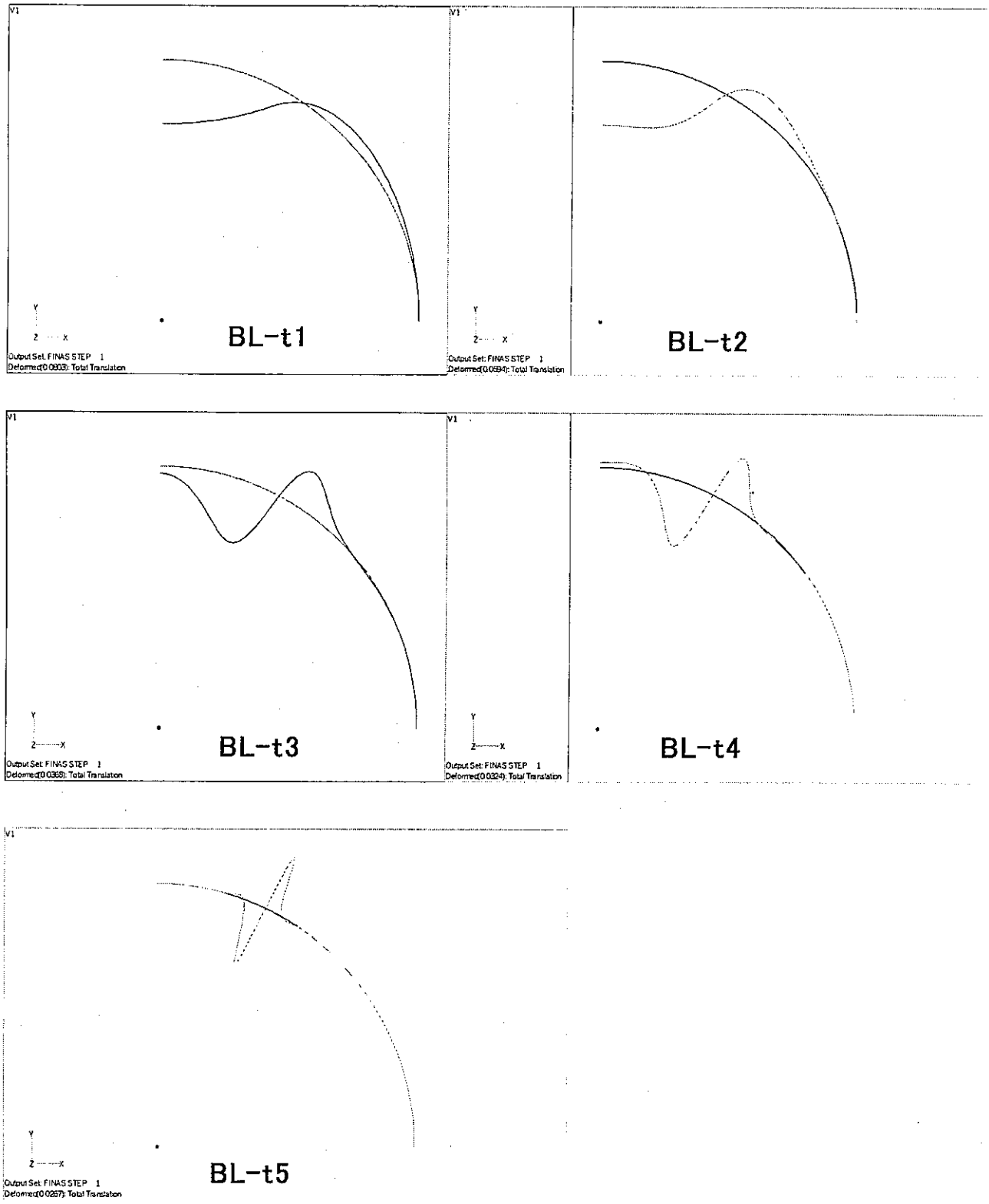

Fig. 5.9 Calculated deformation (BL-t series)

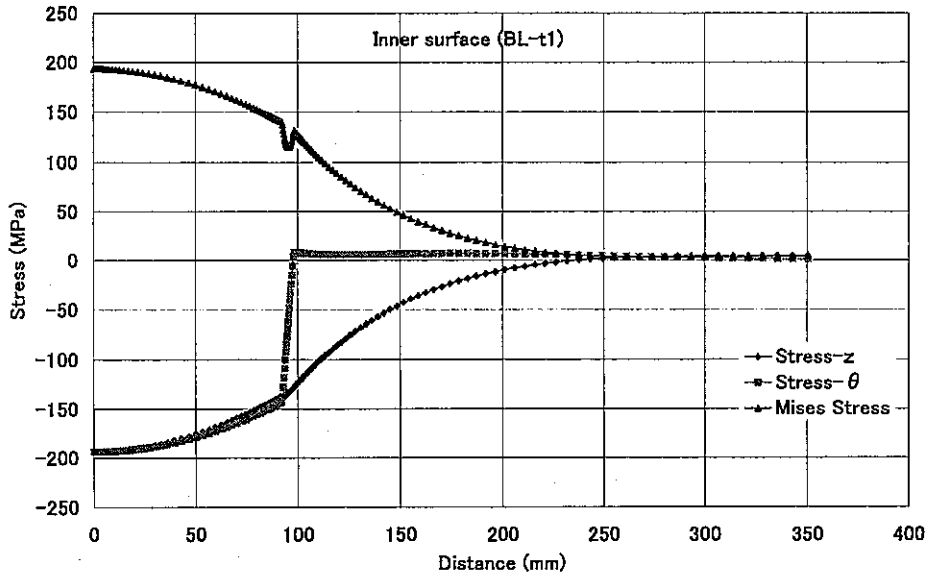
Inner surface (BL-t1)
Stress (MPa)
Distance (mm)
Stress-z
Stress-θ
Mises Stress

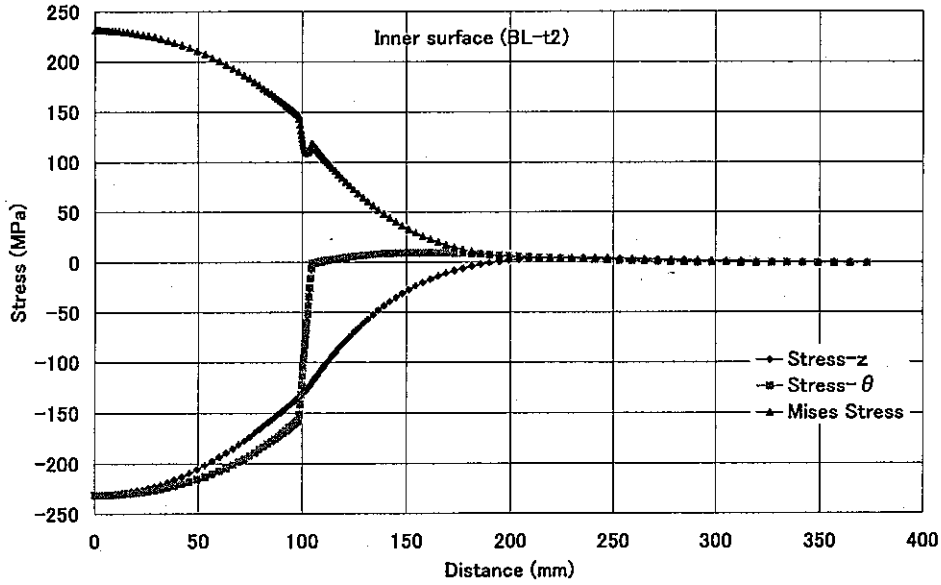
Inner surface (BL-t2)
Stress (MPa)
Distance (mm)
Stress-z
Stress-θ
Mises Stress

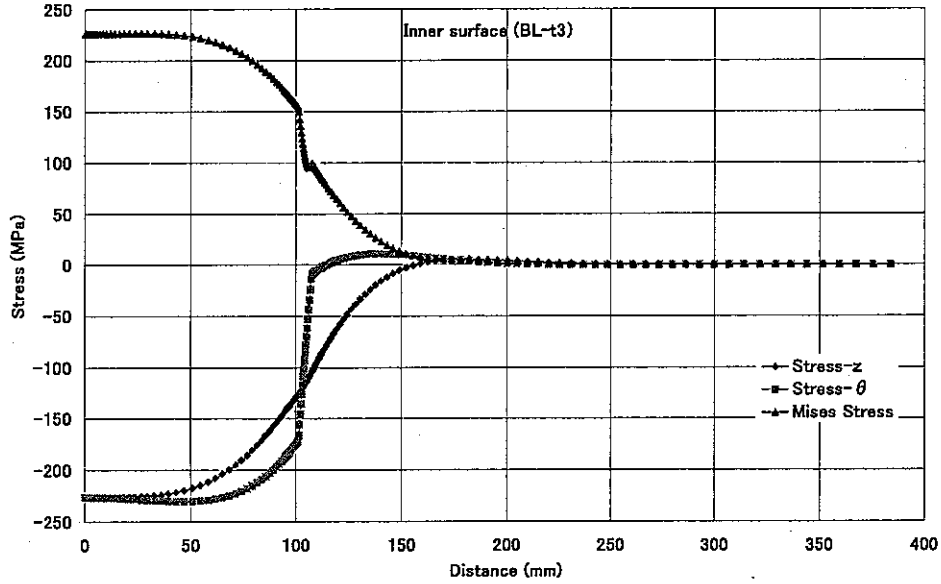
Inner surface (BL-t3)
Stress (MPa)
Distance (mm)
Stress-z
Stress-θ
Mises Stress

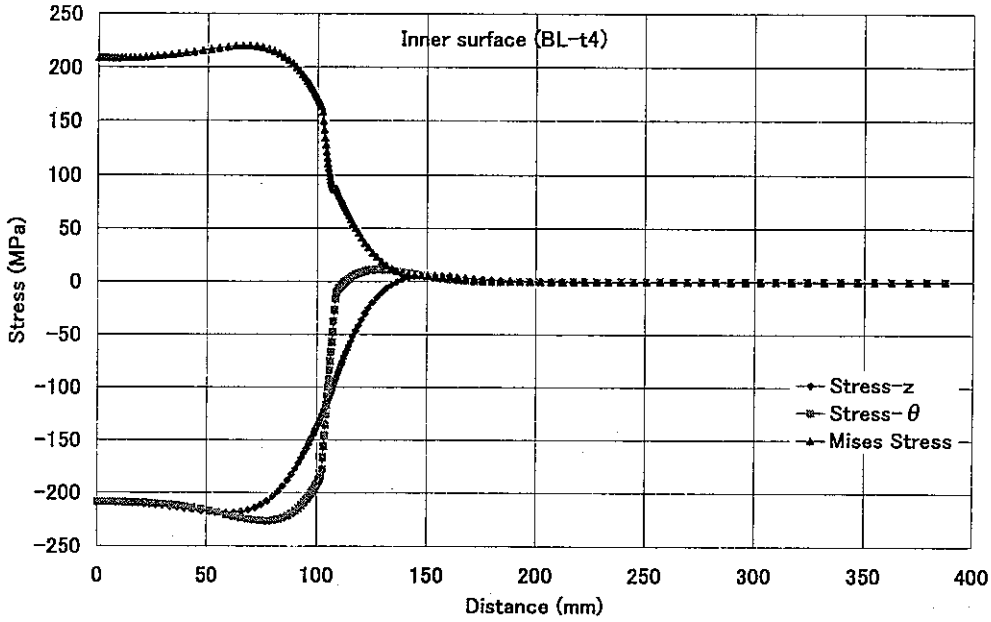

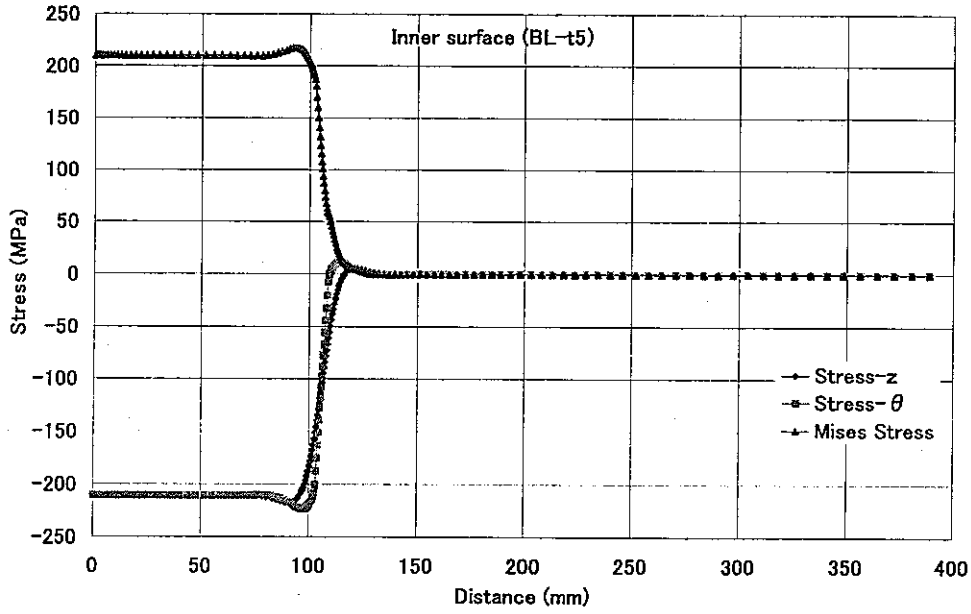

Fig. 5.10 Stress distribution on the inner surface (BL-t series)

(4) Case BL-θ series

The following results of case BL-θ series show that structures with large θ deform well and induced stresses are insensitive to θ except small θ.

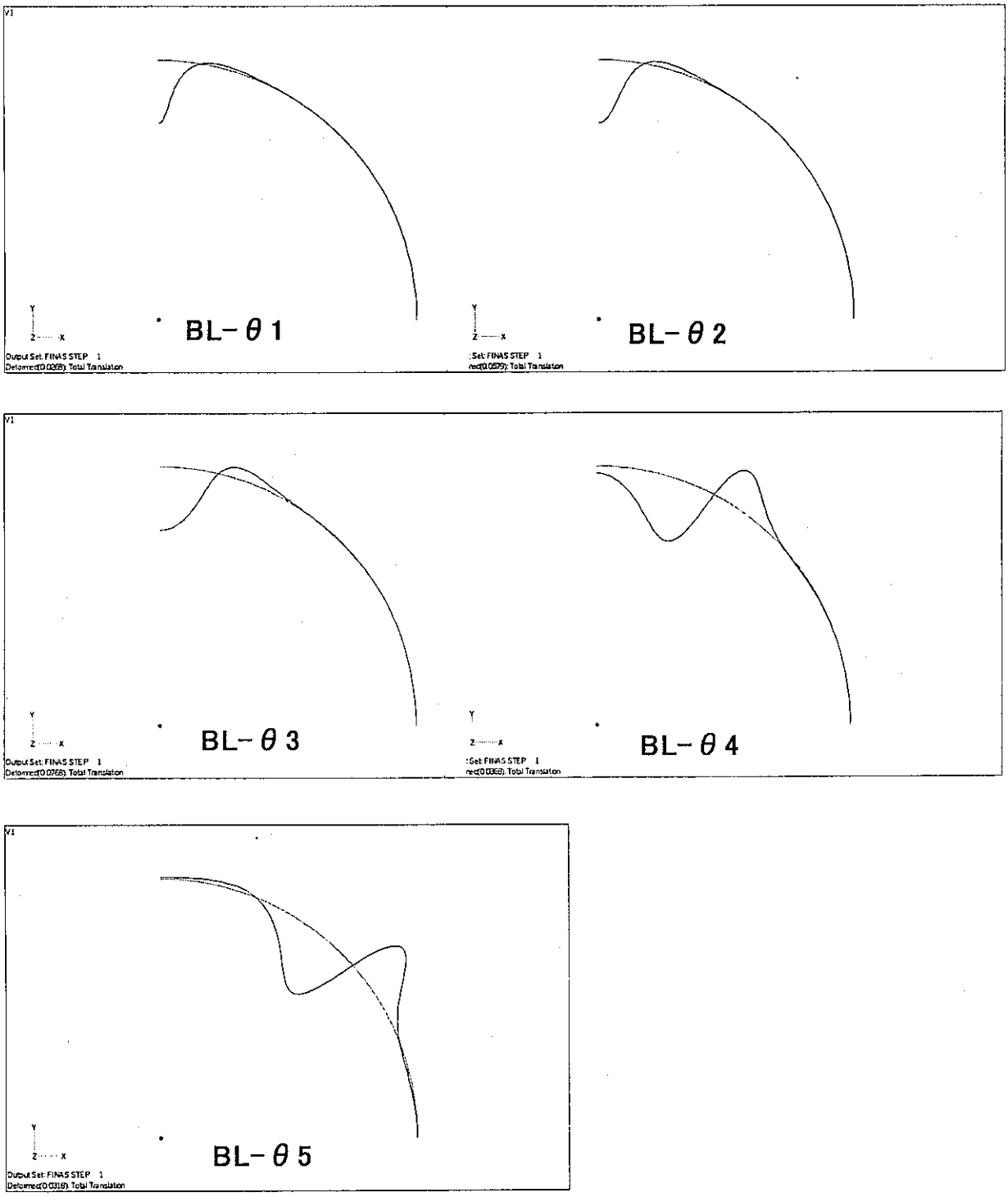

Fig. 5.11 Calculated deformation (BL-θ series)

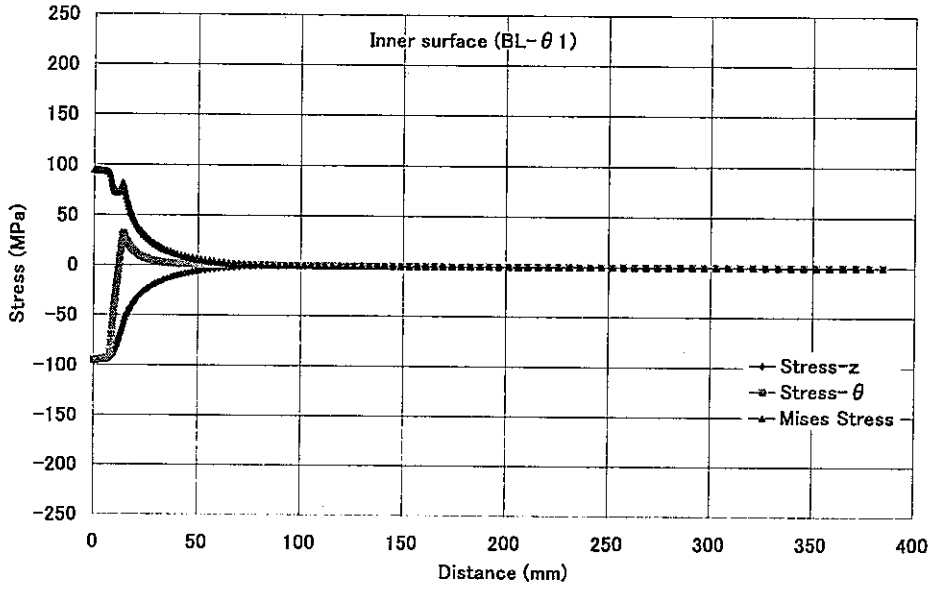
Inner surface (BL-θ1)
Stress (MPa)
Distance (mm)
Stress-z
Stress-θ
Mises Stress

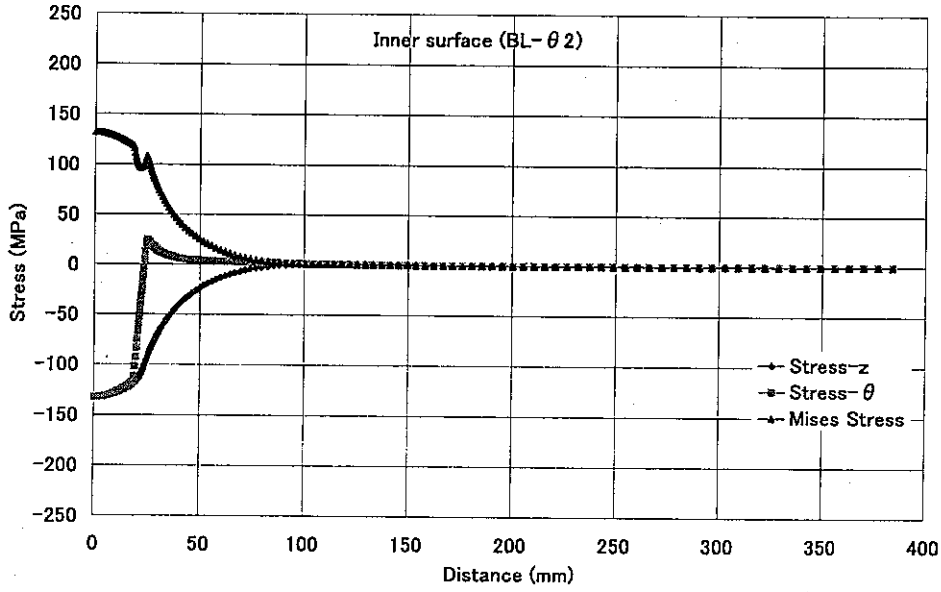
Inner surface (BL-θ2)
Stress (MPa)
Distance (mm)
Stress-z
Stress-θ
Mises Stress

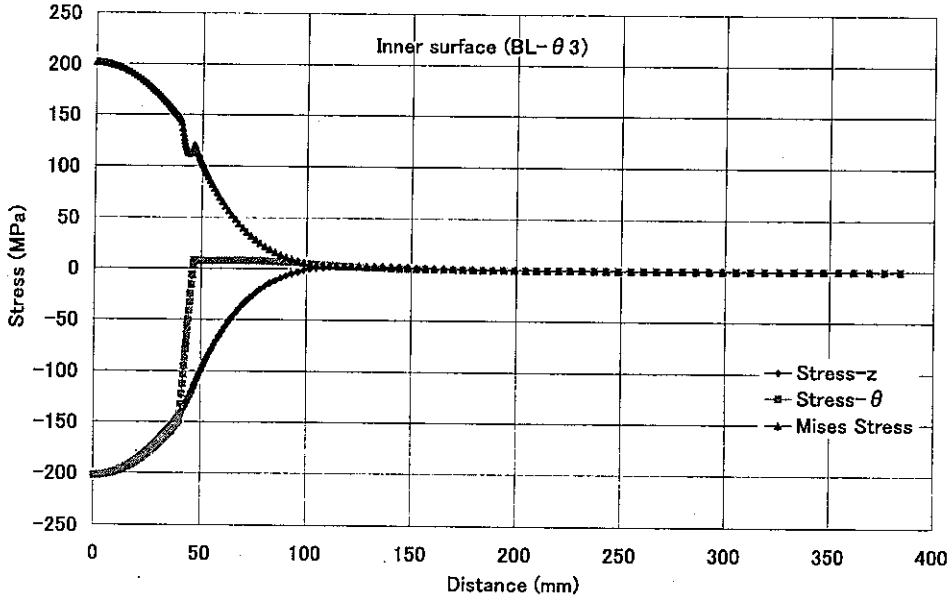
Inner surface (BL-θ3)
Stress (MPa)
Distance (mm)
Stress-z
Stress-θ
Mises Stress

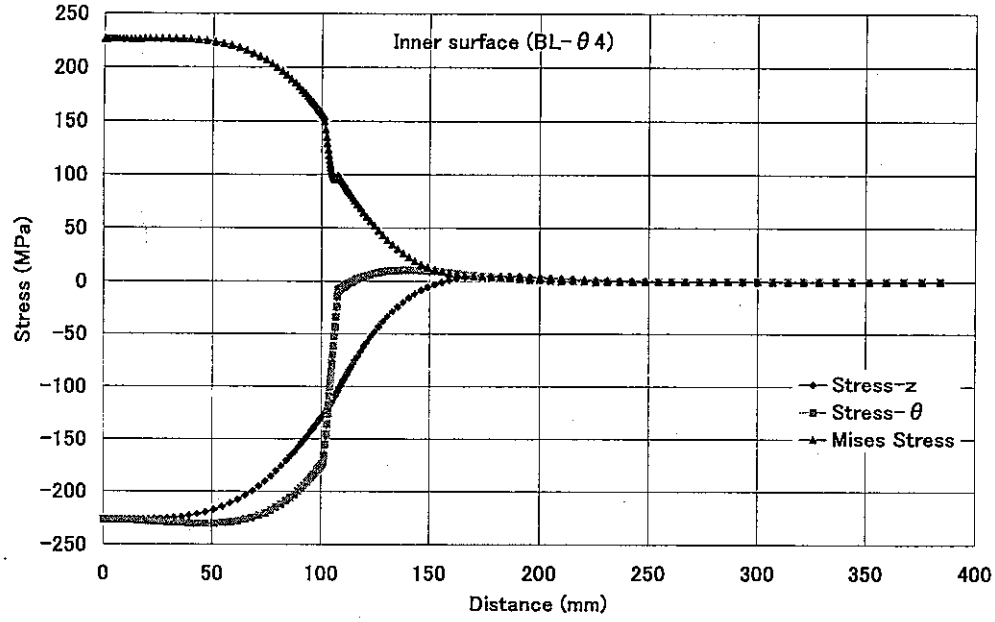

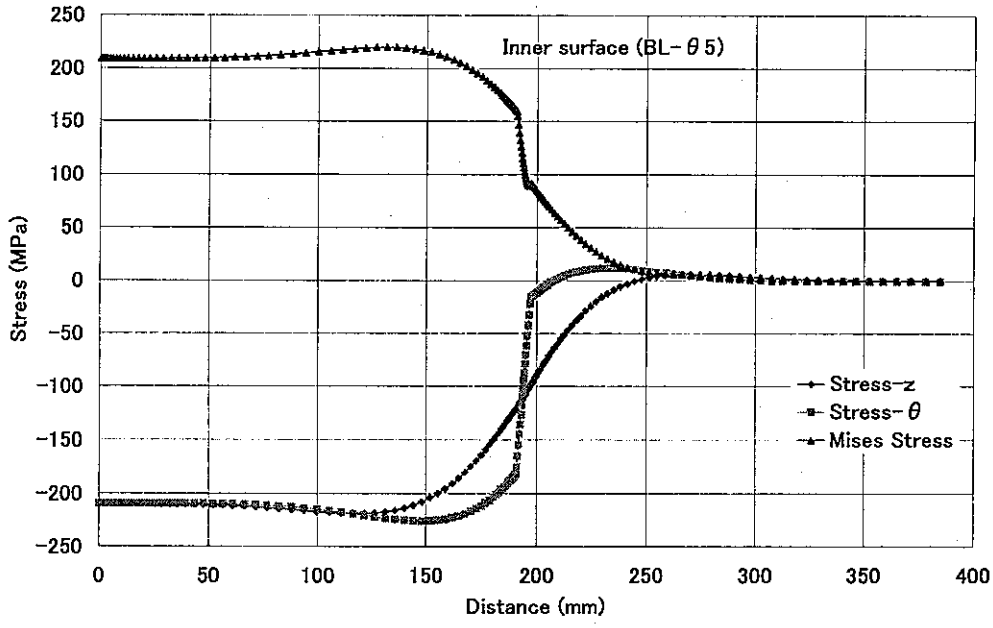

Fig. 5.12 Stress distribution on the inner surface (BL-θ series)

5.3. DIAGRAMS BY SHELL ANALYSES

From F.E. calculated results, we can get constraint efficiency factors for membrane and bending stresses.

Factors for membrane stresses are

$$A_m = \frac{|\sigma_C|}{\Delta\sigma^*} \quad \text{(Center of spot),} \tag{5.1}$$

$$A_m = \frac{|\sigma_i|}{\Delta\sigma^*} \quad \text{(Boundary of spot) and} \tag{5.2}$$

$$A_m = \frac{\max(|\sigma_c - \sigma_o|, |\sigma_i - \sigma_o|)}{\Delta\sigma^*} \quad \text{(Moving spot).} \tag{5.3}$$

Factors for bending stresses are

$$A_b = \frac{|\sigma_C|}{\Delta\sigma^*/2} \quad \text{(Center of spot),} \tag{5.4}$$

$$A_b = \frac{|\sigma_i|}{\Delta\sigma^*/2} \quad \text{(Boundary of spot) and} \tag{5.5}$$

$$A_b = \frac{\max(|\sigma_c - \sigma_o|, |\sigma_i - \sigma_o|)}{\Delta\sigma^*/2} \quad \text{(Moving spot).} \tag{5.6}$$

Next tables show evaluated constraint efficiency factors from shell analysis results and above equations.

Table 5.2 (a) Constraint efficiency factors by shell analysis (ML-t series)

Case	F.E.Calculated Mises Stress (MPa)			$\Delta\sigma^*$(MPa)=	Ratio A_m		
	Center of hot spot σc	Bounday inside hot spot σi	Bounday outside hot spot σo	$E\alpha/(1-\nu)\cdot\Delta T_f$	$\lvert\sigma_c\rvert/\Delta\sigma^*$	$\lvert\sigma_i\rvert/\Delta\sigma^*$	$\max(\lvert\sigma_c-\sigma_o\rvert,\lvert\sigma_i-\sigma_o\rvert)/\Delta\sigma^*$
ML-t1	-213.5	-196	103.00	420.86	0.507	0.466	0.75
ML-t2	-120.7	-181.6	107.30	420.86	0.287	0.431	0.69
ML-t3	7.39	-166.8	113.10	420.86	0.018	0.396	0.67
ML-t4	4.25	-151.3	118.20	420.86	0.010	0.359	0.64
ML-t5	0.00	-103.0	91.80	420.86	0.000	0.245	0.46

Table 5.2 (b) Constraint efficiency factors by shell analysis (ML-θ series)

Case	F.E.Calculated Mises Stress (MPa)			$\Delta\sigma^*$(MPa)=	Ratio A_m		
	Center of hot spot σc	Bounday inside hot spot σi	Bounday outside hot spot σo	$E\alpha/(1-\nu)\cdot\Delta T_f$	$\lvert\sigma_c\rvert/\Delta\sigma^*$	$\lvert\sigma_i\rvert/\Delta\sigma^*$	$\max(\lvert\sigma_c-\sigma_o\rvert,\lvert\sigma_i-\sigma_o\rvert)/\Delta\sigma^*$
ML-θ1	-190.1	-185.5	64.20	420.86	0.452	0.441	0.60
ML-θ2	-224.7	-205.6	69.30	420.86	0.534	0.489	0.70
ML-θ3	-194.0	-200.9	89.70	420.86	0.461	0.477	0.69
ML-θ4	7.39	-166.8	114.60	420.86	0.018	0.396	0.67
ML-θ5	0.58	-152.5	127.80	420.86	0.001	0.362	0.67

Table 5.2 (c) Constraint efficiency factors by shell analysis (BL-t series)

Case	F.E.Calculated Mises Stress (MPa)			$\Delta\sigma^*$(MPa)=	Ratio A_b		
	Center of hot spot σc	Bounday inside hot spot σi	Bounday outside hot spot σo	$E\alpha/(1-\nu)\cdot\Delta T_f$	$\lvert\sigma_c\rvert/(\Delta\sigma^*/2)$	$\lvert\sigma_i\rvert/(\Delta\sigma^*/2)$	$\max(\lvert\sigma_c-\sigma_o\rvert,\lvert\sigma_i-\sigma_o\rvert)/(\Delta\sigma^*/2)$
BL-t1	-193.8	-142.7	7.95	420.86	0.921	0.678	0.96
BL-t2	-231.4	-157.0	9.60	420.86	1.100	0.746	1.15
BL-t3	-226.5	-230.0	10.70	420.86	1.076	1.093	1.14
BL-t4	-208.8	-226.2	11.30	420.86	0.992	1.075	1.13
BL-t5	-210.4	-223.0	11.30	420.86	1.000	1.060	1.11

Table 5.2 (d) Constraint efficiency factors by shell analysis (BL-θ series)

Case	F.E.Calculated Mises Stress (MPa)			$\Delta\sigma^*$(MPa)=	Ratio A_b		
	Center of hot spot σc	Bounday inside hot spot σi	Bounday outside hot spot σo	$E\alpha/(1-\nu)\cdot\Delta T_f$	$\lvert\sigma_c\rvert/(\Delta\sigma^*/2)$	$\lvert\sigma_i\rvert/(\Delta\sigma^*/2)$	$\max(\lvert\sigma_c-\sigma_o\rvert,\lvert\sigma_i-\sigma_o\rvert)/(\Delta\sigma^*/2)$
BL-θ1	-94.7	-92.2	31.80	420.86	0.450	0.438	0.60
BL-θ2	-132.2	-117.1	24.70	420.86	0.628	0.556	0.75
BL-θ3	-201.9	-148.8	8.05	420.86	0.959	0.707	1.00
BL-θ4	-226.5	-230.0	10.50	420.86	1.076	1.093	1.14
BL-θ5	-209.2	-225.5	11.80	420.86	0.994	1.072	1.13

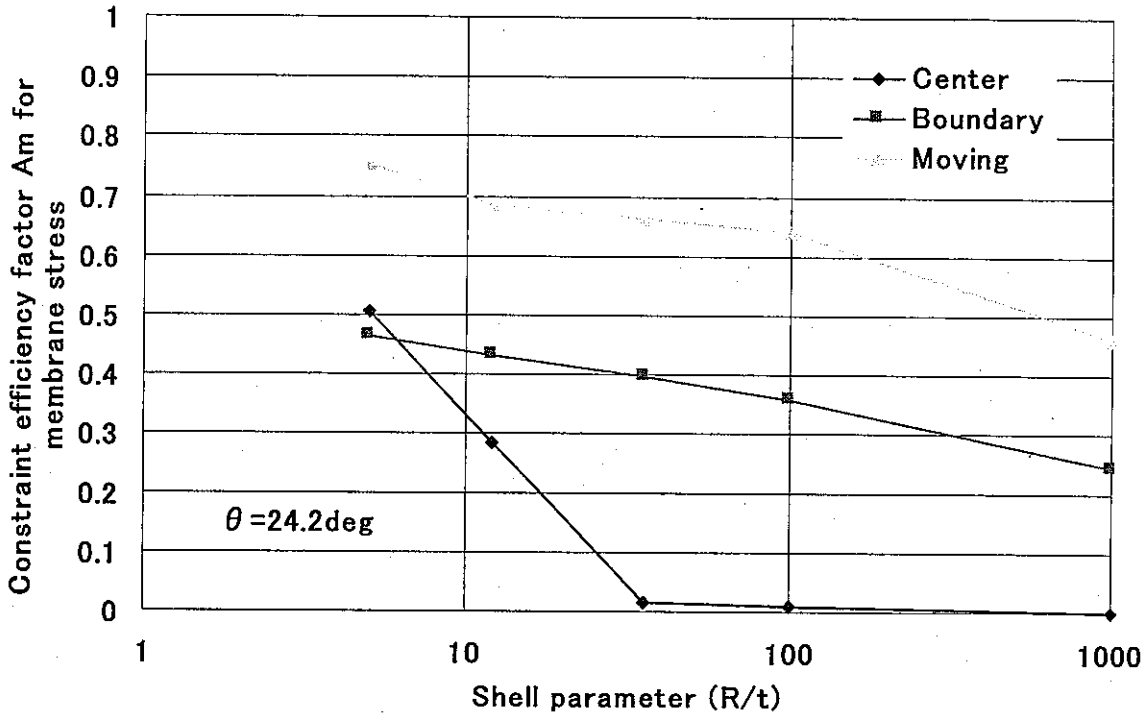

Fig. 5.13 (a) Constraint efficiency diagram for membrane stress (a)

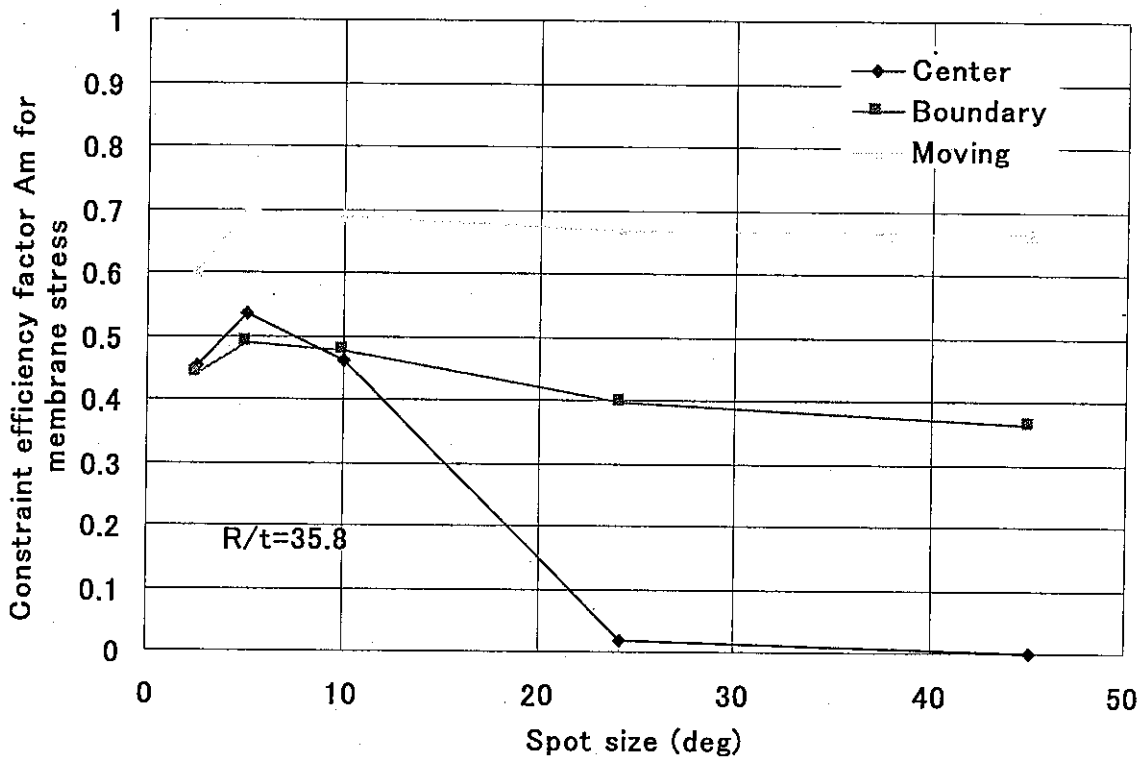

Fig. 5.13 (b) Constraint efficiency diagram for membrane stress (b)

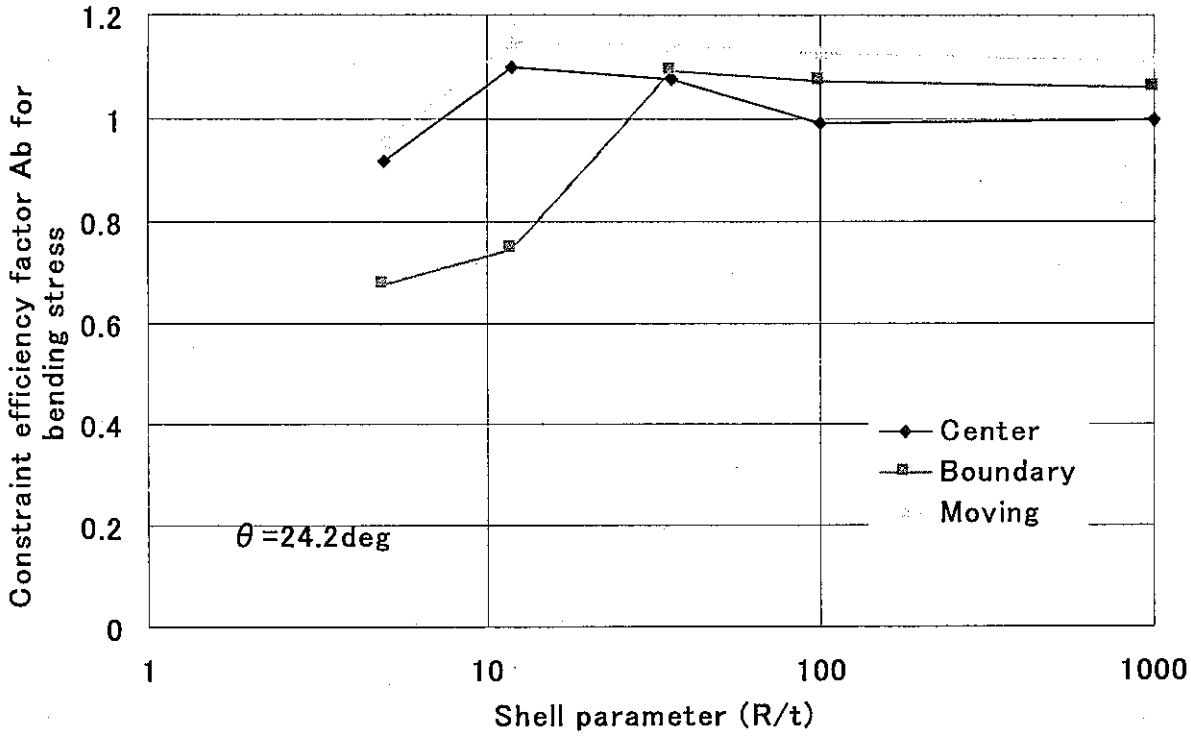

Fig. 5.14(a) Constraint efficiency diagram for bending stress (a)

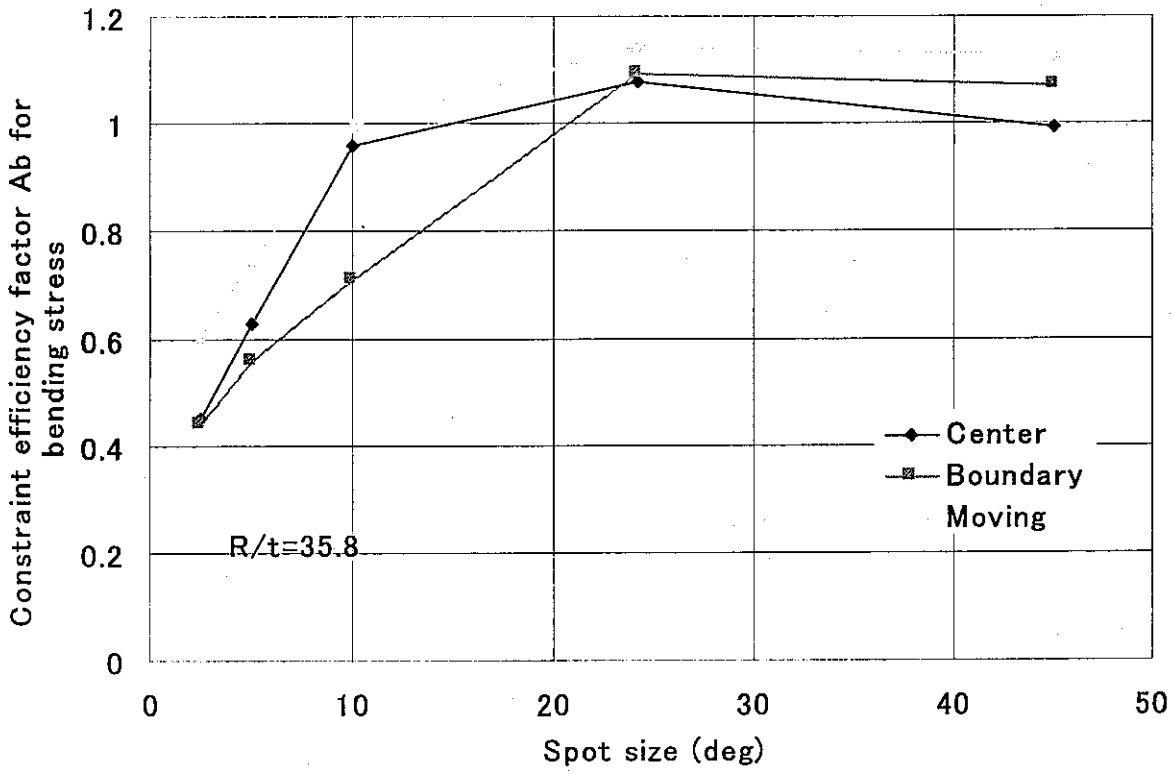

Fig. 5.14(b) Constraint efficiency diagram for bending stress (b)

6. CONCLUSIONS

Hot/Cold spot problems were formulated as the frequency response of structures under complex constrained. To quantify combined constraint conditions of membrane, bending and peak stress, author proposed constraint efficiency factors. By introducing these factors, the frequency response function was extended to Hot/Cold problems. Its applicability was validated by application to a hot spot near the T-junction of PHENIX secondary piping system.

Finally, diagrams of constraint efficiency factors were proposed to generalize this method.

The proposed method for Hot/Cold spot problems is summarized here.

Step 1

Identify geometrical parameters of pipes and hot/cold spot and determine constraint efficiency factors by chart described in Fig.5.4 and Fig.5.5.

Step 2

Evaluate the effective thermal stress function by the next equation.

$$S(jf^*, A_m, A_b) = -(B + jC) + (1 - A_m)(B_m + jC_m) + (1 - A_b)(B_b + jC_b), \tag{6.1}$$

where B, C, B_m, C_m, B_b, C_b are defines in Chapter 2 of this paper.

Step 3

Identify Biot number and evaluate the frequency response function with the effective heat transfer function as

$$G(B_i, jf^*, A_m, A_b) = H(B_i, jf^*)S(jf^*, A_m, A_b). \tag{6.2}$$

Constraint efficiency factor A_m can be defined for ratios of membrane stress and of bending stress stresses separately against membrane temperature. Constraint efficiency factor A_b is the same. These factors can be utilized more precious analysis.

ACKNOWLEDGEMENT

It is thankful in carrying out many finite element analyses to H.Takasho of Joyo industries. Several helpful discussions with Dr. Y. Lejeail of CEA-Cadarache, Dr. D. Moulin of CEA-Saclay, Dr. B.Drubay of CEA-Saclay, Dr.S.Chapuliot of CEA-Saclay, Dr. M.Sperandio, Dr. O. Gelineau and Dr. J.P.Simoneau of Framatome are gratefully acknowledged. The author is also deeply indebted to Dr. C.Poette and Dr. M.T. Cabrillat of CEA-Cadarache and Dr.M.Morishita of OEC/JNC for their kindness to make a chance of cooperative work under the EJCC contract.

REFERENCES

[1] Kasahara,N., Frequency response function method for evaluation of thermal striping phenomena , JNC TN9400 2001-005,(2000)

[2] Kasahara,N. and Lejeail, Y., Benchmark problems on thermal striping evaluation of FAENA and TIFFSS sodium experiments, JNC TN9400 2001-006,(2000)

[3] Kasahara,N. and Lejeail,Y., Interpretation of FAENA and TIFFSS experiments : Comparison of temperature evaluation methods on thermal striping , JNC TN9400 2001-014,(2000)

[4] Kasahara,N. and Lejeail,Y., Interpretation of FAENA and TIFFFSS experiments : Comparison of fatigue strength evaluation methods on thermal striping , JNC TN9400 2001-013,(2000)

[5] Gelineau,O., et al., Review of predictive methods applied to thermal striping problems and recommendations, SMiRT15, F06/3, (1999)

[6] PNC,"FINAS Version 12.0 User's Manual', PNC ZN9520 95-013, (1995)